TOWARDS A BETTER UNDERSTANDING OF EARTHQUAKE TRIGGERED LANDSLIDES:

AN ANALYSIS OF THE SIZE, DISTRIBUTION PATTERN AND CHARACTERISTICS OF COSEISMIC LANDSLIDES IN DIFFERENT TECTONIC AND GEOMORPHIC ENVIRONMENTS

Tolga Görüm

Examining committee:
Prof.dr. S.A.P.L. Cloetingh, *Universiteit Utrecht*
Prof.dr.ir. A. Veldkamp, *Universiteit Twente*
Prof.dr. V.G. Jetten, *Universiteit Twente*
Prof.dr. O. Korup, *Universität Potsdam*
Prof.dr. C. Gökçeoğlu, *Hacettepe Üniversitesi*

ITC dissertation number 235
ITC, P.O. Box 6, 7500 AA Enschede, The Netherlands

ISBN 978-90-6164-363-0
Cover designed by Tolga Görüm (Surface rupture of Denali Fault Earthquake along Slana River and triggered rock avalanches, LIDAR data from NFS Open Topography)
Printed by ITC Printing Department
Copyright © 2013 by Tolga Görüm

UNIVERSITY OF TWENTE.
FACULTY OF GEO-INFORMATION SCIENCE AND EARTH OBSERVATION

TOWARDS A BETTER UNDERSTANDING OF EARTHQUAKE TRIGGERED LANDSLIDES:

AN ANALYSIS OF THE SIZE, DISTRIBUTION PATTERN AND CHARACTERISTICS OF COSEISMIC LANDSLIDES IN DIFFERENT TECTONIC AND GEOMORPHIC ENVIRONMENTS

DISSERTATION

to obtain
the degree of doctor at the University of Twente,
on the authority of the rector magnificus,
prof.dr. H. Brinksma,
on account of the decision of the graduation committee,
to be publicly defended
on Thursday October 31, 2013 at 12.45 hrs

by

Tolga Görüm

born on January 01, 1980

in Muş, Turkey

This thesis is approved by
Prof.dr. Freek D. van der Meer, promotor
Dr. Cees J. van Westen, assistant promotor
Dr. Mark van der Meijde, assistant promotor

To Aral & Hale, Tuğçe & Eda for their unwavering love and support throughout this long journey…

And in memory of Prof. Dr. Erkan Gökaşan
The Quaternary Geologist & Geomorphologist who first inspired me and who passed away when this study was being completed.

Acknowledgements

Many people and organizations have contributed to completion of this work in many ways: spiritual, scientific, financial and technical. Those I would like to thank here. Let me begin by acknowledging the grant that facilitated my thesis research - the HUYGENS Scholarship Programme, Netherlands organization for international cooperation in higher education. I am heartily thankful to my promoter, Prof. Freek van der Meer for his scientific guidance and advice. It has been an honor and pleasure to know and to work with you. Invaluable thanks go to my first co-promoter, "daily" supervisor and great mentor Dr. Cees J. van Westen for his unlimited staying power in scientific guidance and advice, exemplary persuasive idealism, his interest also in details, and his friendship over the last 5 years. Cees, your contributions, detailed comments and mentorship have been of great value to me. I would not be where I am today without your help and support. I hope our collaboration continues for long. I would like to extend my hearty gratitude to my second co- promoter Dr. Mark van der Meijde for sharing his clear scientific vision, guidance, and encouragement. Without his valuable and expressive and especially timely comments it would have been difficult to complete this dissertation.

I express my sincere gratitude to Prof. İsmail Yüksek, Prof. Kutay Özaydın, Prof. Şükrü Ersoy and Prof. Mustafa Yıldırım from Yıldız Technical University for permitting me to pursue my PhD at University of Twente, The Netherlands.

I thank to Prof. Sierd Cloetingh, Prof. A. Veldkamp, Prof. Victor Jetten, Prof. Oliver Korup and Prof. Candan Gökçeoğlu for being the examiners of this thesis.

Special thanks are also necessary to a number of people who made field work in China possible, namely scientists and our research partners at the State Key Laboratory of Geo-hazard Prevention (SKLGP), Chengdu University of Technology (Prof. Runqiu Huang, Prof. Qiang Xu, Prof. Chuan Tang, Prof. Jing Zhu, Prof. Li Yong, Dr. Li Weile, Dr. Liu Hanfu, and Mr. Chen Wei). I would like to give my special thanks to Prof. Niek Rengers for his efforts on the collaboration between ITC and the SKLGP. I also want to thank Prof. Candan Gökçeoğlu, Prof. Timur Ustaömer, Prof. Fatma Gül Kılıç, Prof. Gonghui Wang, Prof. Dai Fuchu, Dr. Chong Xu, Dr. Hakan A. Nefeslioğlu, Dr. Cengiz Yıldırım and Dr. Uğur Şanlı for inspiring discussions, sharing data and kind

encouragements. A person that needs special mention herein is Dr. Füsun Balık Şanlı – as a friend and as a colleague her contributions to this thesis was invaluable.

This acknowledgement cannot be complete without expressing my very special thanks to Prof. Oliver Korup. Thank you (and Ariane) for your support and hospitality during my stay at Potsdam and for your consistent generosity in help, and for sharing with me your wide and deep knowledge of Geomorphology, while always keeping a high spirit.

Many thanks also to all staff members at ITC for their helps and supportive service. People from ITC whom I cannot forget are: Paul van Dijk, Loes Colenbrander, Marga Koelen (it was an honor to work with you in the library committee), Carla Gerritsen, Bettine Geerdink, Ivo Bijker, Lyande Elderink, Marie Chantal Metz, Theresa van den Boogaard, Christie Agema, Marion Pierik, Benno Masselink and Job Duim. Without their support this thesis would not have come to an end.

I would like to broadly thank all the colleagues and students in the ESA whose friendship, enthusiasm, encouragement and example inspired and motivated my time in the department. I would like to acknowledge the older and the new graduate students, in particular the "landslide mafia" (Xuanmei, Byron, Jean Pascal, Simone, André, Khamarrul, Saibal, Sekhar, Darwin, Haydar, Tapas and Pankaj) who provided me with wonderful mentorship and amazing encouragement in life and landslide research field. Especially to Xuanmei, we worked in the same study area, sometimes in the same desk and had shared many memorable Chinese experiences. Fan Xuanmei, your kind support was always there whenever I needed, thank you for that and most of all, thank you for your friendship.

At ITC and Enschede I was lucky to be surrounded by many friends and colleagues. First of all, I would like thank 5th floor gang Sanaz, Sharon, Shruthi, Shafique, Sumbal, Fangyuan, Frederick, Pablo, Nugroho, Juan, Effie, İslam, Anandita, Yaseen, Zack, Fekerte, Chenxiao, Matthew and Nasrullah. I also thank to Zoltan, Wim, Tina, Syarif, Fouad, Alain, Xuelong, Joris, Murat, Jahanzeb from WRS department. Special thanks to Mustafa, Ioannis, Diana, Byron, Chandra, Mireia, Yijian, Enrico, Leonardo for sharing ups and downs of

our PhDs, jokes, dinners, drinks after work in De Beiaard, foosball tournaments and friendship.

I am grateful to my close Turkish friends, Mustafa, Oktay, Banu, Özgün, Sedef, Bengü, Mehmet, Damla, Gül, Ali abi, Devrim and Metehan. Thank you all for sharing the good food and company. Without you all my life in the Netherlands would not have been comfortable and happy. Especially you Mustafa, at the end of this five-year period; as well as giving the diploma which clinched the academic life, those low lands have also given to me a friend like you. Dreaming of the Netherlands, you are in the most important memories that are left in my mind and you will always be. Many thanks for your friendship, company, and brotherhood.

Most importantly, I am and will forever be deeply indebted to my family (Aral, Hale, Eda, Tuğçe, Ayla and Halim) for their love and support that enable me to achieve this goal. Especially, I would like to thank my loving life partner and best friend, Hale. None of this would have been possible without the unconditional love, support and guidance you have given me over the last 5 years. And you Aral, you are the most beautiful miracle in our life and the greatest joy we can ever know. Aral, bil ki bizim için bu dünyada yer ile gök arasındaki en büyük düğümsün. İyi ki varsın!

Life is just a circle
Loop-de-loop round and round
One day you are the king of the hill
The next day you are tumbling down

Omar & The Howlers "Life Is Just A Circle" – Lyrics

Contents

List of figures

List of tables

1 Introduction

1.1 Background

Earthquakes have long been recognized as one of the main triggers for landslides across the globe as well as one of the driving engines behind the creation of mountainous topography. Intermediate and large earthquakes in mountainous terrain can produce clusters of several hundreds to thousands landslides in a very short period of time (Wilson and Keefer, 1979; Keefer, 1984; Harp and Jibson, 1996; Liao and Lee, 2000). Landslides triggered by earthquakes are significant natural hazards to human life and property in many areas of the world, however usually their destructive impact and casualties are included in the overall losses reported for the earthquakes, and thus their long-term economic and societal impacts are commonly overlooked or underestimated. For instance the 2008 Wenchuan, China (M_w 7.9) earthquake triggered around 60,000 landslides which were estimated to be responsible for a quarter to one third of the 88,000 casualties (Wang et al., 2009), indicating that the coseismic landslides as a secondary phenomena can be at least as important as the acute hazard of major earthquakes.

Predicting where earthquake triggered landslides are likely to occur in relation to future earthquakes is difficult because scientifically reproducible predictions of where and when earthquakes will occur cannot be made yet. Nevertheless, these landslides are a consequence of the earthquake dynamics although their rate and distribution highly depend on the seismic characteristics of the event and the local geo-environmental conditions (topography, soil and rock types) of the area. Earthquake-induced landslides have been documented from at least as early as 1789 BC in China (Hansen and Franks, 1991) and 372 BC in Greece (Seed, 1968). The first scientific study of earthquake-induced landslides and their systematic documentation was undertaken in the Calabria region of Italy after the 1783 earthquake swarm and the first basic inventory for earthquake-induced landslides was produced in 1957 for Daly City (USA) after the California earthquake (Keefer, 1994). The first large and substantially complete inventory was done by Harp and Jibson in 1996 for the 1994 Northridge, California (M_w 6.7) earthquake. However, the knowledge of these phenomena have become more detailed and comprehensive with time as increased resources and new tools, such as aerial photography, Geographic Information Systems (GIS) and Remote Sensing (RS) technologies, have been available (Soeters and van Westen, 1996; Keefer, 2002). The widespread use of these tools enabled to

determine the landslide distribution over large areas, and thus improve the understanding of the relation between earthquake dynamics and coseismic landsliding.

The density of coseismic landslides and their distribution pattern can be highly variable in both its spatial and temporal aspects because of the variability of factors related to topography, geology, and morphogenesis, the epicentral location and the frequency-magnitude of the seismic events. The effect and imprint of these coseismic landslides in a geomorphic environment may persevere over time, thus can direct the erosional activities spatially and can add substantially to erosion after an earthquake. Moreover, quantitative assessments of different coseismic landslide event-inventories in different geomorphic and tectonic environments not only help to reveal details of the large historical or contemporary earthquake mechanisms in seismically poor instrumented region but also help to improve the theoretical framework for the predictive mapping of susceptibility to occurrence of earthquake triggered or induced landslides.

1.2 Problem statement

The occurrence and distribution characteristics of earthquake-induced landslides have been studied since 1970's systematically through event based inventories at regional and global scale (e.g., Plafker et al., 1971; Youd and Hoose, 1978; Harp et al., 1981; Keefer, 1984; Harp and Jibson, 1996; Parise and Jibson, 2000; Bommer and Rodriguéz, 2002; Khazai and Sitar, 2003; Malamud et al., 2004). In the last three decades, previous studies have contributed to the understanding of landsliding associated with earthquakes by studying spatial distributions of coseismic landslides in relation to earthquake magnitude, ground motion parameters, distance from epicenter or from ruptured master faults, geological properties (lithology, soil, etc.), geomorphic features (rivers, ridges, etc.) and topographic variables (slope gradient, altitude, etc.). Most significant studies in this context, for instance, Keefer (1984 and 1999) and Rodríguez et al. (1999) and also the later following studies (e.g. Malamud et al. 2004) have been pioneering the systematic compilation and analysis of inventories of earthquake-induced landslides, and proposed empirical curves on the basis of relationships between the total number and maximum or total area to be affected by landslides in relation to earthquake magnitude or distance from hypocenter (e.g. Meunier et al., 2007). Generally, documented spatial patterns of earthquake triggered landslides do reveal some systematic distribution with respect to these controls, yet local differences may be

considerable. Overall, in the point of seismic controls, a big majority of these studies has focused size distribution and spatial pattern of landslides with respect to the magnitude of the event, the location and distance from earthquake epicenter or coseismic fault. Accordingly, it was generally concluded that the number and total volume of landslides triggered by an earthquake, and the area affected by landsliding scale with earthquake magnitude (Keefer 1999; Malamud et al., 2004), and landsliding decreased significantly with increasing distance from the hypocenter (Meunier et al., 2007) or epicenter (Keefer 1984; Rodríguez et al., 1999) and the coseismic fault (Keefer 2000; Khazai and Sitar 2003).

However, recent strong earthquakes have triggered significantly lower numbers and area affected by landslides than those expected from global empirical approaches. For example, the 2002 Denali (M_w 7.9) earthquake that struck the glaciated mountainous terrain of Alaska Range, had triggered considerably fewer landslides (<1,600) than expected. Moreover, the 2010 Haiti (M_w 7.0) and Yushu (M_w 6.8) earthquakes can be considered as precedent events with their lower total area of coseismic landslides compared to the area of those triggered by similar magnitude events. These events highlight the limited applicability of such empirical relationships with their unexplained variance of up to an order of magnitude. This can be attributed to variations in geomorphic or geologic characteristics of different regions that are not taken into account in the analysis of global empirical approaches. However, this observed global variability may also be rooted in variability of the slip mode and earthquake rupture dynamics along the ruptured faults, yet regarding to potential controls of these factors on coseismic landsliding response have not been fully investigated.

Furthermore, differences in faulting style and fault geometry have been found to influence rupture dynamics with modulating the radiation pattern of the seismic waves (Sommerville et al., 1997; Anderson 2000; Oglesby et al., 1998 and 2000a). From a seismological perspective, the localization of the seismic energy along the rupture fault plane differs significantly between dip-slip and strike-slip faulting earthquakes. In general, fault plane slopes of the dip-slip faults are lower (<60°) than the slopes of strike-slip faults (>60°). Therefore, while the most of the energy released from the dip-slip faulting earthquakes localized and focus on the hanging wall of the fault, there is significantly less ground motion in the foot wall section of the fault. In contrast, in strike-slip faulting earthquakes, the pattern of the strong ground motion is more symmetric in the both side of the coseismic fault, though possible variations in seismic radiation

field may occur along the fault due to propagation direction of the rupture (Ben-Zion and Sammis, 2003; Dor et al., 2006). Moreover, dynamic rupture simulation models demonstrate that, for the same initial stress magnitude, thrust or reverse faults produce higher ground motion than normal faults (Oglesby et al., 2000a and 2000b; Ma, 2009), which in turn generally exceeds the fault and ground motion in strike-slip faults. Despite longstanding research on the landsliding associated with earthquakes, how these varying slip and rupture dynamics due to fault type and geometry control the spatial distribution of coseismic landslides remains unknown. Yet together with the topographic variations very little is known about their joint controls on coseismic landsliding. Thus, to go beyond these obscurities, we need more comparative studies from substantially complete event- inventories in different tectonic and geomorphic environments in order to generically embody the distribution pattern and the abundance of coseismic landslides with respect to controlling factors.

1.3 Research objectives

The general objective of the study presented in this thesis is to improve current state of coseismic landslide knowledge in a global context with exploring the role of earthquake rupture dynamics, faulting styles, topography and rock-type on the size, abundance and the distribution pattern of the coseismic landslides in different seismo-tectonic and geomorphic environments. To achieve this goal, the following specific objectives were defined:

- to evaluate the effect of faulting styles and fault geometry on the coseismic landslide distribution characteristics
- to assess whether coseismic landsliding responses and their spatial pattern differ between blind and surface-rupturing earthquakes.
- to determine and to further characterize the potential control of coseismic slip rate and mode together with the differences in rock-type and geomorphic characteristics, on clustering of landslides along the seismogenic faults.
- to develop a conceptual model on the basis of the results presented in this study, thus bring new perspectives in field of earthquake-induced landslide studies.

1.4 Study sites

In this thesis, a total of seven polygon based event-inventory of landslides triggered by the strike-slip and dip-slip earthquakes were used (Figure 1.1). The coseismic event-inventories of 2002 Denali Fault, Alaska (M_w 7.9), 2007 Aisén Fjord, Chile (M_w 6.2), 2008 Wenchuan, China (M_w 7.9) and 2010 Haiti (M_w 7.0) earthquakes were generated within the scope of this thesis. The locations and areas of total 66,700 individual landslides in this four core study sites were mapped from visual comparison of pre- and post-earthquake high-resolution satellite images and aerial photos. The study conducted a large-scale regional analysis at high spatial resolution of coseismic landslides in seismologically and geomorphologically contrasting events and landscapes. In this respect, the seismological (i.e. similar magnitudes and/or dissimilar faulting mechanisms) and geomorphological (i.e. local relief and/or geomorphic environment) differences were principally guided the criteria that were used in selecting these study sites.

1.4.1 Thrust or reverse-faulting earthquakes

1994 Northridge, USA (M_w 6.7) earthquake: The M_w 6.7 Northridge earthquake occurred January 17, 1994 on a blind thrust fault in the subsurface beneath the San Fernando Valley, southern California. The earthquake characterized by its unusual large ground motions and the coseismic slip model results place the upper boundary of the meter-level coseismic rupture at a depth of about 5 km (Shen et al., 1996). The event triggered nearly 11,000 landslides which were heavily clustered on the steeper hillslope (20°- 40°) compared to the average (~12°) of the study area (Harp and Jibson, 1996). The Northridge earthquake occurred in semi-arid area at a dry season, and most of the reported coseismic landslides occurred on the weakly cemented clastic sediments where the coseismic landslides are considerably close to upper slopes and ridges crests (Harp and Jibson, 1996).

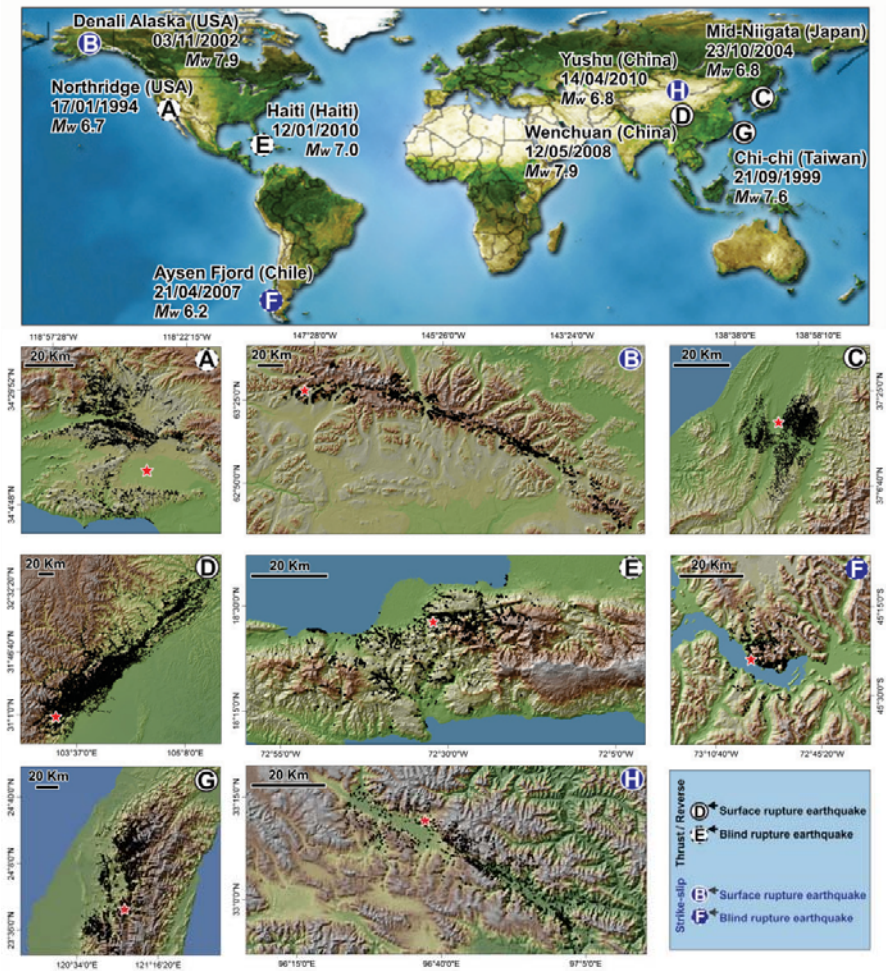

Figure 1.1 Location map of the study sites. Red stars denote the epicentral locations of the each event.

1999 Chi-chi, Taiwan (M_w 7.6) earthquake: The September 21, 1999 Chi-chi earthquake (M_w 7.6) ruptured nearly 100 km of a major thrust fault along the western foothills of the Central Range of Taiwan. The hypocenter located at a depth of 8 km beneath the Chi-Chi area (Tsai and Huang, 2000). Coseismic movement adjacent to the rupture displays northwest slip with horizontal displacements of 7-9 m and vertical displacement of 3-10 m based on geological field measurements (Chen et al., 2001). The earthquake is characterized by low Peak Ground Acceleration and high Peak Ground Velocities (Tsai and Huang, 2000). The earthquake occurred in a relatively dry

season of subtropical climate. More than 22,000 landslides were mapped by the National Science and Technology Center for Disaster Prevention of Taiwan using 20 m resolution SPOT satellite images taken shortly after the earthquake. The majority of the landslides occurred within a distance of 20 km from the surface rupture while the greatest distance from the rupture is about 70 km (Liao and Lee, 2000). In this event, most of the reported landslides clustered on the Tertiary sedimentary rocks.

2004 Mid-Niigata, Japan (M_w 6.8) earthquake: The Mid-Niigata earthquake occurred on 23 October 2004 in the Shinano River fold and thrust zone, western margin of Northeast Japan (Japan Meteorological Agency, 2004). The event produced a nearly 1-km long, N-S to NNW-SSE striking, west-side-up surface rupture along a previously unmapped fault at Obiro, Uonuma City, eastern margin of the epicentral region (Maruyama et al., 2005). Seismological studies indicated that the rupture initiated at a depth of ca. 13-km and extended along over 20-km long NNE-SSW-trending NW dipping reverse fault (Hirata et al., 2005). The maximum coseismic slip is between 1.0-1.6 meters and occurred over approximately 6s in an elongate, 15-km long patch near the 2-km base of surface expression of the seismogenic fault (Yoong and Okada, 2005). The event occurred in a relatively wet season of humid subtropical climate. The Mid-Niigata earthquake triggered more than 4,400 landslides over an area of 1,000 km^2. These were mainly shallow slides, although more than 150 deep-seated (deep >10-m) translational rock and debris slides also occurred (Sekiguchi and Sato, 2006; Yamagishi and Iwahashi, 2007). Most of these landslides clustered on the moderately steep slopes (i.e. > 28°), and mainly composed of Neogene sedimentary rocks.

2008 Wenchuan, China (M_w 7.9) earthquake: The Wenchuan earthquake (M_w 7.9) occurred on 12 May 2008 (USGS, 2008) in the Longmen Shan region at the eastern margin of the Tibetan Plateau, adjacent to the Sichuan Basin. The earthquake, with a focal depth of ~14 km to 19 km, initiated close to the base of the Beichuan fault and propagated upwards. Seismological data indicate that the rupture initiated in the southern Longmen Shan and propagated unilaterally toward the northeast, along a northwest dipping fault for about 320 km (Xu et al., 2009). The earthquake ruptured both the Beichuan (about 240 km long) and Pengguan faults (72 km long), which are linked by a short northwest striking rupture zone at the southern end surface rupture through a lateral ramp. The largest surface slip (about 11.0 m vertical and 4.5 m right-lateral displacement)

is found near Beichuan town (Liu-Zeng et al., 2009). This event produced more than 60,000 landslides throughout an area of about 20,000 km^2, from which a total area of 850 km^2 was affected by landslides (Dai et al., 2010; Gorum et al., 2011). This number and the area affected by the landslides made this event one of the most significant ever recorded in historic times. Furthermore, the landslide distribution shows a very distinct "hanging wall" effect, and most of landslides occurred within a 20 km range from the seismogenic fault (Gorum et al., 2011). Most of these landslides clustered on the steep slopes which are higher than 35°and mainly composed of Cambrian sandstone and siltstone intercalated with slate or Precambrian metamorphic rocks.

2010 Haiti (M_w 7.0) earthquake: The 12 January 2010 M_w 7.0 Haiti earthquake occurred in a complex deformation zone at the boundary between the North American and Caribbean plates. Combined geodetic, geological and seismological data posited that surface deformation was driven by rupture on the Léogâne blind thrust fault, while part of the rupture occurred as deep lateral slip on the Enriquillo-Plantain Garden Fault (EPGF) (Hayes et al., 2010). The earthquake triggered more than 4,490 landslides in a tropical climate environment, and these landslides are mainly shallow, disrupted rock falls, debris-soil falls and slides, and a few lateral spreads, over an area of ~2150 km^2. Most of the coseismic landslides did not proliferate in the hanging wall of the main rupture, but clustered instead in a 5-km wide corridor at the junction of the blind Léogâne and EPGF ruptures, where topographic relief and hillslope steepness are above average of the area (Gorum et al., 2013). Coseismic slope failures occurred mainly in the Eocene and the Upper Miocene limestones.

1.4.2 Strike-slip faulting earthquakes

2002 Denali Fault (M_w 7.9) earthquake: The M_w 7.9 Denali Fault earthquake struck the central Alaska Range on 3 November 2002. The event was one of the largest earthquake in U.S. history, ruptured unilaterally from west to east about 340 km in 100 seconds on along three major faults in the interior of Alaska. The geological and seismological observations show that the Denali Fault earthquake originated with thrust motion on the Susitna Glacier Fault, with an average dip slip of 4 m and then ruptured along 226 km of the Denali Fault where right lateral slip at the surface averaged 4.5-5.1 m and reached a maximum of 8.8 m (Haeussler et al., 2004) about 40 km west of the Denali-Totschunda fault junction. Finally, the rupture propagated southeasterly another 66 km along the Totschunda fault, where right-lateral surface displacements

averaged 1.7 m (Eberhart-Phillips et al., 2003; Haeussler et al., 2004). The 2002 Denali Fault earthquake triggered at least 1,580 landslides over an area of 7,150 km^2, and up to a distance of ~380 km from the epicenter. The majority of coseismic landslides clustered in a ~10-km wide corridor along the surface ruptures (see Chapter 3). The Tertiary granitic rocks and ice covered terrains are the most landslide-prone units in terms of landslides.

2007 Aisén Fjord (M_w 6.2) earthquake: The M_w 6.2 Aisén Fjord earthquake occurred in the nearby town of Aisén, Chilean Patagonia on April 21, 2007(Global CMT Catalog, 2008; NEIC, 2008). The main shock focal mechanism was strike-slip with a north-south plane solution (CMT Global Catalog, 2008), and indicates one of the main mapped branches of the Liquiñe-Ofqui Fault Zone which is a right-lateral strike-slip fault zone that accommodates the parallel component of the oblique subduction of the Nazca plate beneath the South American plate (Sepúlveda and Serey, 2009). The earthquake did not create surface rupture, however the development of aftershock activity to the east of the main fault indicates that the sequence of 2007 and its main event, the April 21 Aisén earthquake, re-activated subsidiary faults located to the East of the main fault that belong to the same structural system (Agurto et al., 2012). The event-inventory of landslides associated with the earthquake was generated from 10-m resolution SPOT satellite image within the scope of this thesis. The event triggered 515 landslides which were mainly rock slides and avalanches, rock falls, and debris flows. Despite the relatively low magnitude of the earthquake the average size of the landslides were found considerably high (see Chapter 3). The majority of coseismic landslides occurred in the high periglacial mountainous terrain and clustered near the ridge crests. In this event, most of the mapped landslides were occurred on the Cretaceous intrusive rocks.

2010 Yushu (M_w 6.8) earthquake: The M_w 6.8 Yushu earthquake struck the northeastern section of the semi-arid Tibetan Plateau around the Yushu County, Qinghai Province, China on 14 April 2010 (Li et al., 2011). This event occurred on the left-lateral Yushu fault that forms the western part of the Yushu-Garzê-Xianshuihe fault zone which is one of the most active fault zones in eastern Tibet (Lin et al., 2011). Integrated results of the SAR and optical imagery, and body wave seismology show that nearly pure left-lateral slip has occurred on three segments of the Yushu fault over a distance of nearly 80 km, with maximum slip of 1.5 m on the 30 km long southeastern segment (Li et al., 2011). Nearly 2,000 landslides were mapped by Xu et al. (2012) throughout an

area of about 3,000 km^2 from very high resolution aerial photos and satellite images. The reported sizes of the coseismic landslides were considerably small, although landslides cover about a total area of 1.2 km^2. The coseismic landslide density is strongly controlled by proximity to the main surface ruptures, and most landslides clustered in a 3 km of wide corridor along the seismogenic fault. Most of these landslides clustered on the steep slopes (i.e. > 32°), and mainly composed of Mesozoic sandstone, siltstone and limestone or Neogene sedimentary rocks.

1.5 Structure of the thesis

This thesis consists of a total of six chapters. Apart from the introduction and synthesis, the four remaining core-chapters have either been published in peer-reviewed journals or are under review.

Chapter 2 shortly introduces the state of art in the field of regional scale earthquake triggered landslide studies. The chapter defines the event-inventory and landslide mapping criteria which are also followed and applied to other study sites within the scope of this thesis. This chapter further compare the landslide distribution results of 2008 Wenchuan (M_w 7.9) earthquake from two different inventories, and presents the results of an extensive study of the mapping the distribution of 60,000 landslides triggered by the Wenchuan earthquake in Sichuan Province, China, on 12 May 2008.

Chapter 3 investigates the role of the fault geometry, coseismic slip rate and mode together with the local topographic and geomorphic differences on the size- and spatial-distribution pattern of landslides triggered by the 2002 Denali Fault (M_w 7.9) strike-slip faulting earthquake. The resulting patterns are then used to compare other documented event-inventories from similar faulting earthquakes for determining the common or divergent distribution signatures of the coseismic landslide patterns in different geomorphic environments.

Chapter 4 analyses the combined effect of complex rupture dynamics, rock-type and topography on previously rarely documented pattern of nearly 4,500 landslides associated with the 2010 Haiti (M_w 7.0) earthquake. This chapter further investigates whether coseismic landsliding responses and their spatial pattern differ between blind and surface-rupturing earthquakes. For that purpose the event-inventories of six reverse or thrust-fault earthquakes with regard to potential controls of magnitude, occurrence of surface ruptures, and local relief,

on coseismic landsliding response were compared to build a better picture of regional distribution characteristics of landslides.

Chapter 5 examines whether and how distinct faulting styles modulate both the abundance and spatial patterns of earthquake-induced landslides in a global and regional sense (from a global and regional viewpoint). In the context of this chapter, a data set on fault-dip angles and rupture mechanisms together with the total number of coseismic landslides from fifteen substantially complete inventories were compiled to characterize the global signature of coseismic landsliding response. Furthermore, the event-inventory of >60,000 landslides triggered by the 2008 Wenchuan (M_w 7.9) earthquake along the Yingxiu-Beichuan fault, where two distinct types of faulting mechanisms occurred over a rupture length of 240 km was used in this chapter for regional-scale assessments.

Chapter 6 provides a conceptual model based on the synthesis of the obtained results, and discusses the outcomes and their implications for the earthquake-induced landslide studies, and finally concludes with recommendatory remarks on the direction and scope for further research.

2 Identification, mapping and regional distribution pattern of landslides triggered by the 12 May 2008 Wenchuan earthquake[1]

2.1 Introduction

The study of earthquake-induced landslide distribution has a major importance for a better understanding of the relationship between landslide density, type, and size and the causal mechanisms. These causal mechanisms are a complicated interplay between seismic parameters (e.g. the earthquake magnitude, depth, focal mechanism, fault plane geometry, coseismic slip) and terrain parameters, related to morphology (slope angle, orientation, altitude, slope curvature), slope materials (soil cover, lithology and geological structure), hydrology, land use, and geomorphology (e.g. the presence of old landslides). The knowledge of causal mechanisms for earthquake-induced landslides is essential for the improvement of spatial earthquake-induced landslide prediction methods.

From previous major earthquakes that occurred in mountainous areas, much has been learned about the causal mechanisms (Keefer, 1984, 2000; Jibson and Keefer, 1989; Keefer and Manson, 1998; Khazai and Sitar, 2003; Jibson et al., 2004; Harp and Crone, 2006; Chigira and Yagi, 2006; Mahdavifar et al., 2006; Sato et al., 2007; Wang, H.B. et al., 2007; Owen et al., 2008). For instance the Chi-Chi earthquake of 1999 generated a large amount of research on the relation between causal factors and earthquake-induced landslides (Wang, W.N. et al., 2003; Khazai and Sitar, 2003; Lee et al., 2008).

In many studies, the focus was on the relation between landslides and the triggering seismic factors, such as the magnitude and mechanisms of the event. This was done by analyzing the relation with the distance to the epicenter and coseismic fault rupture, the magnitude, intensity and peak ground acceleration (PGA) of the earthquake with the landslide distribution pattern. Among these, Keefer (1984) and Rodriguez et al. (1999) made global study of the landslides that occurred after 40 and 36 earthquakes respectively, and presented the relations between the distribution, type and area coverage of the landslides with

[1] This chapter is based on the following paper: Gorum, T., Fan, X., van Westen, C.J., Huang, R., Xu, Q., Tang, C., Wang, G., 2011. Distribution pattern of earthquake-induced landslides triggered by the 12 May 2008 Wenchuan Earthquake. *Geomorphology 133, 152–167.*

parameters such as the distance to the epicenter, the magnitude of the earthquake and the distance to fault rupture. As a result of these studies, it was found that there is positive relation between the magnitude of the earthquake and the distance of the landslides to the coseismic fault. Although these studies were general in terms of their scale, they are important in revealing general trends. Another study on the relation of landslide distance to the epicenter carried out in Greece by Papadopoulos and Plessa (2000) also supported the negative relation between the distance to the epicenter and landslide, and revealed that earthquakes that trigger landslides range in magnitude from M_s=5.3 to 7.9, with peaks at M_s=6.4 and 6.7.

In contrast with these general conclusions, it was found in the Wenchuan area that deep-seated landslides also occurred far away from the epicenter. For instance, the Donghekou landslide occurred 225 km from the epicenter, although only a 700 m from the coseismic fault (Huang and Li, 2009). Also the 1999 Duzce (Turkey) earthquake (M_w 7.2) is not in line with the general trend. The Duzce earthquake was caused by a right lateral strike-slip rupture along part of the secondary Duzce fault and the length of surface rupture was estimated to be 45 km, with an average lateral offset of 4m. The earthquake only triggered 45 landslides, with a total area of 4 km^2 despite its relatively high magnitude. Parallel to these findings, several studies in the last 10 years report that the distribution of earthquake triggered landslides is more related to the distance from the surface projection of the fault plane and the surface projection up-dip edge of the fault rather than the distance from the epicenter (Keefer, 2000; Mahdavifar et al., 2006; Sato et al., 2007; Huang and Li, 2009).

On the other hand, it is known from recent studies that the dynamics of the earthquake rupture process are complex. Due to the different geometry the coseismic slip resulting from a fault rupture is distributed differently along the fault which cause differences in the deformations along the fault (Barka et al., 2002; Hsu et al., 2002; Cakir et al., 2003; Avouac et al., 2006; Fukuyama, 2009; Lin, 2009; Hao et al., 2009). There are also studies which put forward that the different distribution patterns of deformation as a result of coseismic faulting is more highlighted in strike-slip systems, especially depending on the direction of surface rupture propagation (Ben-Zion and Huang, 2002; Ben-Zion and Sammis, 2003; Dor et al., 2006). All these studies show that the earthquake rupture process is rather complex and that the distribution of the landslides triggered by the fault rupture also presents a complicated phenomenon.

Several studies that consider the parameters belonging to the triggering mechanisms such as Arias and MMI intensities and peak ground acceleration (PGA) found a higher correlation with the landslide distribution pattern (Meunier et al., 2007, 2008; Lee et al., 2008; Miles and Keefer, 2009). For instance, Meunier et al. (2007) studied the patterns of landslides induced by earthquakes in California, Taiwan and Papua New Guinea, and reported a close relation with ground shaking. In all three cases, they mentioned that the density of coseismic landslides peaked with the largest ground accelerations. For the Chi-Chi and the Northridge earthquakes, strong correlations were reported between landslide density and both the vertical and horizontal components of recorded peak ground accelerations.

Geo-environmental factors such as lithology, morphology, presence of secondary active or inactive faults also have a strong relation with earthquake-induced landslide distribution (Crozier et al., 1995; Keefer, 2000; Jibson, et al., 2000; Chigira et al., 2003; Wang, W.N. et al., 2003; Khazai and Sitar, 2003; Chigira and Yagi, 2006; Yagi et al., 2009). In these studies, it was found that the density of earthquake-induced landslides was higher in weakly cemented, unconsolidated and semi-consolidated lithological units, and in highly fractured and weakened rocks. Also the presence of old landslides formed prior to the earthquake can be considered important, as these may be re-activated. Different morphological factors, such as relative relief, slope steepness or terrain roughness can also result in distinct landslide distributions and types.

Therefore, a detailed analysis of the causal relations between the triggering factors and geo-environmental conditions is important for a comprehensive understanding of the landslide distribution patterns triggered by earthquakes.

This chapter presents the results of an extensive mapping study of the landslide distributions triggered by the Wenchuan earthquake in Sichuan Province, China. The study aims to contribute to the understanding of the casual mechanisms of landslides and landslide dams triggered by the Wenchuan earthquake by making a detailed landslide inventory map, and correlating this with seismic, lithologic and terrain parameters.

2.2 Tectonic setting and earthquake characteristics of the study area

On 12 May 2008, the M_w 7.9 (USGS, 2008) Wenchuan earthquake occurred in the Longmen Shan region at the eastern margin of the Tibetan Plateau, adjacent to the Sichuan Basin (See Figure 2.1). The area is characterized by elevations of up to 7500 m above sea level and by topographic variations of more than 5 km over distances of less than 50 km. The earthquake triggered a large number of landslides, rock avalanches, debris flows etc. Some of the landslides formed natural dams in the rivers, with the potential secondary hazard of the subsequent flooding. One third of the estimated 88,000 casualties of the earthquake were considered to be caused by landslides (Wang et al., 2009).

The present-day Longmen Shan region is roughly coincident with the position of a Mesozoic collisional plate margin that developed during the closure of the Paleo-Tethys and the collision of the Qiangtang block with the North China-Kunlun-Qaidam and South China blocks (Li et al., 2003). Wang and Meng (2009) stated that the Longmen Shan fault belt was first formed as an intercontinental transfer fault, partitioning the differential deformation between the Pacific and Tethys tectonic domains, initiated in the late Paleozoic-early Mesozoic period and continued to the Late Cretaceous. From the northwest to southeast, the eastern margin of the Tibetan Plateau is composed of three major tectonic units: the Songpan-Ganzi Fold Belt, the Longman-Shan Thrust Belt, and the Longmen Shan Foreland basin (Li et al., 2003). The southeastward extrusion of the Songpan-Ganzi block, which obliquely collided with the foreland basin, resulted in three large thrust faults in the Longmen Shan tectonic boundary: the Wenchaun-Maowen fault, the Yingxiu-Beichuan fault and the Pengguan fault (Wang and Meng, 2009) (See Figure 2.1). These faults accommodated significant crustal shortening during the Late Triassic Indosinian Orogeny (Li, Y et al., 2003), which has led to the identification of the Longmen Shan region as a major thrust zone that was reactivated in the India-Asia collision (Xu and Kamp, 2000). During the collision, a complex package of rocks, including Triassic marine sedimentary rocks of the Songpan-Ganzi remnant ocean basin (Zhou and Graham, 1996), was thrust to the southeast over the margin of the South China block, creating a Late Triassic foreland basin. After the earthquake, extensive tectonic research was carried out in the eastern margin of the Tibet Plateau (Jin et al., 2009; Zhang et al., 2009; Tang et al., 2009; Wang and Meng, 2009).

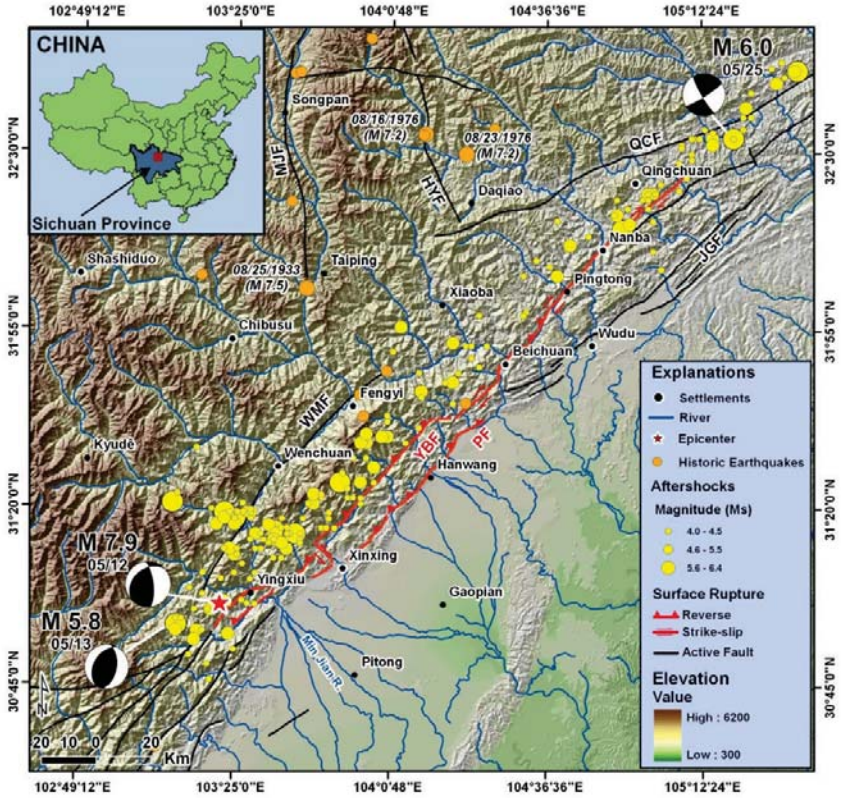

Figure 2.1 Location and 12 May 2008 Wenchuan earthquake fault surface rupture map, and focal mechanisms of the main earthquake (12 May) and two of the major aftershocks (13 May and 25 May). Also the epicenters of historic earthquakes are indicated. The following faults are indicated: WMF: Wenchuan-Maowen fault; BF: Beichuan-Yingxiu fault; PF: Pengguan fault; JGF: Jiangyou-Guanxian fault; QCF: Qingchuan fault; HYF: Huya fault; MJF: Minjian fault Based on the following sources: (Surface rupture: Xu et al., 2009; Epicenter and aftershocks: USGS 2008; Historic earthquakes: Kirby et al., 2000; Li et al., 2008; Xu et al., 2009).

Densmore et al. (2007) and Li, Y. et al. (2003) indicated that the Longmen Shan fault zone represents the features of thrusting and dextral strike-slip in late Cenozoic. The dextral strike-slip rate of the Yingxiu-Beichuan fault since the late Pleistocene is less than 1 mm/year, and the thrust rate is 0.3-6 mm/year. Such low slip rates are consistent with GPS estimates of the shortening rate across the Longmen Shan range of < 3 mm yr^{-1} (Shen et al., 2009; Xu et al., 2009).

There is historic information on 66 earthquakes since 638 AD with M_s larger than 4.7 that occurred in the eastern margin of the Tibetan Plateau, mainly concentrated on the Minjiang fault and the southern part of the Longmen Shan

fault zone (Li et al., 2008). For instance, in 1933, a strong earthquake (M_s 7.5) was induced by the tectonic activity along the Minjiang fault zone. Two earthquakes with Magnitude M_s 7.2 earthquakes occurred between Songpan and Pingwu on August 16 and 23, 1976 (See Figure 2.1). Along the middle and southern part of the Longmen Shan fault zone, three earthquakes were reported: in 1657 (Wenchuan with M_s 6.5), 1958 (Beichuan with M_s 6.2) and 1970 (Dayi with M_s 6.2) (Kirby et al., 2000; Li et al., 2008; Xu et al., 2009).

The Wenchuan earthquake, with a focal depth of ~14 km to 19 km, initiated close to the base of the Beichuan fault and propagated upwards. Seismological data indicate that the rupture initiated in the southern Longmen Shan and propagated unilaterally toward the northeast, along a northwest dipping fault for about 320 km (Xu et al., 2009). The earthquake ruptured both the Beichuan (about 240 km long) and Pengguan faults (72 km long), which are linked by a short northwest-striking rupture zone at the southern end of the Pengguan fault through a lateral ramp, called the Xiaoyudong rupture zone. East of Yingxiu, the Beichuan fault branches into two segments. The largest surface slip (about 6.2m vertical and 4.5m right-lateral offset motion) is found near Yingxiu town and the branching point of the two segments. Another peak of coseismic surface offsets is found near Beichuan, located at a fault juncture, where the Beichuan fault bends about 25° clockwise and almost intersects with the Wenchuan-Maowen fault (Shen et al., 2009). The geometry of the fault changes along its length: in the southwest the fault plane dips moderately to the northwest but becomes near vertical in the northeast. Associated with this is a change in the motion along the fault from predominantly thrusting to strike-slip (Shen et al., 2009 and Xu et al., 2009). This is also illustrated in Figure 2.1, where the aftershock of the May 25 occurring in the NE part of the area has a clear strike-slip component.

After the Wenchuan earthquake, research was carried out on the seismic mechanism and characteristics of the Longman-Shan fault zone (Burchfield et al., 2008; Wang and Meng, 2009), the location and offsets of the surface rupture, the slip distribution, the fault geometry, the slip rate and kinematic characteristics, based on field investigation and measurements, and the coseismic deformation observed using GPS and InSAR (Xu et al., 2009; Shen et al., 2009; Li et al., 2008; Li et al., 2009). Research on landslide distribution and characteristics was carried out by several authors. Huang and Li (2009) studied the distribution of what they called “geohazards” triggered by the earthquake. They identified a total of 11,300 landslide initiation points on the basis of a

rapid inventory using air photos and satellite images. Sato and Harp (2009) carried out a preliminary study on landslides interpretation by using pre- and post-earthquake FORMOSAT-2 imageries. Wang et al. (2009) presented preliminary investigation results of some large landslides triggered by the earthquake. Yin et al. (2009) analyzed the distribution of earthquake-induced landslides and the characteristics and mechanism of some typical landslides, and assessed the hazards caused by some of the landslide dams. Tang et al. (2009) developed a numerical rating system, using five factors that contribute to slope instability to assess the landslide susceptibility in Qingchuan County, Sichuan. Studies on landslide dams induced by the earthquake were carried out by Cui et al., (2009) who listed more than 200 landslide dams in the earthquake-hit region and made a preliminary risk evaluation of some key landslide-dammed lakes. Xu et al. (2009) presented a statistical analysis of the distribution, classification, characteristics and hazard evaluation of 32 main landslide dams induced by the earthquake. Liu et al. (2009) studied the largest barrier lake, Tangjiashan, and presented a risk analysis, emergency planning and the effect of emergency measures.

2.3 Methodology and input data

The methodology used in this research, which is presented in Figure 2.2, consisted of two main steps. The first step was to generate the inventory of landslides triggered by the Wenchuan earthquake, and the second step was to correlate this with a series of parameters to investigate the causal relationships. In the study, three different datasets were used: (1) Pre- and post-earthquake satellite images, (2) a pre-earthquake grid-based Digital Elevation Model (DEM) and DEM derivative factors (elevation, slope gradient, etc.) having a spatial resolution of 30m x 30m of the study area, (3) scientific papers, reports and maps which are related to the study area before and after the earthquake. In addition to these, fieldwork was carried out in May and June 2009 to understand the general distribution pattern. Geo-spatial and remote sensing data analysis was conducted with ArcGIS, SAGA, and ERDAS Imagine software. Remote sensing images have been extensively applied to landslide studies (Rengers et al., 1992; Mantovani et al., 1996; Metternicht et al., 2005; Weirich and Blesius, 2007). A landslide inventory is the simplest form of landslide mapping, which records the location, the date of event and types of landslides (Guzzetti, et al., 2000; Guzzetti, 2005; van Westen, et al., 2008). Inventory maps can be prepared by different techniques, depending on their purpose, the extent of the area, the scales of base maps, satellite images and aerial photographs, the

quality and detail of the accessible information, and the available resources to perform the work (Guzzetti et al., 2000). In this research, the spatial locations of the event-based individual landslide initiation areas were detected from the pre- and post-earthquake satellite images.

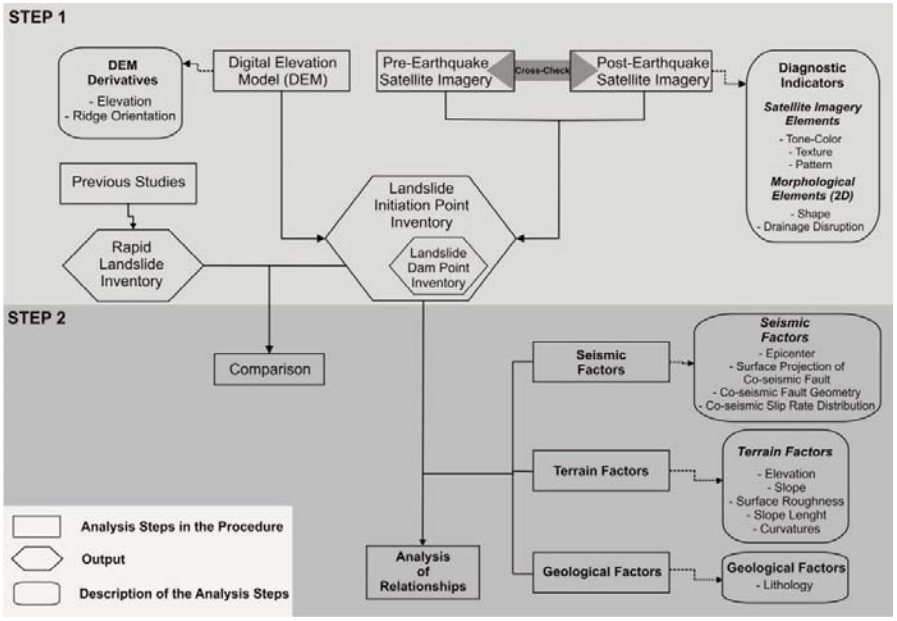

Figure 2.2 Flowchart indicating the method used for generating the event-based point inventory of landslides caused by the Wenchuan earthquake.

Figure 2.3 indicates the spatial coverage of the satellite images that were collected for both the pre- as well as the post-earthquake situation. A total of 52 satellite images were collected: 26 representing the pre- and the post-earthquake situations (See Figure 2.3). The pre-earthquake images consisted of multispectral data such as ASTER (Advanced Spaceborne Thermal Emission and Reflection Radiometer-15 m spatial resolution) and ALOS (Advanced Land Observing Satellite- AVNIR-2 (10 m)) as well as panchromatic data from ALOS PRISM (2.5 m) and the Indian Cartosat-1 (2.5 m). Post-earthquake images also included SPOT-5 (2.5 m) and IKONOS (2.5 m) data (Table A1 in appendix). Most of the satellite images were chosen among the images with low cloud-shadow coverage. The aerial coverage of the cloudy and shadow areas is 192.7 km^2 in the total study area. This area corresponds to 0.5% of the total study area.

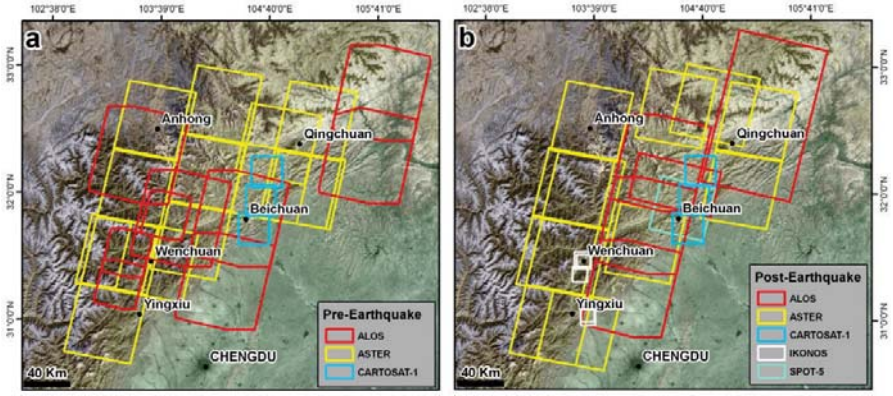

Figure 2.3 Pre- and Post-earthquake satellite image coverage.

The interpretation of landslides was carried out using the pre- and post-earthquake satellite images and the DEM. The DEM was generated using digitized contour lines from 1:50,000 scale topographic maps with contour intervals ranging between 10 meters for low relief areas to 25 meters for mountain areas. The DEM was used to generate a derivative map showing the ridges and slope length. Figure 2.4 illustrates some of the aspects that were encountered while carrying out the interpretation. Several areas exhibited landslides that were present before the earthquake. As can be seen in Figure 2.4a and b some of these landslides were reactivated during the earthquake. In this case only the active landslides that were triggered by the earthquake were mapped. Figure 2.4c and d show an example where a pre-existing landslide was not reactivated during the earthquake. In such cases the landslide was not included in the event-based landslide inventory.

The individual landslide initiation zones were indicated using points. The minimum size of landslide initiation area was determined as 600 m^2 and the areas below this value were not considered since the resolutions of the satellite images were not sufficient. In the case of complex situations where many landslides are interconnected, it was difficult to identify the individual initiation zones. This is illustrated in Figure 2.4e to h. In such cases the convergence index developed by Kothe and Lehmeier (1993) was used to produce ridge and valley orientations to get information for identifying the landslide initiation areas.

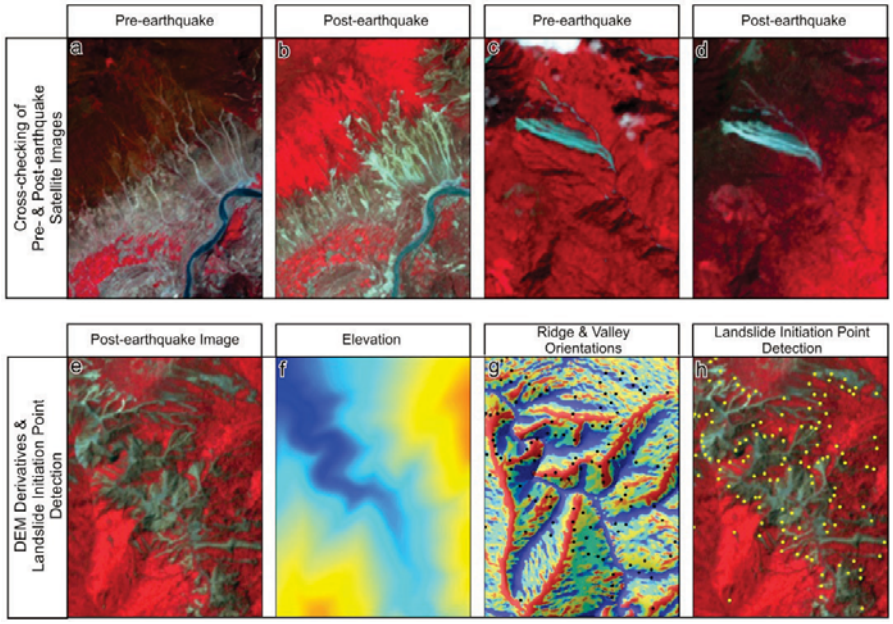

Figure 2.4 Example aspects used in detection of landslide initiation points. Above: cross-checking of landslides with pre-earthquake imagery to avoid double counting of landslides. **(a)** pre-earthquake image showing many landslides in the Wenchuan area; **(b)** post-earthquake image of the same area. Only the new landslides were added to the database; **(c)** Single large landslide existing before the earthquake in Wenchuan County; **(d)** Post-earthquake image showing no major difference in landslide activity. Below: Use of DEM derivatives for detection of landslide initiation points. **(e)** Post earthquake image showing complex landslide polygons that have merged. **(f)** Digital Elevation Model; **(g)** DEM derived map with ridges and valleys used for separating landslide initiation points; h: Final interpretation of landslide initiation points.

The visual landslide interpretation was made using false color composites or panchromatic images, using monoscopic image interpretation. Although stereoscopic image interpretation would be better for optimal landslide interpretation, it was practically not possible to generate stereo images for such an extensive area. In the interpretation we made use of the following diagnostic features (See also Figure 2.5):

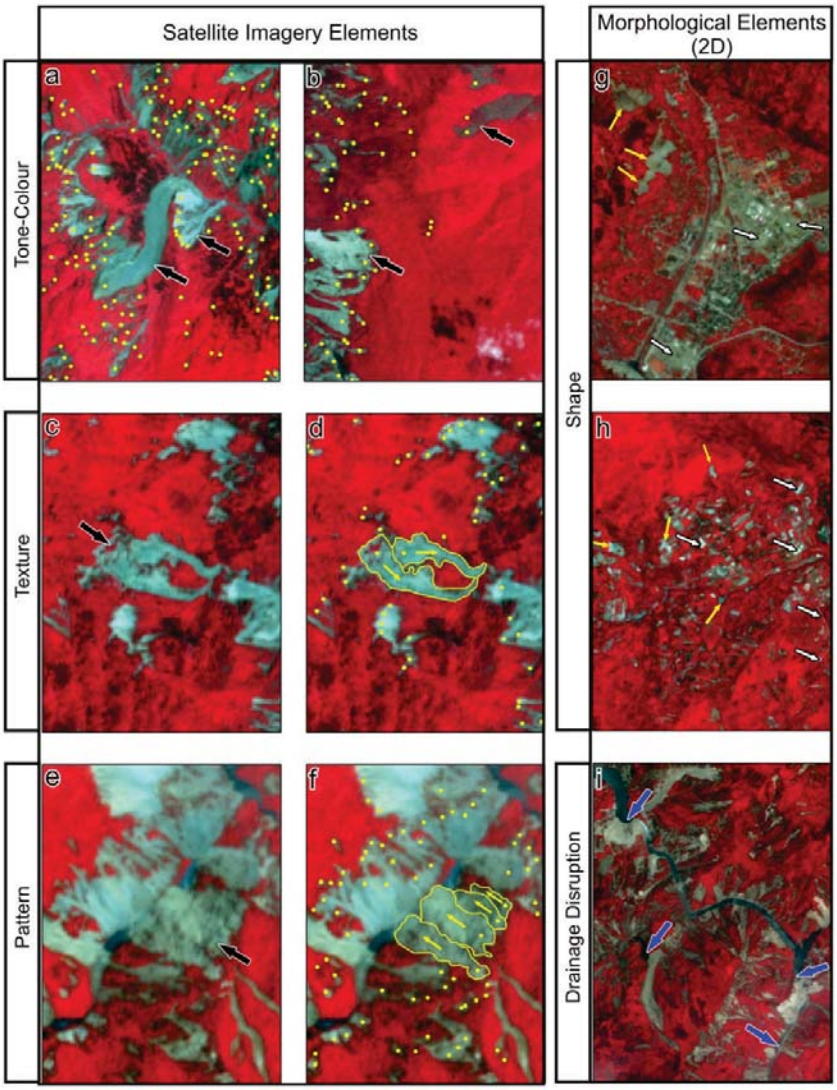

Figure 2.5 Use of image interpretation characteristics for the detection of landslide points. Initiation points are indicated with yellow points. White arrows indicate areas with high reflectance values that are not considered as landslides. Yellow arrows indicated landslides directions, and black and blue arrows represent particular examples of satellite image and morphological (2D) elements. See text for explanation.

- The tone, defined as the relative brightness in a black/white image, or the color in the false color composite allowed differentiating unvegetated areas that are most indicative for recent landslides. Figure 2.5a and b show

examples how differences in color can be used to indicate different landslide initiation areas.

- Texture relates to the frequency of tonal change. It is the result of the composite appearance presented by an aggregate of unit features too small to be recognized individually. This is illustrated in Figure 2.5c and d.
- Pattern refers to the spatial arrangement of features and implies a characteristic repetition of certain forms or relationships. Figure 2.5e and f give an example how this was used for identifying a series of individual initiation points in a large unvegetated area.
- Shape or form refers to the geometric aspects of the object in the image, and association refers to the occurrence of the object of study in combination with other objects that makes it possible to infer about its function or meaning. Figure 2.5g and h indicate how unvegetated landslide initiation points were differentiated from other unvegetated areas, related to urban areas.
- Drainage disruption and existence of lakes were used to identify landslides that have dammed the rivers (see Figure 2.5i). These were mapped as a subset of the entire landslide distribution.

2.4 Landslide distribution analysis

2.4.1 General landslide distribution characteristics

The Wenchuan earthquake produced landslides throughout an area of about 20,000 km^2, from which 8,000 km^2 was highly affected by landslides (Figure 2.6). The landslide inventory map (See Figure 2.6) shows a distinct pattern with higher landslide densities along the surface rupture of the faults and the banks of major rivers. The majority of landslides were concentrated on the hanging wall part of the Yingxiu-Beichuan fault and Pengguen fault, but with a higher density on the former.

From the landslide inventory map, it can be observed that landslides are concentrated in a zone up to 100 km northeast of the epicenter, 15 km west and 4 km east of the fault rupture, and in a northeast-southwest direction along the coseismic fault. Landslides are generally concentrated in the southwest and middle parts of the fault segments. More than 70 percent of the earthquake-induced landslides occurred in the area between Yingxiu and Beichuan towns, which is in agreement with the high vertical displacements measured by Xu et

al. (2009) immediately after the earthquake. In addition, the distribution pattern of landslides was wider (~17 km) around the middle and southwest parts of the surface rupture (between Yingxiu and Beichuan towns) and became narrower (~3.5 km) after 10 km northeast of Beichuan (Figure 2.6).

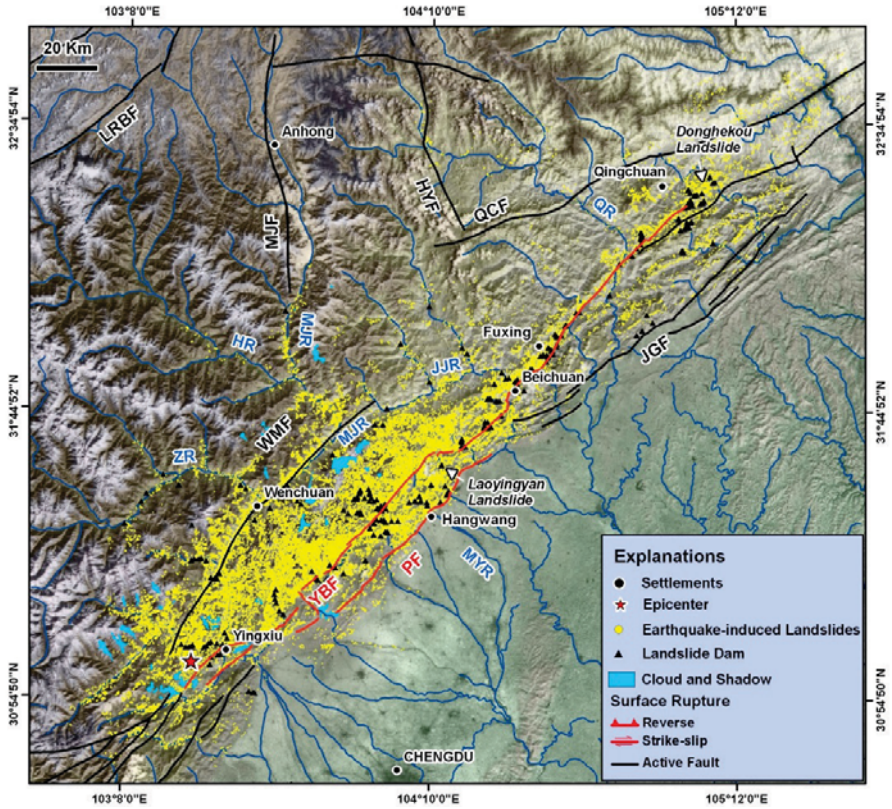

Figure 2.6 Landslide and landslide dam distribution map derived from this study. The map contains 60,104 landslide initiation points and 257 landslide dams. The following rivers are indicated: MJR: Minjiang River; ZR: Zagunao River; HR: Heishuehe River; MYR: Mianyuan River; JJR: Jianjiang River; QR: Qingzhu River. For fault names see Figure 2.1.

Landslides are also frequent on the deeply incised valley side slopes along the Minjiang, Jianjiang, and Zagunao rivers. It is also remarkable how the landslide distribution patterns become much narrower after Beichuan (Figure 2.6). According to our field survey, most of the landslides are smaller and shallower further away from the fault. This trend changes significantly around Wenchuan town and along Min River (Figure 2.6). On the other hand, the landslide density becomes considerably lower from East to West in the southwest section of the surface rupture and the density starts to increase again on both side slopes of the

river. Similarly, the landslide density becomes less towards the side slopes of the Zagunao and Heishuihe rivers, which are tributaries of the Minjiang River. The landslides along the Min River show an asymmetric distribution pattern (Figure 2.6). The presence of the Wenchuan-Maowen active fault (Densmore et al., 2007; Kirby et al., 2000) in this area and long-term tectonic deformation of this fault are considered to be the reason for this asymmetric distribution.

The most common types of landslides were rockfalls, rock avalanches, and rock-debris slides in the area. Deep-seated large landslides were moderately common and these were abundant in the close vicinity of the fault rupture. Most landslides were in highly fractured and jointed Precambrian crystalline and metamorphic rocks, weakly cemented and weathered Paleozoic sedimentary rocks and preexisting landslide deposits. The initiation parts for most of the landslides were very close to prolonged and narrow ridges. Areas with high internal relief show a larger landslide density than those with low relief. However, this difference generally varies depending on the distance from the fault and the lithology.

Landslide density increases in areas where lithologies are highly susceptible to landslides, relatively close to the fault rupture, and with high relief and slope gradient. On the other hand, this situation changes 10 km northwest of Beichuan, where the coseismic fault is transferred from a thrust component to a strike-slip component. Although the relief and slope gradient do not change significantly, the landslides are distributed in a narrow zone.

2.4.2 Comparison of individual landslide inventories

The landslide inventory map with 60,104 landslide points produced in this study (Figure 2.6) was compared with the inventory map that was prepared by Huang and Li (2009) directly after the event, which contains 11,306 individual landslide points (Figure 2.7). The landslide interpretation was carried out by Huang and Li (2009) using high resolution aerial photos and optical satellite images (e.g., ALOS and SPOT-5) for only the post-earthquake situation. The main purpose of this comparison is to analyze the degree of correlation of the newly produced landslide inventory with the previous inventory for the same area.

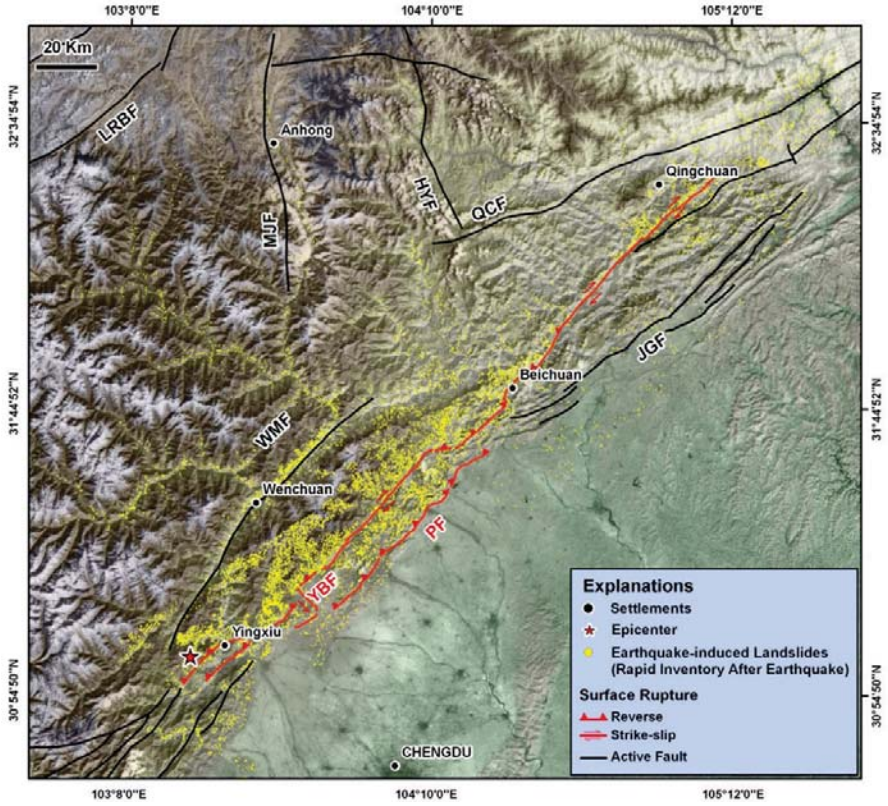

Figure 2.7 Landslide distribution map derived from a rapid landslide inventory made directly after the Wenchuan earthquake by Huang and Li (2009). The map contains 11,306 landslide initiation points.

There are different approaches in the literature for the comparison of landslide inventory maps (van Westen et al., 1999; Guzzetti et al., 2000; Galli et al., 2008). It is possible to group these approaches under two headings: direct and indirect comparison approaches. Direct approaches are based on evaluating the degree of cartographic matching between two maps, and consist of making pair-wise comparisons of the mapped landslides (Galli et al., 2008). The indirect comparison approach considers the correlation of landslide inventories using landslide densities (Guzzetti et al., 2000), frequency-area statistics of landslides (Galli et al., 2008; Martha et al, 2009), and susceptibility or hazard mapping results (van Westen et al., 1999) for inventories based on different expert interpretations or different inventory mapping techniques for the same area.

In this study, a grid-based landslide density analysis was selected for the comparison of the landslide point inventory. A new area was defined to reduce

the number of pixels, with the Longmen Shan mountain front as the eastern boundary and natural catchment boundaries in the West (Figure 2.8). Landslide density maps were prepared for both the individual landslide inventory (ILI) and the rapid landslide inventory (RLI) (Figure 2.8a and b).

The grid-based density maps were produced by counting the percentage of landslide points within a circular moving window with an area of 1 square kilometer, and a pixel size of 90 m. Maximum landslide densities are 54.1/km^2 for the ILI inventory and 21.2/km^2 for RLI. The grid-based density maps were normalized by dividing each cell value by the maximum density. After the normalization, the two maps were compared by ranking both with respect to the density classes (<2%, 2%–10%, 10%–45%, and >45%; see Figure 2.8a and b). High (>45%), medium (10%–45%), low (2%–10%), and very low (<2%) density classes were obtained applying the ranking process, which enabled the comparison of both density maps in a relative manner.

After applying the normalization procedure, analysis of the spatial correlation became possible for the values obtained from both density maps. Finally, a density difference map was produced by subtracting the density maps (ILI – RLI). The values of the density difference map range between 0.86 and -0.51 (Figure 2.8c). The positive and negative extreme values correspond to areas with high differences. The landslide density differences and spatial correlation graph allowed to compare both density maps.

From Figure 2.8 it can be observed that both the visual and spatial correlations (Figure 2.8d) are low between the two maps. For instance, while some of the landslide complexes have been represented with a single point in the rapid inventory immediately after the earthquake, the new inventory study determined more than 20 single landslides within the same landslide complex. According to a proximity analysis between the common landslides in both inventory maps, the average difference between the landslide locations is 82 m. This is mostly due to the fact that the rapid damage inventory did not follow clear criteria for mapping only landslide initiation areas, as was done for the inventory prepared in this study. Therefore many landslide points were located in the run-out area. The rapid landslide inventory was also based on partially on image interpretation, and landslide points were concentrated in areas where landslides were large and considered dangerous by the group of people mapping them in the field.

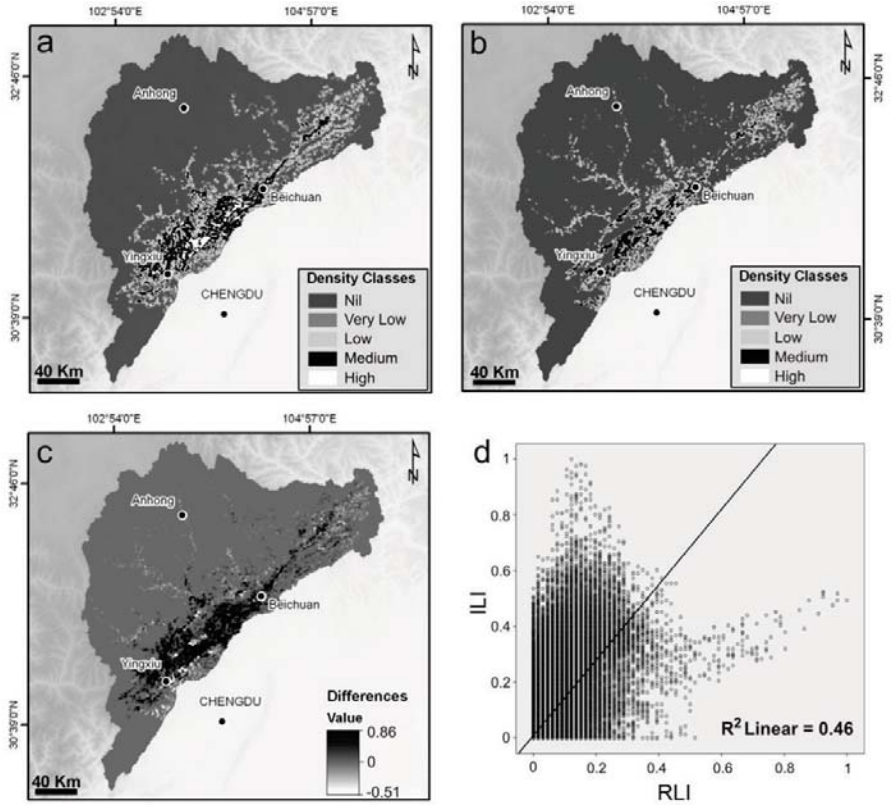

Figure 2.8 Comparison between the inventory maps of landslide initiation points triggered by the Wenchuan earthquake. **(a)** Density map of individual landslide inventory; **(b)** Density map of rapid landslide inventory; **(c)** Density difference map; **(d)** Spatial correlation graph of landslide densities. ILI: Individual landslide inventory (this study); (RLI) rapid landslide inventory (Huang and Li, 2009). See text for detail explanation.

2.5 Characteristics and distribution of landslide dams

The Wenchuan earthquake generated at least 257 landslide dams according to the preliminary interpretation of Cui et al. (2009), but due to difficulty of access, to date we only collected field data for 32 landslide dams (Xu, Q. et al., 2009). Based on the previous field investigation and Cui et al.'s (2009) interpretation the distribution of the 257 landslide dams is shown in Figure 2.6. After the earthquake, one of the most important problems that the Chinese government needed to deal with was evaluating the potential hazards of landslide dams in the densely populated region and making the right decision rapidly to take appropriate counter measures to reduce the risk. An empirical method was implemented to appraise the hazard of the 32 comparatively

dangerous dams (Xu, Q. et al., 2009 and Cui et al., 2009). The height and constituent material of landslide dams as well as the maximum capacity of barrier lakes were selected as the criteria to rank the landslide dam hazard.

Zhang et al. (2009) presented the characteristics and treatment measures of 10 barrier lakes triggered by the Wenchuan earthquake. They classified landslide dams into two types: dams formed by rock blocks and loose deposits. The largest barrier lake, Tangjiashan with a storage capacity of 316 million m^3 was the most threatening and received most attention. Wang, G.Q. et al. (2008) proposed a physically-based numerical simulation approach for real-time prediction of dam breach development of the Tangjianshan barrier lake. Liu et al. (2009) presented the risk analysis, emergency countermeasures and their corresponding effects on the Tangjiashan landslide dam. Most of landslide dams triggered by the Wenchuan earthquake had to be evaluated very rapidly, once they were formed. Exploring for a method of rapid assessment of landslide dam hazard is much needed and worthy of further research. On the basis of preliminary field investigations, we observed that the landslide dam composition materials and sedimentologic structure play important roles in landslide dam stability and hazard assessment. For example, landslide dams composed by unconsolidated fine materials such as the Donghekou landslide have lower stability compared to those composed by rock blocks and boulders such as the Laoyingyan landslide dam. The Donghekou landslide dam failed by naturally overtopping only 4 days after it was created, while the Laoyingyan landslide dam is still stable so far. We estimated that the main reason is that the different erosional resistance capacity, dam strength and permeability are determined by the composition materials and dam structure.

2.6 Analysis of relations with seismic and geo-environmental factors

The relation between the landslide distribution pattern and three main types of factors: seismic (seismic source parameters and coseismic slip), lithologic and topographic factors, was analyzed. A statistical analysis was carried out using geologic maps digitally compiled by Chengdu Institute of Geology and Mineral Resources (2004) and a DEM produced by digitized contour lines from 1:50,000 scale topographic maps. In this study, the seismic factors were obtained from the China Earthquake Administration (CEA, 2008), Xu et al. (2009) and Shen et al. (2009), respectively.

The landslide concentration (C_L) index (Keefer, 2000; Wang, H.B. et al., 2007) can be used to reflect the influence of landslide occurrence, which is defined as the number of landslides per square kilometer. Based on this definition, the analysis was conducted for an area of 34608.3 km^2 that contained 60,104 individual landslides. The average landslide concentration ($C_{L\ average}$) in the study area was calculated and the result shows that it equals to 1.73/km^2 (60,104/34608.3 km^2).

2.6.1 Relation with seismic factors

The relation of landslide (dam) concentration was investigated using three different seismic factors: the epicentral distance, the surface projection of the fault rupture (Xu et al., 2009), and the coseismic slip (Shen et al., 2009). With the assistance of GIS, landslide concentration (C_L) and landslide dam concentration (C_{LD}) were determined for a sequence of concentric bands 2 km wide extending outward (buffer) from the source (epicenter and surface projection of the fault rupture).

Figure 2.9a and b shows the variation of C_L and C_{LD} with epicentral distance. The highest C_L value was calculated as 8.4 landslides/km^2 in the area within 8 km from the epicenter. The highest C_{LD} value, 0.08 landslide dams/km^2, appeared in the area within 6 km from the epicenter. C_L values show significant peak values rather than decreasing gradually. These peaks are especially significant between the epicentral distances of 50-58, 80-96 and 224-230 km (Figure 2.9a). Additionally, the standard error values of C_L and C_{LD} with epicentral distance are considerably high having values of 0.59 for C_L and 0.72 for C_{LD} respectively.

Contrary to other studies (Keefer, 2000; Khazai and Sitar, 2003; Wang et al., 2007) we found no obvious relation between the distance from the epicenter and C_L as well as C_{LD} (Figure 2.9a and b). In other words, the landslide and landslide dam distribution are not controlled by the distance from the epicenter, and may be dominated by other factors.

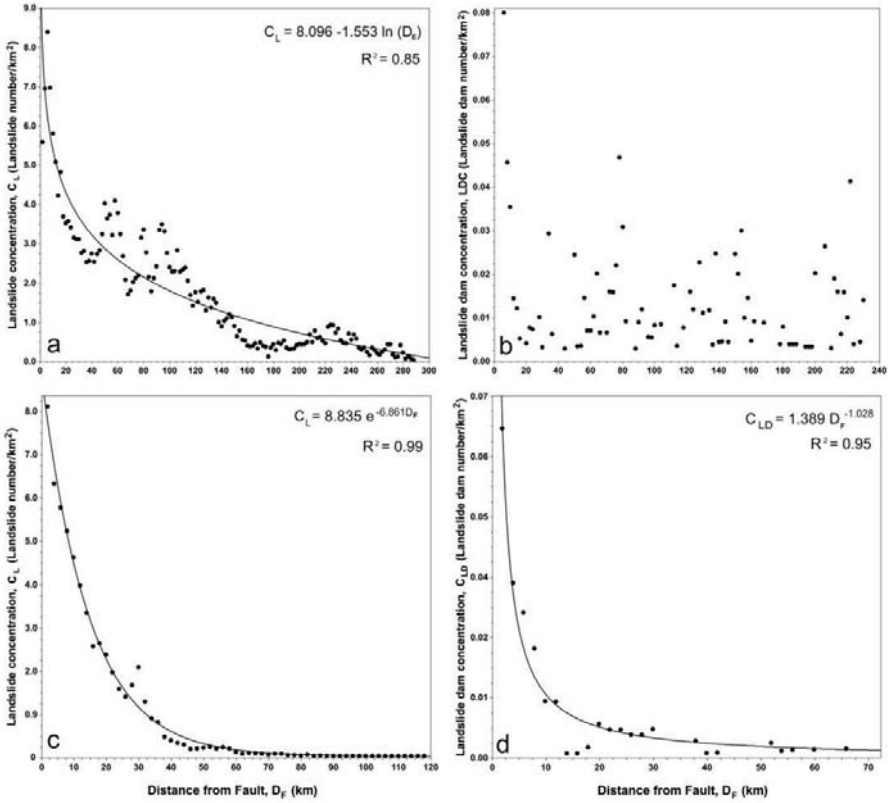

Figure 2.9 Relationship between landslide (dam) concentration and distance from epicenter and fault. **(a)** Distance from epicenter for all landslides; **(b)** Distance from epicenter for landslide dams; **(c)** Distance from fault rupture for all landslides; **(d)** Distance from fault rupture for landslide dams.

Figure 2.9c and d show that the variation of C_L and C_{LD} has a strong inverse correlation with the distance from the surface rupture of the fault. C_L values descend from 8.0/km^2 at D_F =2 km to 5.2/km^2 at D_F =8km, while C_L values decrease from 0.066 landslide dams/km^2 at D_F =2 km to less than 0.012 landslide dams/km^2 at D_F =10 km. C_L and C_{LD} values are fitted best empirically with regression equations having an exponential form and power law form respectively, as shown in equation (1) and (2).

$$C_L = 8.835\, e^{-6.861 D_F} \quad (R^2 = 0.99, S=0.1801) \tag{1}$$

$$C_{LD} = 1.389\, D_F^{-1.028} \quad (R^2 = 0.95, S=0.0029) \tag{2}$$

where, C_L and C_{LD} refer to landslides and landslide dams per square kilometer respectively, D_F is the distance to the surface projection of the fault rupture in

kilometers, S is the standard error. Both the C_{LD} and C_{LD} variation versus the distance from the ruptured fault show that the occurrences of landslides and landslide dams are strongly concentrated around the high seismic zone, near the ruptured fault zone. On the other hand, a peak of C_L is found at a distance of 28-30 km from the surface rupture (Figure 2.9c), corresponding to the Wenchuan-Maowen Fault Zone located along the Minjiang River. This is an active fault system at the western branch of the Longmen-Shan Thrust Fault, which was not ruptured during the Wenchuan earthquake. While the landslide density decreases gradually with increasing distance from the surface rupture, the density increases again in the 28-30 km distance band (Figure 2.10). For better visualization of this phenomenon, the map was cropped in the part where the Wenchuan-Maowen fault ends (NE). According to the map (Figure10 inset map), C_L values are very high (~5.8/km^2) up to 14 km distance from the surface rupture, while the C_L values decline to ~3.6/km^2 (High) between 14-26 km, and then increase again to very high C_L values in the 28 km distance band where Wenchuan-Maowen fault is located (Figure 2.10).

Besides the distance from the epicenter and surface rupture, the relation of C_L with coseismic slip was investigated (Figure 2.11). The landslide distribution pattern was compared with coseismic slip values determined by Shen et al. (2009), which correspond with field measurements of slip-rate by Xu et al. (2009). Shen et al. (2009) have used Global Positioning System (GPS) and Interferometric Synthetic Aperture Radar (InSAR) data to infer fault geometry and slip distribution associated with the earthquake. Their study shows that the geometry of the fault changes from the epicenter towards the northwest. In the southwest part, the fault plane dips moderately to the northwest but becomes nearly vertical in the northeast. Associated with this is a change in the motion along the fault from predominantly thrusting to strike-slip. Peak slip along the fault occurs at the intersections of fault segments located near the towns of Yingxiu, Beichuan and Nanba, where fatalities, damage, and landslides were highest (Shen et al., 2009).

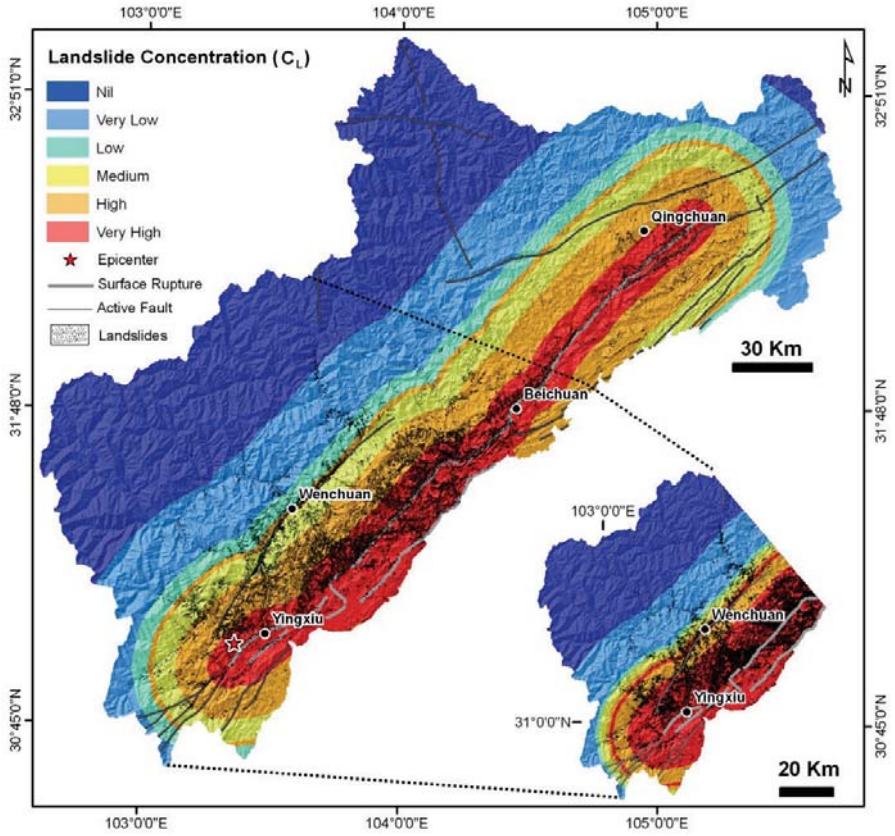

Figure 2.10 Landslide concentration in relation to the distance to the fault rupture.

The coseismic slip values determined by Shen et al. (2009) and the projection of coseismic fault plane borders (surface and dip edge of Yingxiu-Beichuan fault rupture) were used in our study for the analyses of the landslide distribution pattern. C_L values which were calculated for the whole area (Figure 2.11a) were clipped using the defined fault plane borders (Figure 2.11b), and were depicted as isopleths. As a result, the C_L values range between 0.005-0.080 (Figure 2.11b), with peak values at 35 km NE of Yingxiu and at 25 km SW of Beichuan town. When the results are compared with the coseismic slip map (Figure 2.11c), it is observed that these peak areas also correspond to the high coseismic slip values. In addition, C_L values show a narrow pattern particularly in the zone starting 10 km NE of Beichuan town (Figure 2.11c). There is a clear relation between the isopleths of landslide concentration and coseismic slip values (Figure 2.11d). As mentioned before, this area corresponds to the area where the fault geometry and the fault plane dips are almost vertical. Apart from this, in

the SW part where the thrust component of the fault is high (Shen et al., 2009; Xu et al., 2009; Lin et al., 2009), the fault plane dips is less steep and dips with an angle of 49° on average.

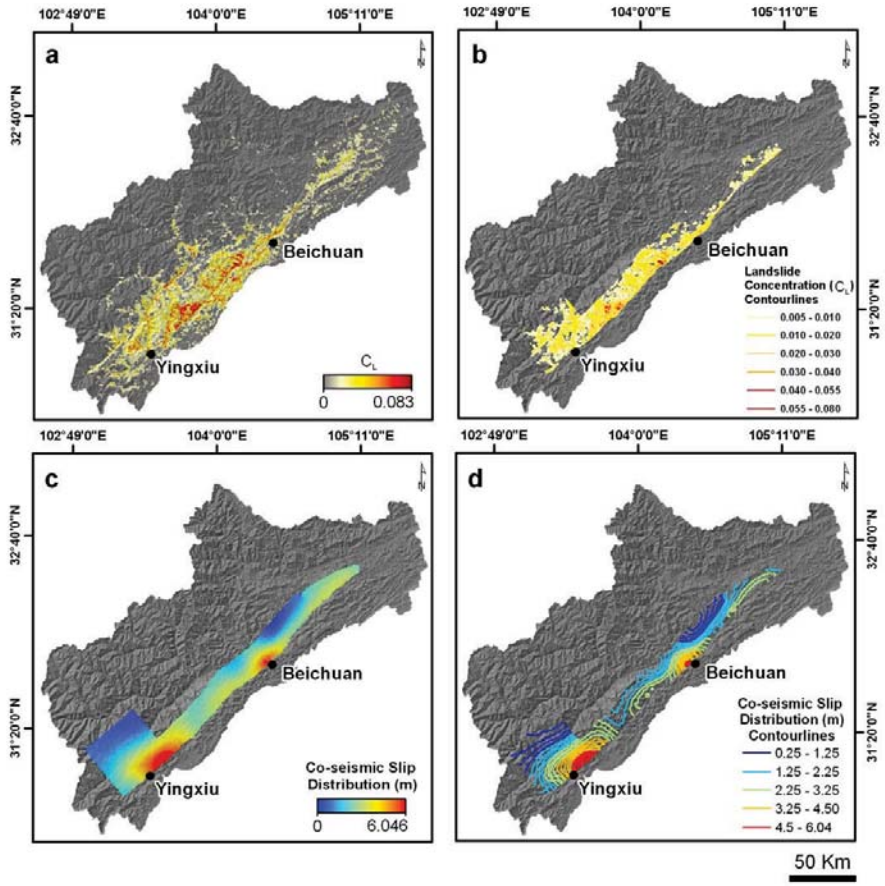

Figure 2.11 Landslide concentration in relation to the total coseismic slip distribution of the fault rupture (coseismic slip distribution model is from Shen et al., 2009). **(a)** the landslide concentration; **(b)** contour lines of landslide concentration clipped for the projected fault plane boundary; **(c)** the coseismic slip distribution; **(d)** Contour lines of coseismic slip distribution.

In this zone landslides are distributed over a larger area as compared to the northeast part. The comparison of the coseismic slip rate and landslides (Figure 2.12) indicates that landslide concentration increases with increasing coseismic slip up to a certain maximum of 10 landslides/km^2. On the other hand, the linear association between landslide concentration and coseismic slip breaks down at this certain level. This further implies that landslide concentration and coseismic slip are nonlinearly related and rather demonstrate a power trend.

2.6.3 Relation with topographic factors

In order to assess the potential influence of topography on coseismic landsliding, we extracted landslide density plots of the local relief H and the slope gradient S_h in areas with abundant landsliding (Figures 2.12a and b). Detailed information on the generation of these factors from DEMs is provided by Wilson and Gallant (2000) and Hengl and Reuter (2009). Local relief and slope gradient have a nonlinear relationship with landslide density (Figures 2.12a and b). Landslide density increases in a roughly linear fashion with both local relief and hillslope gradient from H ~200 to 850 m and S_h 2° to 30°, respectively, but then increases rapidly near the H ~1050-1200 m and S_h ~35° to 40°. By comparison, mean slope gradients in the earthquake struck region are between 30° and 38°, with isolated areas >40°, while mean slope gradients in the basin are lower (<10°), with very few areas >15°. The mean values show a considerable dissimilarity between the grid cells with landslides and without landslides (35° and 26° respectively). Thus, suggesting that the coseismic landslides in the region commonly occurred on the grid cells having moderately high values of slope gradients.

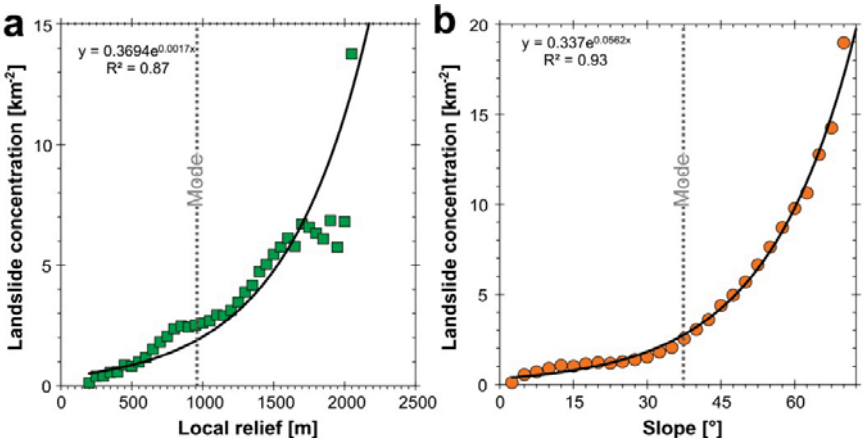

Figure 2.12 Landslide density versus local relief **(a)** and slope gradient **(b)**. The linear increase in landslide density grows significantly above the common mode of local relief and slope gradient.

2.7 Discussion and Conclusion

This study aimed to generate a comprehensive data base of landslides triggered by the Wenchuan earthquake, based on multi-temporal image interpretation, and to correlate these with seismic and environmental factors. The landslide interpretation focused on the mapping of landslide scar areas in a very extensive

area covering around 35,000 km^2. The landslide points were indicated in the scarp areas, using a number of interpretation criteria and comparison with pre-earthquake satellite images. Unfortunately it was not possible to use stereo image interpretation techniques, due to time constraints and the unavailability of a high resolution DEM for generating the stereo images. Given the above mentioned constraints a database was generated containing more than 60,000 individual landslide scarps, which were triggered by the Wenchuan earthquake. This might be one of the largest numbers of landslides triggered by a single earthquake event in historical times. Recent other earthquakes in mountainous areas triggered substantially fewer landslides: the Northridge earthquake (M_w=6.7, 1994) triggered around 11,000 landslides (Harp and Jibson, 1995), the Chi-chi earthquake (M_w =7.6, 1999) caused 22,000 landslides (of which 9272 larger than 625m^2) affecting an area of 128 km^2, and the Kashmir earthquake (M_w =7.6, 2005) caused only 2252 landslides (larger than 625 m^2) (Dunning et al., 2007). The earthquake also triggered more landslides than the ones reported by recent hurricane events, such as Hurricane Mitch which caused over 9594 landslides in Guatemala, and comparable numbers in Honduras and El Salvador (Bucknam et al., 2001).

In this study, we only derived the number of landslides, as landslides were mapped as individual points. Therefore the total landslide area cannot be defined. Keefer (1984) studied the relationship between the total volume of landslides triggered by an earthquake and the earthquake's moment magnitude. If we assume an average landslide area as indicated by Malamud et al. (2004) of 3.07 x 10^{-3} km^2 the total landslide area would be 184 km^2 which would put this event in the upper right corner of the relation between magnitude and landslide area. The landslide magnitude of this event would be around 4.8 (log N_{LT}). When we apply the N_{LT} (number of total landslides in an event) of 60,000 in the equations of Malamud et al. (2004) the resulting values for total landslide area (184 km^2) and volume (1.68 km^3) appear to be too low for this event.

In our study we found that the distribution of earthquake-induced landslides for the Wenchuan earthquake is primarily controlled by the fault rupture. The landslide distribution shows a very distinct "hanging wall" effect, and most of events occurred within a 10 km range from the fault. It is observed that the 76% of all landslides occurred on the hanging wall of the Yingxiu-Beichuan fault and 13% on that of the Pengguan fault. The distribution of landslides is within two main concentration zones; one is the area along the coseismic rupture, and the other is along the deeply incised valley-side slopes of the Min River system.

Besides of these, the landslide distribution patterns changes significantly northeast of Beichuan town and has a narrowing pattern. This narrowing of the high density landslide area could be explained well by the change in fault geometry. The main thrust component transfers to a strike-slip component 10 km beyond Beichuan town (Xu et al., 2009; Lin et al., 2009) and the fault dip angle changes from approximately 45° in the southwest to 65-80° after Beichuan town.

The landslides along the Min River show a clear asymmetric distribution pattern. According to our field survey, most of the landslides in this zone occurred on the hanging wall block of the Wenchuan-Maowen Fault, and from the image interpretation, using the pre-earthquake satellite images, it was determined that there were many active and dormant landslides before the earthquake. These landslides were re-activated by the Wenchuan earthquake. The presence of Wenchuan-Maowen active fault (Densmore et al., 2007; Kirby et al., 2000) in this area and the long-term tectonic deformation of this fault can be considered as the reason for this asymmetric distribution. In this regard, long-term tectonic deformation characteristics and the existence of active faults, which were not ruptured during earthquake, are important in terms of earthquake-induced landsliding. Although there is also a relation with lithology, this is not as clear as the relation with the seismic factors. The clear relation reported by D.N. Petley (personal communication, 2009) of landslides with igneous rocks could not be confirmed by our study, also because we studied a larger area and used a more detailed lithological map.

Looking at the landslide distribution in terms of terrain factors, it is observed that 53.2 % of the earthquake-induced landslides occurred in the transition zone between highly dissected hilly topography and moderately high mountainous topography. This transition zone is observed between 1750-1950m and expresses moderately high topographic slope (35°-40°), convex slope and high roughness characteristics in terms of terrain factors. It was determined that the areas with such terrain values also relate to the high landslide density areas.

3 Controls on earthquake triggered landslides in strike-slip tectonic environments, 2002 Denali Fault earthquake[1]

3.1 Introduction

The M_w 7.9 Denali Fault earthquake struck the South-central Alaska and the Alaska Range at 13:12 local time (22:12 UTC) on 3 November 2002. It was one of the largest earthquakes in U.S. history, rupturing along three major faults in the interior of Alaska over a distance of 340 km in 100 seconds. The earthquake hypocenter was at 18.44° N, 72.57° W (U.S. Geological Survey, 2002), at a depth of 5 km on an east-northeasterly striking plane (Figure 3.1). The Alaska Earthquake Information Center placed the location and mechanism for this event as the rupture of the multiple faults, mainly the dextral Denali Fault (DF) zone, which is part of a system of active intra-continental strike-slip fault accommodating contemporary deformation (8-9 mm yr^{-1}) along the North American–Pacific plate boundary.

Geological and seismological observations show that the Denali Fault earthquake originated with thrust motion on the Susitna Glacier Fault, with an average dip slip of 4 m (Haeussler et al., 2004). The earthquake then ruptured along 226 km of the Denali Fault where right lateral slip at the surface averaged 4.5–5.1 m, with a maximum of 8.8 m (Haeussler et al., 2004) some 40 km west of the Denali-Totschunda fault junction (Figure 3.1). Finally, the rupture propagated southeasterly another 66 km along the Totschunda fault, where right-lateral surface displacements averaged 1.7 m (Eberhart-Phillips et al., 2003; Haeussler et al., 2004). Inversion of the strong motion records suggests that the main event comprised three subevents (Frankel 2004; Hreinsdottir et al., 2003 and 2006; Ozacar and Beck, 2004). The first occurred near the epicentral area on the 48°N-dipping plane of the Susitna Glacier Thrust Fault. The other two strike-slip subevents were recorded along the Denali Fault following the initial thrust event (Figure 3.1), i.e. a M_w 7.3 subevent 60-100 km east of the epicenter, near where the Trans-Alaska pipeline crosses the fault, and a M_w 7.6 some 40 km west of the Denali-Totschunda fault junction (Frankel 2004;

[1] This chapter is based on the following paper: Gorum, T., Korup, O., van Westen, C.J., van der Meijde, M., Xu, C., van der Meer, F.D., 2013. Controls on earthquake triggered landslides in different strike-slip orogenic belts. *Tectonophysics* (Under-review).

Hreinsdottir et al., 2006), where the maximum surface offset was measured (Eberhart-Phillips et al., 2003).

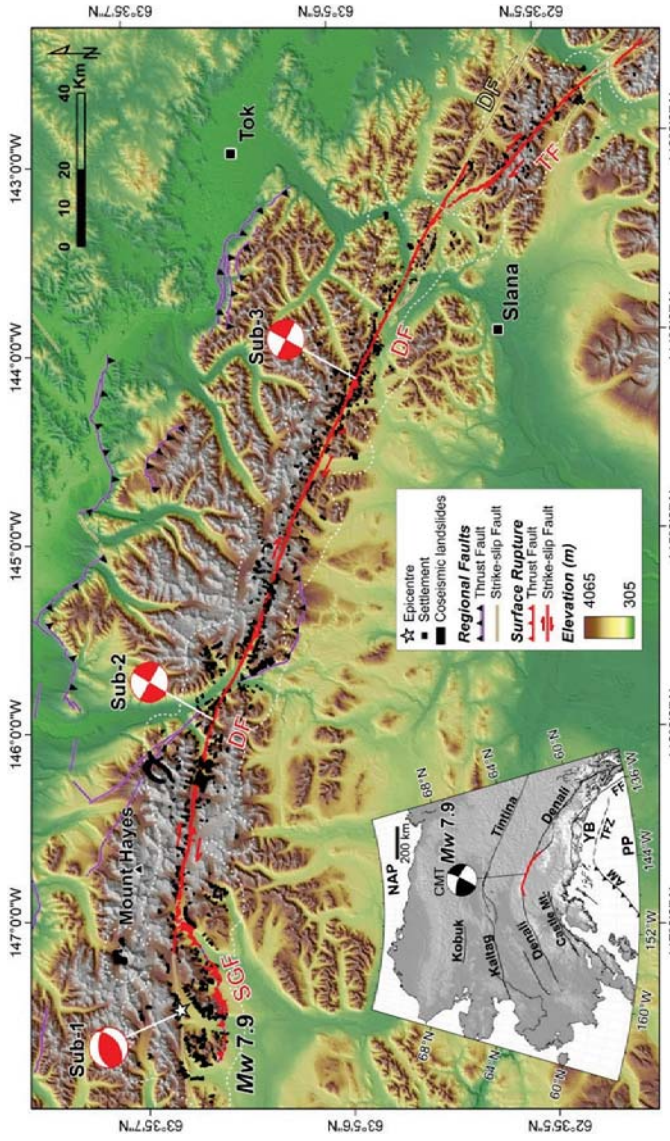

Figure 3.1 Distribution of landslides triggered by the Denali Fault earthquake and tectonic setting of the study area. Red lines indicate surface traces of coseismic rupture (Haeussler, 2009); focal mechanism of the first motion solution (sub 1) and the two largest subevents from waveform inversion (sub 2 and sub 3) (Eberhart-Phillips et al., 2003) are shown in red and white beach balls. the focal mechanism is the Harvard CMT solution for the earthquake. Dashed white lines is region of the high landslide density zone delimited by a landslide area density >0.01 km^{-2}. Inset map shows major tectonic boundaries between the North American plate (NAP), the Pacific plate (PP), and the Yakutat block (YB) and the focal mechanism of the Harvard CMT solution for the earthquake. AM: Alaska megathrust, FF: Fairweather Fault, TFZ: Transition fault zone between Alaska and Yukon terrains.

About 1,000 landslides were attributed to the 2002 Denali Fault earthquake, according to U.S. Geological Survey researchers who undertook aerial reconnaissance shortly after the event (Jibson et al., 2004; 2006). Slope failures included seven rock avalanches with a total volume of 77.5 x 10^6 m^3 that was

deposited on the Black Rapids, McGinnis, and West Fork Glaciers (Jibson et al., 2006). Although these large rock avalanches were studied in detail (Harp et al., 2003; Jibson et al., 2004 and 2006), there is no substantially complete landslide inventory for the earthquake. Compared to other recent landslide-triggering earthquakes such as the 2010 M_w 6.8 Yushu, China, and the 2010 M_w 7.0 Haiti earthquakes, the total volume contained in the seven rock avalanches from the Denali earthquake is 32 times larger than the total volume of landslides generated by these two earthquakes. Yet the Denali Fault earthquake triggered considerably fewer landslides in terms of total area and volume when compared to events of similar magnitude, such as the 2008 M_w 7.9 Wenchuan earthquake (Dai et. al., 2010). Moreover, the other aspect of the landslides triggered by Denali Fault earthquake was their narrow density over a non-circular area around the surface rupture (Figure 3.1). Our mapping results show that the maximum distance of the landslides triggered by Denali Fault earthquake to the surface rupture, excluding some small failures in side-slopes of the Nelchina River about 150 km from the fault, was 24 km. In addition the area affected by landslides was 7,150 km^2 (Figure 3.1). Empirical relationships (Keefer, 1984; 2002; Rodrìguez et al., 1999) suggest that an earthquake of this magnitude would trigger landslides from 250 to 350 km away from the fault rupture, covering an area of 30,000-95,000 km^2. We find that the distance and the extent of the landslides triggered by Denali earthquake are noticeably below these values.

Here, we explore the role of the seismological (i.e. dynamic rupture process, fault geometry, faulting mechanism, and rupture directivity), lithological, and geomorphological controls on the spatial and size distribution of landslides triggered by the 2002 Denali earthquake. Our objectives are (1) to quantify from a substantially complete inventory of ~1,600 coseismic landslides the contributions of complex coseismic slip and mode, high- and low-frequency seismic energy pulses, geomorphological, and rock-type controls to build a better picture of regional distribution pattern of landslides triggered by the Denali earthquake; (2) to compare these results with those from landslide inventories of strike-slip faulting earthquakes, and to determine differences and similarities in coseismic landslide distribution.

3.2 Study Area

Our study focuses on the main epicentral area of the 2002 Denali earthquake in the central and eastern Alaska Range (Figure 3.1), a large mountain belt that

extends for ~950 km, and varies in width from 70 to 200 km. The Alaska Range was built up by the collision of an island-arc with the North American continental margin, which has gradually deformed since the late Mesozoic (Ridgway et al., 2002; Matmon et al. 2006). The relief of the central and eastern range is >3300 m, rising from low foothills at <800 m a.s.l. to the highest peak (4150 m a.s.l.) in the central part. The orographically enhanced climatic contrast is characterized by a cold continental climate on the northern flank, while the southern flanks have a warmer maritime climate (Capps, 1940). The central, high-elevated sections of the range were extensively glaciated during the Last Glacial Maximum (LGM) around 20 ka, though the extent of glaciation was limited along the northern range (Dortch et al., 2010), indicated by rugged mountain relief featuring jagged peaks, serrated ridges, and steep-sided U-shaped valleys.

The regional geology of the study area is closely related to the Denali Fault system which developed in a former suture zone between the Paleozoic continent, and a late Paleozoic island-arc system (Figure 3.2; Richter and Jones, 1973; Csejtey, 1976). This fault system is one of the of the most prominent tectonic features of North America, extending over 2,000 km in an arc-like fashion (Stout and Chase, 1980) from southeastern Alaska to the Bering Sea. The Cenozoic activity and the net fault slip is >38 km over the past 38 Myr (Stout et al., 1973; Reed and Lanphere, 1974). Cosmogenic dating along the central sections of the Denali fault system indicates that the mean late Quaternary slip rate is 12.0 ± 1.7 mm yr^{-1} (Matmon et al., 2006). The areas north of the Denali fault are mainly composed of the Devonian-Mississippian and middle Paleozoic Yukon-Tanana terrane, comprising poly-metamorphosed, deformed metasedimentary, and intermediate-composition metavolcanic rocks, and lower Devonian and Mississippian metagranitic rocks (Figure 3.2; Stanley et al., 1990). Bedrock south of the fault features Paleozoic and Mesozoic sedimentary and volcanic rocks (Hickman et al., 1977). The generally older rocks along much of the north side of the Denali fault indicate that the net vertical slip has been north side up (Stout et al., 1973). Seismicity is high with dominantly medium-sized shallow earthquakes, however for the 30 years prior to the 2002 sequence was infrequent with an average of four earthquakes of M> 3.0 per year (Doser, 2004).

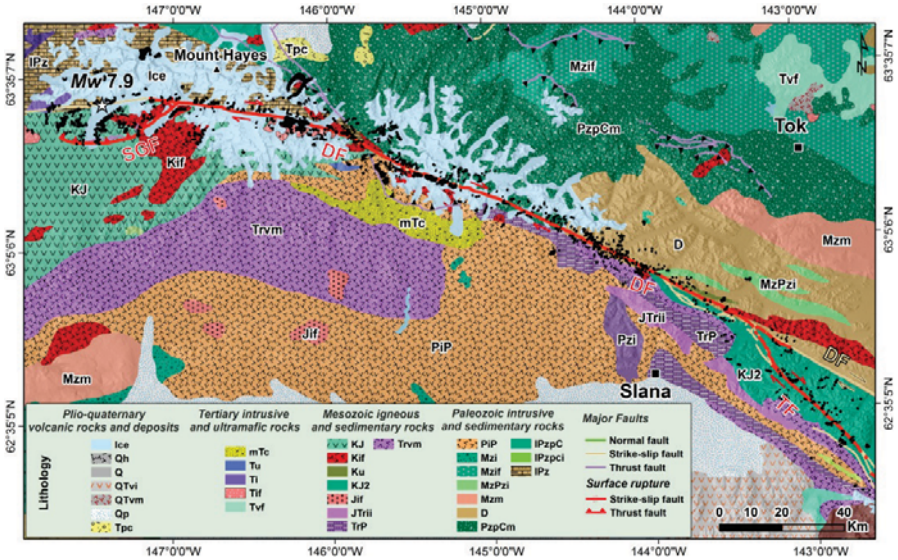

Figure 3.2 Geologic map of the study area (after Beikman 1980). Ice: Ice covered areas, Qh: Holocene deposits, Q: Quaternary deposits, Qp: Pleistocene deposits – alluvial and glacial, QTvi: Quaternary or Tertiary intermediate volcanic rocks - trachyte to andesitic, QTvm: Quaternary or Tertiary mafic volcanic rocks – basalt, mTc: Middle Tertiary continental deposits - sandstone, siltstone, claystone and coal beds, Tu: Tertiary ultramafic rocks, Ti: Tertiary undifferentiated intrusive rocks, Tif: Tertiary felsic intrusive rocks - granite to granodiorite, Tvf: Tertiary felsic volcanic rocks - rhyolite to dacite, KJ: Cretaceous and Jurassic rocks - argillite, shale nad greywacke, Kif: Cretaceous felsic intrusive rocks - granite to granodiorite, KJ2: Lower Cretaceous and upper jurassic rocks - shallow and deep water clastic deposits, Ku: Cretaceous ultramafic rocks, Jif: Jurassic felsic intrusive rocks - granite to granodiorite, JTrii: Jurassic and(or) Triassic intermediate intrusive rocks - syenite to diorite, TrP: Triassic and Permian rocks - sandstone, siltstone, and shale, Pip: Permian and Pennsylvanian rocks - basaltic to andesitic lavas and derivative volcaniclastic rocks, Mzi: Mesozoic undifferentiated intrusive rocks, Mzif: Mesozoic felsic intrusive rocks - granite to granodiorite, MzPzi: Mesozoic and paleozoic undifferentiated intrusive rocks, Mzm: Mesozoic metamorphic rocks, D: Devonian undifferentiated volcanic rocks, lPzpC: Lower Paleozoic and(or) Precambrian rocks - sandstone, limestone, shale, chert and phyllite, lPzpCi: Lower Paleozoic and(or) Precambrian undifferentiated intrusive rocks, lPz: Lower Paleozoic rocks - includes rocks of Cambrian through Devonian age, in places metamorphosed to greenschist and amphibolite facies.

3.3 Materials and Methods

We mapped the locations and areas of individual landslides from pre- and post-earthquake multi-spectral satellite images and a Light Detection and Ranging (LIDAR) digital surface model (DSM) covering a total area of ~22,000 km^2. We mapped pre-earthquake landslides from ASTER and Landsat TM5 and ETM+ satellite images taken between 1995 and 2003. Post-earthquake images included Earth Observing One (EO-1) data together with LIDAR DSM (0.5-m)

covering the main affected region. The images had a fractional cloud and shadow cover of <1.2%.

We used true-color composites and panchromatic images for monoscopic image interpretation. To identify individual slope failures in the images, we used diagnostic features such as differences in shape, size, color, tone, texture, and landform assemblages (van Zuidam 1985; van Westen et al., 2008; Fiorucci et al., 2011; Gorum et al., 2011). We also used oblique-aerial photos taken from observation aircrafts shortly after the event (11/7/2002; USGS, 2002; http://ak.water.usgs.gov/glaciology /m7.9_quake/). We mapped 1,580 coseismic landslides but suspect that many small landslides remained below the detection limit of the satellite images, especially in the western part of the study area. We computed the point density [km^{-2}] and the fraction of area affected by landslides within a moving window of 2-km radius using a Gaussian kernel density estimator. We further computed hillslope gradient from an ASTER digital elevation model (GDEM-2) at 30-m pixel resolution using a best-fit plane in a 3×3 moving window. Local topographic relief was computed as the maximum elevation range within a 2-km radius.

In order to assess the role of topography and surface-rupture process on the distribution of coseismic landslides, we combined various terrain metrics with lithologic data, the mode and the rate of coseismic deformation. We used the 1:250,000 digital geologic map of interior Alaska (Wilson et al., 1998), and derived density estimates of local relief and topographic slope gradient for affected and non-affected landscapes by landslides for the thrust and strike-slip components of the fault rupture. The mean and the skewness of these distributions can be used as proxies for to characterized the spatial-response of landscape at the regional scale (Wolinsky and Pratson, 2005; Korup 2008; Korup and Schlunegger 2009), and allow assessing the susceptibility of topography to coseismic landsliding, although we excluded areas of low coseismic landslide density (<0.01%) from our analysis. Regional-scale coseismic deformation rate and rupture process of the earthquake are part of a detailed 3D rupture model based on a joint inversion of geodetic and field based off-sets measurement data (Hreinsdottir et al., 2006). We also used inversion model results from the teleseismic body-wave data (Frankel, 2004) to determine the role of low and high seismic energy pulses on the size and abundance of the coseismic landslides. Finally, we used the polygon based coseismic landslides inventories of 2007 M_w 6.2 Aisén Fjord, Chile (this study) and 2010 M_w 6.9 Yushu, Cihana (Xu et al., 2012) earthquakes to compare with Denali Fault

earthquake for identifying the similar spatial and size distribution signatures in strike-slip faulting earthquakes.

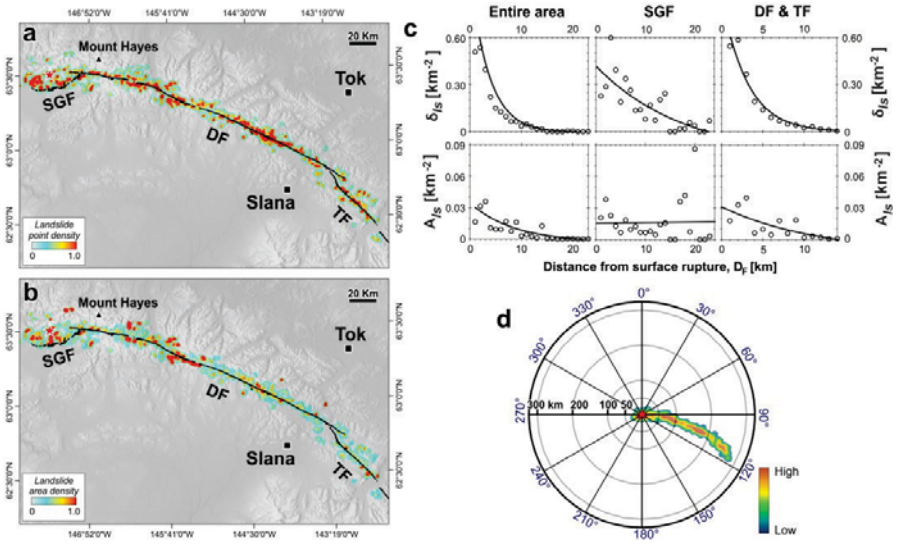

Figure 3.3 Regional density of coseismic landslides. **(a)** Normalized spatial density of coseismic landslides within 2-km radius (see text). **(b)** Normalized spatial density of area affected by the coseismic landslides within 2-km radius. **(c)** Relationship between landslide density (number, δ_{ls} and area, A_{ls}) and distance from surface ruptures, D_F. **(d)** Directivity analysis of 1,580 landslides triggered by the 2002 Denali Fault M_w 7.9 earthquake, Alaska. SGF: Susitna Glacier Fault, DF: Denali Fault, TF: Totschunda Fault.

3.4 Results

3.4.1 Regional distribution of coseismic landslides

The 2002 Denali earthquake triggered >1,580 landslides over an area of 7,150 km^2, up to ~380 km away from the epicenter. The majority of coseismic landslides clustered in a ~10-km wide corridor along the surface ruptures of the Susitna Glacier, Denali and Totschunda faults (Figures 3.3a and b). Most slope failures were shallow rock falls and rock slides from steep slopes, involving the top few meters of weathered bedrock or thin colluvium (Jibson et al., 2006). Larger bedrock failures occurred mainly in ice-covered terrain and in Cretaceous granites (Figure 3.2). Small, shallow landslides mostly clustered in the western section of the surface rupture where Devonian phyllites, graywackes, and sandstones are widely exposed. About 65% of coseismic landslides occurred in the northern part of the surface ruptures (Figures 3a, b).

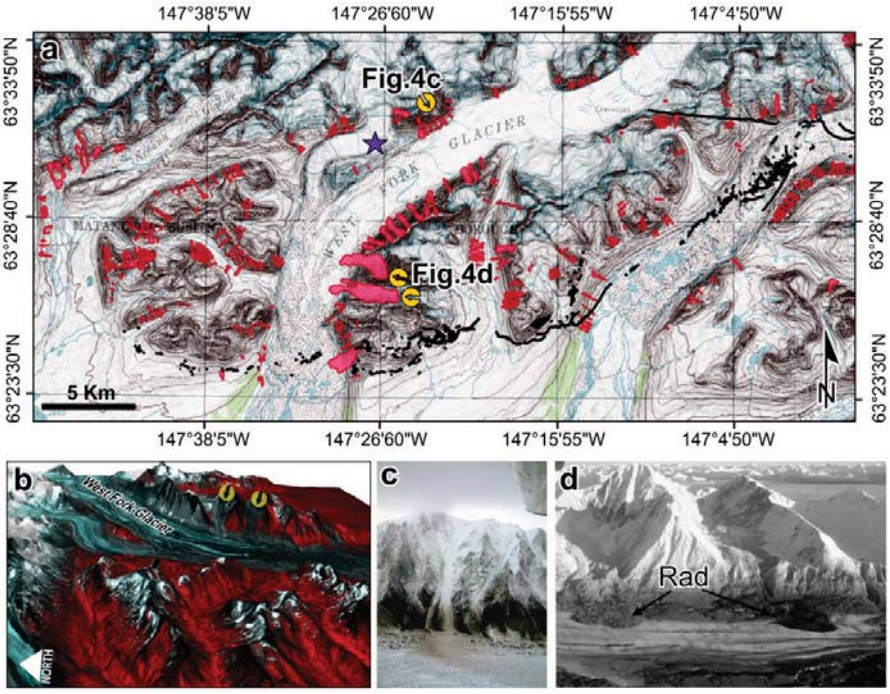

Figure 3.4 (a) Distribution of coseismic landslides in the Susitna Glacier Fault area. Star shows the location of the Denali Fault earthquake epicentre. **(b)** Post-earthquake three-dimensional scene and location of the two large rock avalanches occurred above the West Fork Glacier. **(c)** Rock avalanches and falls on the western slopes of the West Fork Glacier (photo courtesy of USGS, 2002). **(d)** West Fork Glacier rock avalanches (view toward east) (photo courtesy of USGS, 2002). Rad: Rock avalanche deposits.

Although landslide point density is generally uniform along the surface rupture and exponentially decreased away from the rupture, the areas affected by the landslides are concentrated in specific zones in three areas (Figure 3.3b). The first peak is located in near the epicentral area on the 48° north dipping plane of the Susitna Glacier Thrust Fault, and features 32% of the total coseismic landslides with a total area of 22 x 10^6 m^2. Almost all of the landslides (i.e. 94%) are located on hanging wall of the surface rupture (Figure 3.4a), and landslide point density decreases exponentially away from the surface rupture (Figure 3.3c). This decay trend is especially apparent in strike-slip sections of the surface rupture, but not so clear in the thrust section (Figure 3.3c). The landslides in this zone have an average slope gradient of >0.6 (~32°), concentrating in the steep side slopes of the West Fork Glacier (Figures 3.4a and b), where the dominant landslide types are rock slides and avalanches (Figure 3.4c).

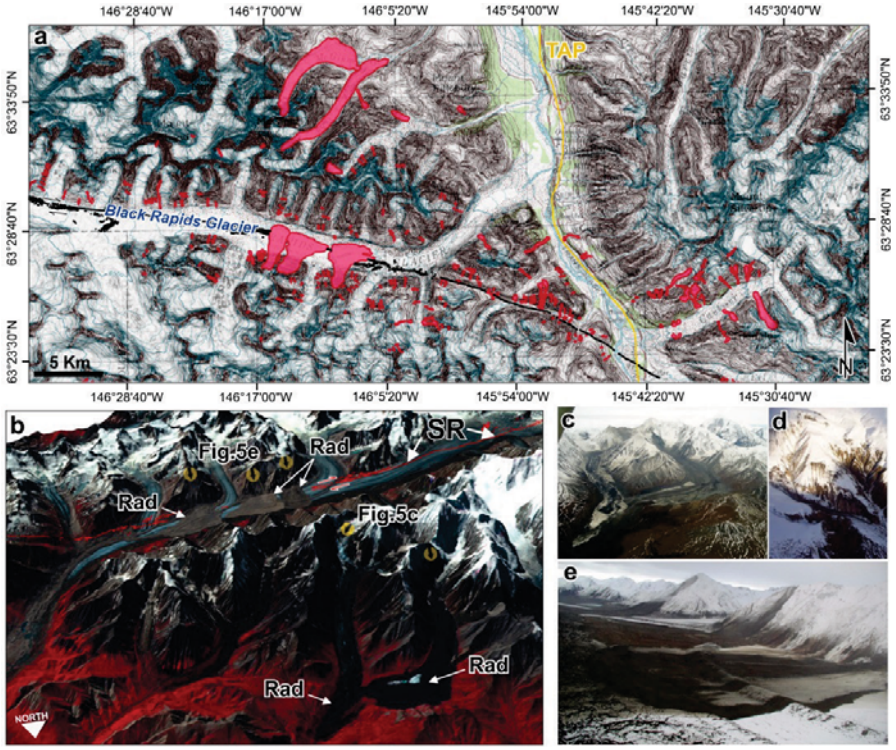

Figure 3.5 (a) Coseismic landslides in the Black Rapids Glacier. **(b)** Post-earthquake scene and location of the five large rock avalanches occurred northern and southern side of the Denali Fault. Rad: Rock avalanche deposits, SR: Surface rupture. **(c)** Rock avalanches on the north and south flanks of McGinnis Peak (view toward southwest). This two rock avalanches travelled more than 6 km. **(d)** Relatively small rock falls on slopes near the Denali fault. **(e)** Deposit of east Black Rapids rock avalanche (view toward southeast). Photos (Figure 3.5c-e) courtesy of USGS, 2002.

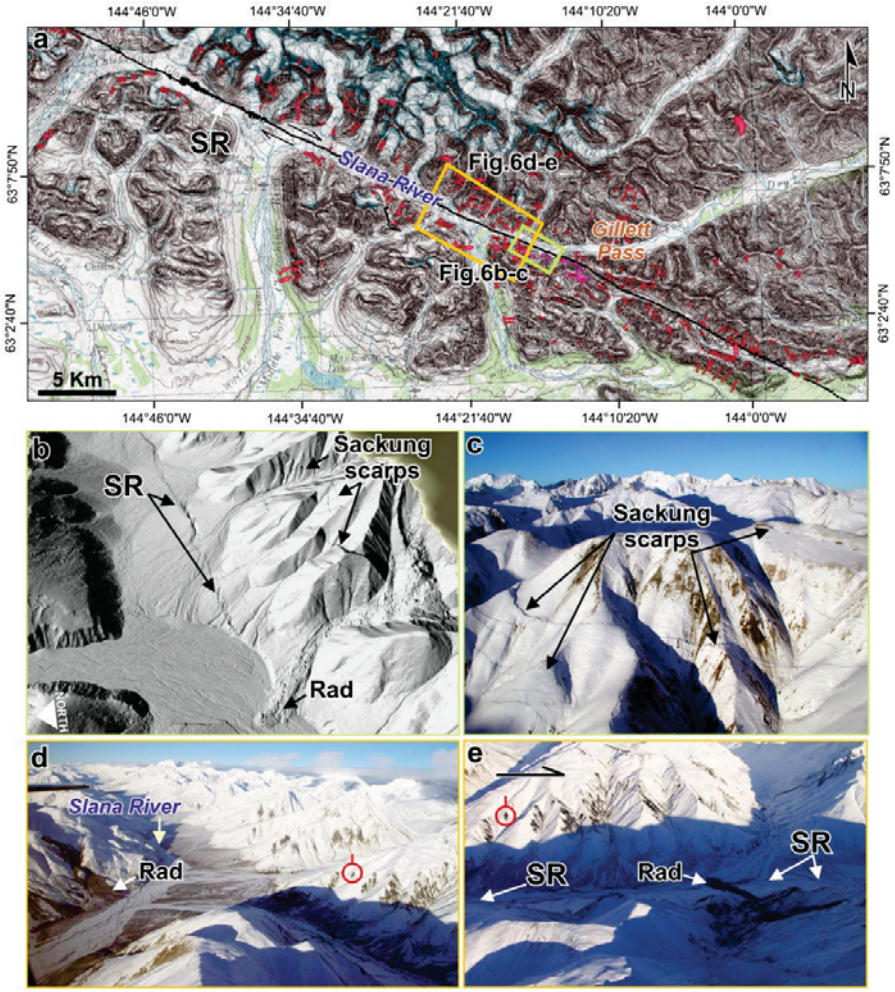

Figure 3.6 (a) Coseismic landslides in the side slopes of Slana River and southern part of the Gillett Pass. **(b)** LIDAR derived topography shows rock avalanche deposits and multiple uphill-facing scarps on ridge astride the Denali fault. Sackung scarps had 0.5-7.0 m of vertical offset; cumulative vertical offset across the ridge averaged about 9 m. Source of LIDAR data: EarthScope LiDAR data, this data set is freely available from the Open Topography portal at http://opentopography.org. Rad: Rock avalanche deposit, SR: Surface rupture. **(c)** Aerial view of the sackung cracks (views toward south). **(d)** Rock falls in the northern section of the Denali Fault (view toward northwest). **(e)** Different looking direction to the rock falls in the northern section of the Denali Fault (view toward north). In this section the majority of coseismic landslides clustered in the northern portion of the surface rupture and concentrated in the east-southeast slope face of the hillslopes which is consistent with the direction of rupture propagation. Red circles in the Figures 3.6d and e indicate the reference rock fall in both images. Black arrow in Figure 3.6e shows the propagation direction of the surface rupture. Photos (Figure 3.6c-e) courtesy of USGS, 2002.

The remarkable coseismic landslides in this zone are the West Fork rock avalanches with runouts of 3.5 and 4.1 km, and volumes of 4.1 x 106 and 4.4 x 106 m3, respectively (Jibson et al., 2004; 2006) (Figure 3.4d).

The landslide density decreases towards the west of the junction of the Susitna Glacier Thrust and Denali strike-slip faults, while spiking dramatically again ~30 km in the eastern and western parts of the right-lateral rupture on the Denali Fault near the Trans-Alaska Pipeline (TAP; Figure 3.3b). This zone corresponds to second peak in respect to coseismic landsliding, and contains 42% of the area affected by the landslides.

The largest coseismic slope failures included five huge rock avalanches near McGinnis Peak and Black Rapids Glacier (Figures 3.5a, b), with volumes of 20 x 10^6 m^3 (north), and 11 x 10^6 m^3 (south), and runouts of 11 – 11.5 km (Jibson et al., 2006; Figures 3.5b, c). Similarly large rock avalanches, with a total volume of 37 x 10^6 m^3, occurred south of the surface rupture in the north-facing hillslopes of Black Rapids Glacier (Figure 3.5). While landslide density values decrease in the western direction along the surface rupture, the values increase again 40 km west of the Denali-Totschunda Faults junction, where the surface rupture is very linear (Figure 3.6a). This increase corresponds to third peak and is not as high as the other two peak areas, but the landslide abundance in this zone is still above the average of the whole study area (Figures 3.5a, b). Shallow rock slides and falls abound south of the surface rupture, and there are sackungs having scarps and cracks with varying lengths (i.e. 10 – 650 m) from Gillett Pass about 5 km westward (Figures 3.6a, b and c). These scarps are parallel to ridge crests, and in several locations they extended through ridges normal to the ridge crest. Some scarps had as much as 7 m of displacement, and ridge-top trough and tensional anti-slope scarp formed along the surface rupture near the ridge crest (Figures 3.6b and c). In this zone, the northern block contains more landslides, with >65% concentrated on east-southeast exposed hillslope faces (Figures 3.6d, e). This aspect is consistent with the direction of rupture propagation, and indicates that the dominant east-southeast direction of coseismic slip could have caused increasing ground-motion amplitudes east-southeastward.

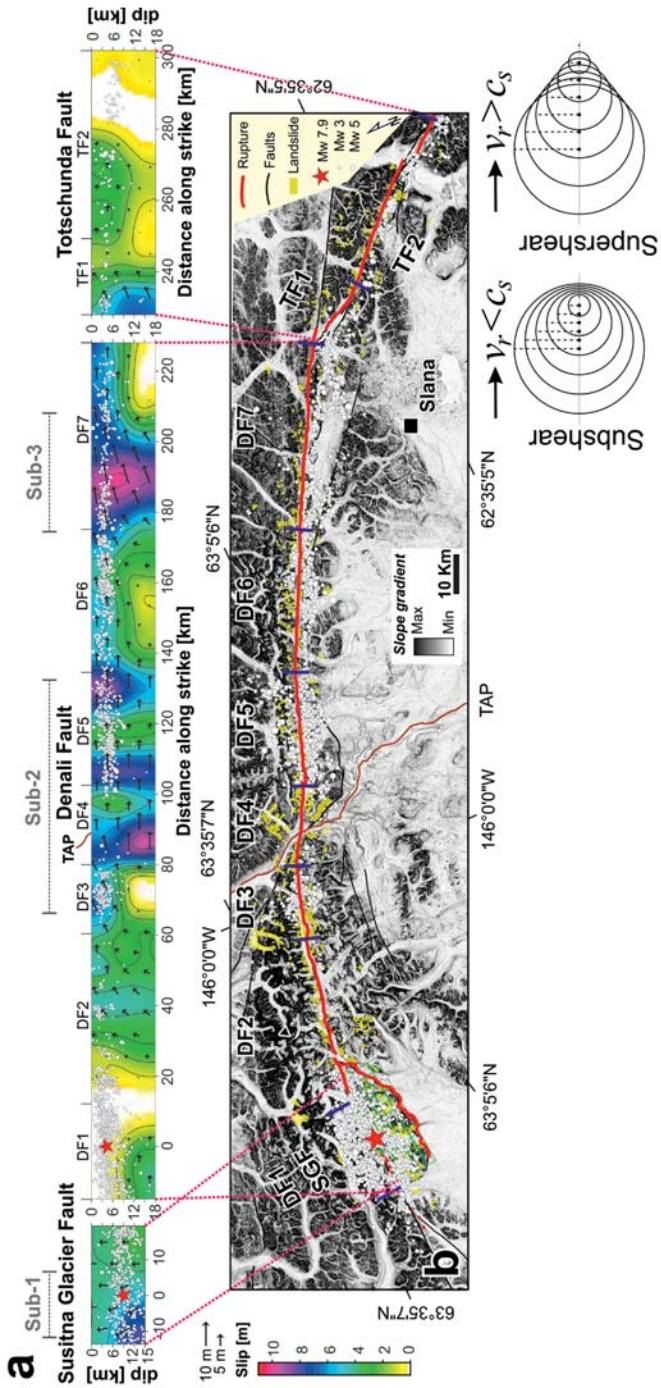

Figure 3.7 Coseismic slip model (Hreinsdottir et al., 2006) and distribution of the landslides triggered by the Denali Fault earthquake. **(a)** Coseismic slip model of the Denali Fault earthquake (Hreinsdottir et al., 2006). The estimated coseismic slip distribution is shown for (middle) the Denali Fault in seven planes (DF1-7), (right) the Totschunda Fault in two planes (TF1-2), and (left) Susitna Glacier Fault in two planes (SGF1-2), with vectors indicating slip direction and scale of the north side relative to an observer on the south side (Hreinsdottir et al., 2006). The epicenter of the earthquake is indicated with stars. TAP: Trans-Alaska pipeline. Faults are from Plafker et al. (1994). **(b)** Distribution of coseismic landslides for spatial and visual comparison with coseismic slip model and the location of the subevents. The relocated aftershocks (white dots) from Ratchkovski et al. (2004) in both figures are shown for reference. Inset illustrations (from Dunham and Bahat, 2008) show shear wavefronts emitted when the rupture passes the solid dots. Rupture speed, v_r is lower than S-wave speed, c_s, in case of subshear rupture (left) which is reversal for super-shear rupture (right).

3.4.2 Coseismic displacement, fault rupture geometry and rupture velocities

The complex rupture of the event generated mainly three deformational areas which correspond to individual subevents (Frankel 2004; Hreinsdottir et al., 2006) that show as areas of above-average coseismic slip rate (Figure 3.7a). The location and the range of these subevents (Figure 3.7a) defined by inversion of teleseismic waveforms (Frankel 2004) and GPS data with surface offset measurements (Hreinsdottir et al., 2006). Vertical displacement ranges from 0.2 to 5.4 m (Crone et al., 2004) in the first subevent, which occurred near the epicentral area on the Susitna Glacier Thrust Fault, with most landslides clustering in areas with 1.5 to 5 m offsets (Figures 3.7a, b). Bordering the unruptured segment of Denali Fault during the earthquake, 94% of coseismic landslides occurred in the hanging wall, up to 24 km away from the fault. In the western strike-slip segments, where two subevents occurred, coseismic landslides occurred in a 10-km corridor along the surface rupture. Although the maximum horizontal displacements during the Denali earthquake were associated with subevent 3, the area affected by the landslides in this part was considerably lower than the other two sub-events (Figures 3.7a, b). Subevent 1 and subevent 2 contain 517 coseismic landslides, with a total affected area of 80 x 10^6 m^2, which is nine times more than that in subevent 3 at 40 km prior to the Denali-Totschunda Faults junction (Figure 3.7). Moreover, the largest high-frequency energy per fault segment occurred in subevent 1 and 2, respectively (Frankel, 2003). On the other hand, when comparing the effective length along the rupture and the landslide abundance in these parts, subevent 3 has higher landslide abundance. Thus, the landslide abundance varies with deformation rate. This low ratio of total area affected by landslides in subevent 3 can be explained by the relatively lower accelerations and less high-frequency seismic energy caused by the super-shear rupture dynamics.

Dividing the surface rupture into two sub-sections based on dominant fault-slip geometries and normalizing the data with respect to rupture length of the each fault types, we find that the western portion of the fault (SGF), which is dominated by thrust faulting and high vertical coseismic offsets (with an average of ~3 m), has the highest values (normalized) of area affected by landslides overall. Local decreases in landslide density are consistent with lower measured coseismic offsets (Figures 3.7a, b).

Table 3.1 Areal distributions of lithological units in the study area with respect to landslides triggered by the Denali Fault earthquake.

Lithology	Symbol	Landslide				Lithology		Landslide density
		Frequency of landslides (*N*)	Frequency of landslides (%)	Total area *A* (km^2)	%	Total area *A* (km^2)	%	%
Glacial covered areas	Glacier	300	18.99	58.51	48.23	2332.59	33.23	1.76
Ultramafic rocks (Tertiary)	Tu	2	0.13	0.05	0.04	16.98	0.24	0.19
Undifferentiated intrusive rocks (Tertiary)	Ti	5	0.32	0.92	0.76	41.53	0.59	1.55
Granite to granodiorite (Tertiary)	Tif	58	3.67	7.07	5.83	91.67	1.31	5.41
Argillite, shale, greywacke, quartzite, conglomerate (Cretaceous)	KJ	209	13.23	11.45	9.44	498.56	7.10	1.61
Granite to granodiorite (Cretaceous)	Kif	148	9.37	7.44	6.13	441.88	6.30	1.18
Ultramafic rocks (Cretaceous)	Ku	6	0.38	0.29	0.24	23.15	0.33	0.87
Sandstone, arkose, siltstone, and limestone (Lower Cretaceous)	KJ2	212	13.42	6.96	5.74	1018.77	14.52	0.48
Argillite, limestone, siltstone, conglomerate, and abundant gabbroic sills (Triassic)	TrP	25	1.58	0.69	0.57	304.92	4.34	0.16
Basalt (Triassic)	Trvm	53	3.35	1.23	1.01	320.59	4.57	0.27
Basaltic to andesitic lavas (Permian)	PIP	65	4.11	5.88	4.85	371.06	5.29	1.11
Undifferentiated intrusive rocks (Mesozoic and Paleozoic)	MzPzi	12	0.76	1.19	0.98	75.45	1.07	1.11
Pyroclastic rocks and ash flows interbedded with sedimentary rocks (Devonian)	D	268	16.96	6.63	5.46	749.59	10.68	0.62
Schist and gneiss (Paleozoic and (or) Precambrian)	PzpCm	129	8.16	8.66	7.14	447.84	6.38	1.36
Limestone, dolomite, argillite, chert, and graywacke (Lower Paleozoic)	lPz	88	5.57	4.35	3.58	283.99	4.05	1.07

Directivity analysis of 1,580 landslides reveals a distinct sub-parallel clustering with respect to the ruptured faults, with less landslides occurring west of the epicentral area (Figure 3.3d). The majority of slope failures occurred both within <118° of the mean azimuth of the surface rupture, and the western fault segments dominated by dip-slip (Figure 3.3d). Coseismic landslide concentration from west to east direction along the surface rupture is consistent with the direction of rupture propagation.

3.4.3 Rock-type, local relief and hillslope steepness effects

Landslide abundance per unit area varies per lithologies along the surface rupture (Table 3.1). Where slope failures abound, Cretaceous sandstone and limestone, Devonian pyroclastic rocks, and glacierized areas contain 50% of all landslides among the bedrock and Quaternary cover units. In terms of landslide densities (Table 3.1), glacierized Tertiary granites are the most landslide-prone units. The widespread Cretaceous sandstone, arkose, and limestone rocks show surprisingly few landslides, while Triassic to Tertiary sedimentary and ultramafic rocks were amongst the most resilient lithologies in the earthquake-struck region.

Local relief and hillslope gradient have a nonlinear relationship with landslide density (Figures 3.8a and b). Landslide density increases in a roughly linear fashion with both local relief and hillslope gradient from H ~250 to 650 m and S_h ~0.2 to 0.8, respectively, but then increases rapidly near the common modes of the local relief and hillslope gradient (H ~700-800 m and S_h ~0.9-1.0). This supports earlier observations from several other earthquake-struck landscapes (Keefer, 2000; Korup, 2008; Iwahashi et al., 2007; 2012). Local relief and slope gradient values decrease from west to east in the high density landsliding zone. This decreasing form is explicitly high in the eastern part of TAP.

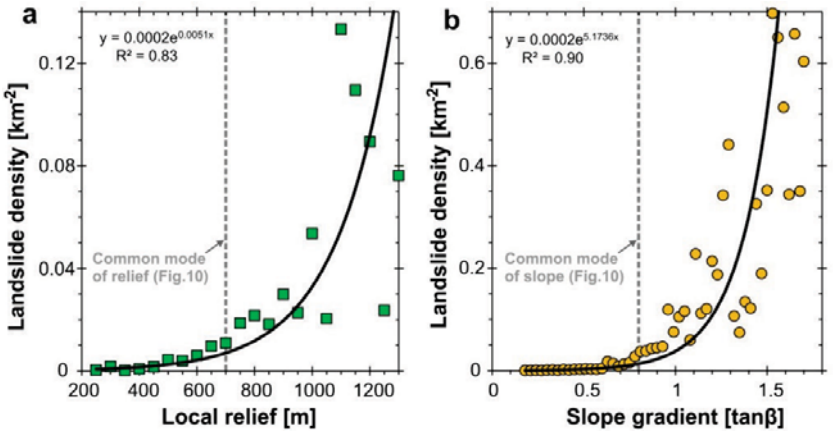

Figure 3.8 Landslide density versus local relief **(a)** and slope gradient **(b)**. The linear increase in landslide density grows significantly above the common mode of local relief and slope gradient.

The geomorphometric parameters of coseismic landslides (Table 3.2) in ice-covered and ice-free areas vary in terms of their topographic characteristics (Figures 3.9a-d). Only 300 landslides, but 48% of the total landslide-affected area is in glacierized terrain (Table 3.2). There, landslides descended from steeper and higher slopes, and had longer runouts. Apart from the ten large rock avalanches triggered by the earthquake, the average deposit thickness of the coseismic landslides was <1 m (Jibson et al., 2006). The presence of longer landslides in the ice covered terrains, despite the generally similar thickness values in earthquake struck area, can possibly be attributed to the low-friction surfaces such as on glaciers.

Table 3.2 Comparison of geomorphometric variables of ice covered and ice free terrains in Denali Fault earthquake struck region.

Geomorphometric parameter	Min	Max	Mean	Std. error	Std. deviation	Median	Skewness	Kurtosis
Ice covered terrains (N =300)								
Altitude (m)	932.8	3064.5	1830.5	21.8	376.9	1822.2	0.5	0.6
Local relief (m)	223.0	1736.0	767.8	11.3	195.3	756.0	0.7	2.1
Slope gradient (tanβ)	0.2	2.0	1.0	0.0	0.3	0.9	0.5	0.3
Terrain ruggedness	0.0	0.3	0.1	0.0	0.1	0.1	0.6	-0.5
Slope height (m)	32.0	841.9	267.7	8.7	150.7	244.3	0.9	0.5
Landslide area (m^2)	1459.5	8,984,600	167,360	43,560	754,480	26,105	8.4	80.7
Landslide runout (m)	63.2	11,508	548.3	38.6	669.4	361.9	5.5	41.3
Ice free terrains (N = 1279)								
Altitude (m)	794.6	2,811	1,525	8.7	312.8	1,512	0.4	0.7
Local relief (m)	230.0	1,659	695.6	4.4	159.1	685.0	0.4	1.5
Slope gradient (tanβ)	0.2	1.7	0.9	0.0	0.3	0.8	1.9	10.8
Terrain ruggedness	0.007	0.31	0.08	0.001	0.05	0.08	0.72	0.40
Slope height (m)	13.5	758	234.1	3.7	132.4	214.1	0.8	0.4
Landslide area (m^2)	889.9	6,920,700	55,547	6,902	246,830	21,793	20.13	502.95
Landslide runout (m)	55.5	3,539	430.5	12.5	450.0	310.5	10.1	192.8

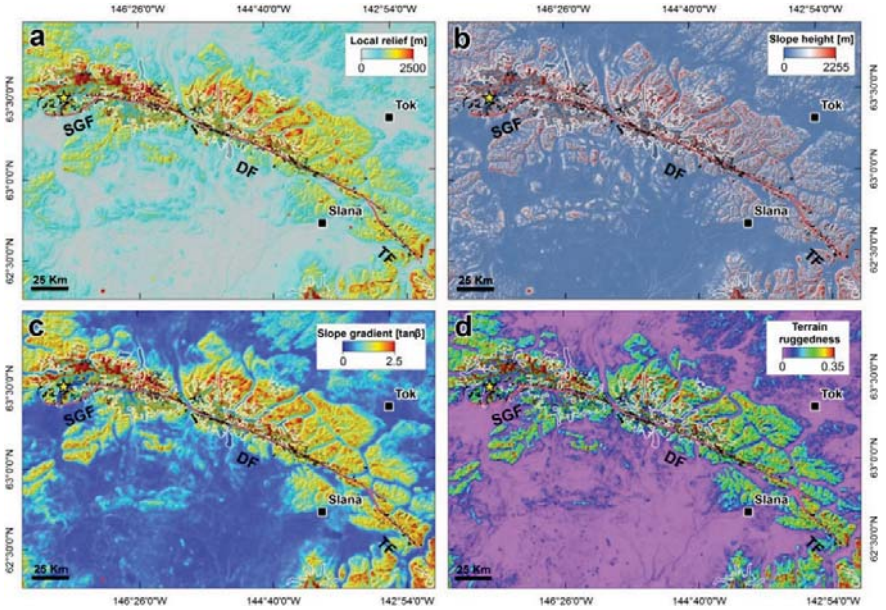

Figure 3.9 Geomorphometric variables of the earthquake struck region. **(a)** Local relief. **(b)** Slope gradient. **(c)** Slope height. **(d)** Topographic ruggedness. White lines highlight the boundary of the ice covered areas.

3.4.4 Control of topography and surface rupture on coseismic landslides

Coseismic landslides occurred mostly on hillslopes steeper than the modal slope gradient for the study area (Figures 3.10a, b). This phenomenon was also similar in DTF and SGF, despite their different faulting mechanisms. However, coseismic landslides located on SGF had slightly lower values of local relief and slope gradient modal than DTF (Figure 3.10a, b), while landslide density varies with the different faulting types (Figures 3.10c and d).

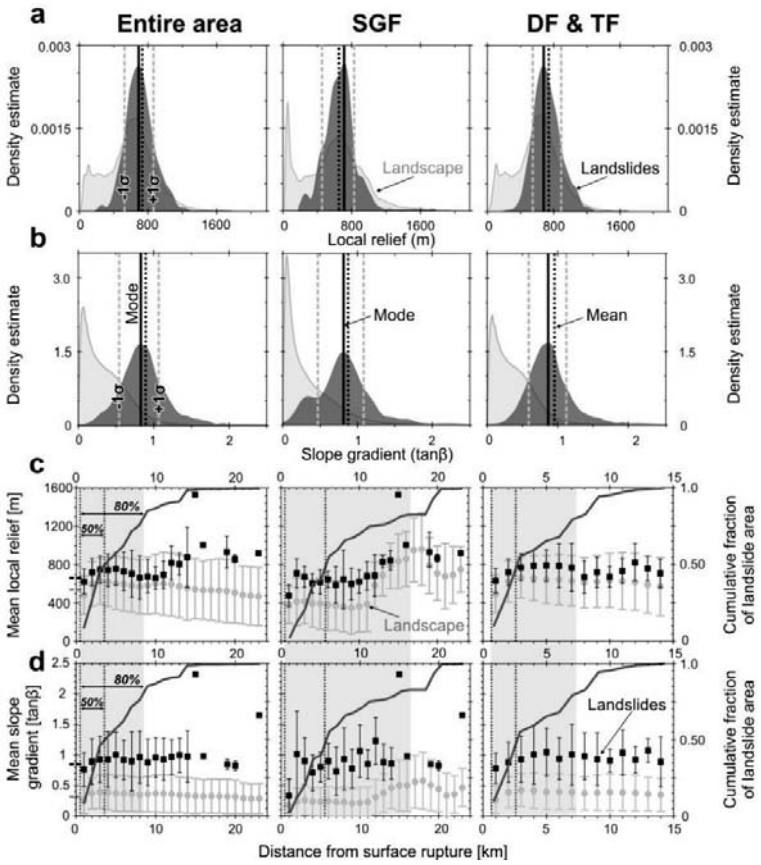

Figure 3.10 Gaussian kernel density estimates of local relief **(a)** and hillslope gradient **(b)** in the entire and the different style of faulting sections of the study area. Mean local relief **(c)** and hillslope gradient **(d)** of landslides and landscape as a function of 1-km distance bins from surface rupture in the entire and the different style of faulting sections of the study area. Right axis shows cumulative fraction of landslide area. Light grey boxes and dashed black lines delimit 80% and 50% of cumulative fraction of landslide area, respectively.

About 80% of the landslide-affected area is in the first 8 km distance band of the surface rupture in steeper portions of the landscape. Hence only small areas were affected by the landslides in the first kilometers of the distance band. Such a distribution can mainly be explained by the fact that surface rupture was developed along the glacial valley where local relief and slope gradient values were low. In contrast to SGF where thrust faulting is dominant, landslides concentrates in a narrower zone in DTF with 80% of landslides located in a 7-km long segment. In SGF, coseismic landslides are observed up to 24 km distance, with 80% of the landslides distributed in a 16 km part of the surface rupture. Here, mean local relief values of the areas affected by the coseismic

landslides exceeds the landscape mean by ~1.4 times. The higher variation between coseismic landslides and mean slope gradient values of the landscape is similar both in thrust and strike-slip dominant SGF and DTF, respectively (Figures 3.10c, d). Mean local relief and slope gradient of the coseismic landslides increases with distance from the surface rupture in parts where both faulting mechanisms prevail. Furthermore, coseismic landslide abundance decreases after 15 km despite sufficiently steep terrain. This decrease points at an exponential seismic wave attenuation. Considering the strike of surface rupture (111°), the control of both distance from the fault (roughly in N-S direction) and topographic parameters occurs along the fault. However, coseismic landslide abundance and density is peaked in individual subevents along the surface rupture.

3.5 Discussion

Our data show that fault geometry is a key control on the spatial landslide distribution in normal to the fault. Clustering of 70-85% of the landslides triggered by intermediate- and large-sized earthquakes over the surface projection (up- and down-dip edge) of earthquake fault supports this observation, e.g. 1989 Loma Prieta, U.S.A (M_w 6.9) (Keefer, 2000), 1999 Chi-chi, Taiwan (M_w 7.6) (Liao and Lee, 2000), 2008 Wenchuan, China (M_w 7.9) (Gorum et al., 2011) events. The landslides pattern reflects the segments of differing fault geometry, especially in complex earthquake rupture sequences involving more than one fault type (Gorum et al., 2013). Yet the abundance and density of the coseismic landslides strongly vary along the surface rupture.

We assume that the frictional strength along the fault plane is not uniform, thus overall displacement involves slip on one or more asperities, i.e. high-slip patches, where the friction is maximum (Hall-Wallace, 1998). Most of the energy released during earthquakes is tied to these asperities (Ruiz et al., 2011). Our results show a strong variation of coseismic landslide abundance with both rate and mode of the coseismic deformation, but also with the topography. Step changes in cumulative area and in the number of the coseismic landslides coincide where coseismic deformation attained its maximum (Figures 3.11a, b). These areas of higher coseismic slip correspond to earthquake asperities and contain nearly 85% of the areas affected by the landslides (Figures 3.7a; 3.11a, b).

Although the highest displacement values were measured in subevent 3, the areal landslide density was lower in subevent 3 compared to the first two

subevents (Figure 3.11a, Sub-3). However, there is still a considerable increase in terms of cumulative number of landslides in subevent 3. These differences are likely to be caused by differing modes and rates of coseismic slip, rupture velocities, and topographic parameters observed for these subevents. Vertical slip rates in the first two subevents is higher than in subevent 3 (Figure 3.11b). Coseismic slip directions are fault-normal and therefore have compressive strain in subevent 1. On the other hand, subevent 2 shows a transition character. In subevent 2, especially where landslides abound, coseismic slip directions are fault-parallel with high shear strain and above-average vertical displacement (Figures 3.7a, 11b). In subevent 3, horizontal displacements dominate while surface rupture is quite linear. In addition, while velocity values are 3.5 km s^{-1}. or lower in subevents-1 and 2, it appears to have an effective rupture velocity of about 5.0 km s^{-1} in subevent 3, which is super-shear (Frankel, 2003). In this respect, rupture speed determines how waves from different parts of the fault interfere with each other (Figure 3.7 illustrated inset diagrams from Dunham and Bhat, 2008). When the rupture is subshear (rupture speed, v_r < S-wave speed, c_s) as in subevent 1 and 2, the wavefronts are concentrated in the forward direction and separated in the backward direction (Figure 3.7 inset diagram (left)). This leads to larger amplitudes and higher frequencies in the forward direction (Dunham and Archuleta, 2004; Dunham and Bhat, 2008). For super-shear ruptures ($v_r > c_s$), the source outruns the waves (Figure 3.7 inset diagram (right)) and a Mach front is formed (Dunham and Bhat, 2008). Thus, it is not surprising that landslide density is high in the first two subevents but how landslide pattern record these differences in rupture velocities is remarkable. Additionally, our coseismic landslide inventory provides a unique opportunity to characterize the propagation direction of the surface rupture. Distribution pattern of 1,580 landslides shows a distinct sub-parallel clustering with respect to the ruptured faults, with less landslides occurring west of the epicentral area suggests that the dominant direction of the seismic waves could have caused the increasing of the ground-motion amplitudes eastward.

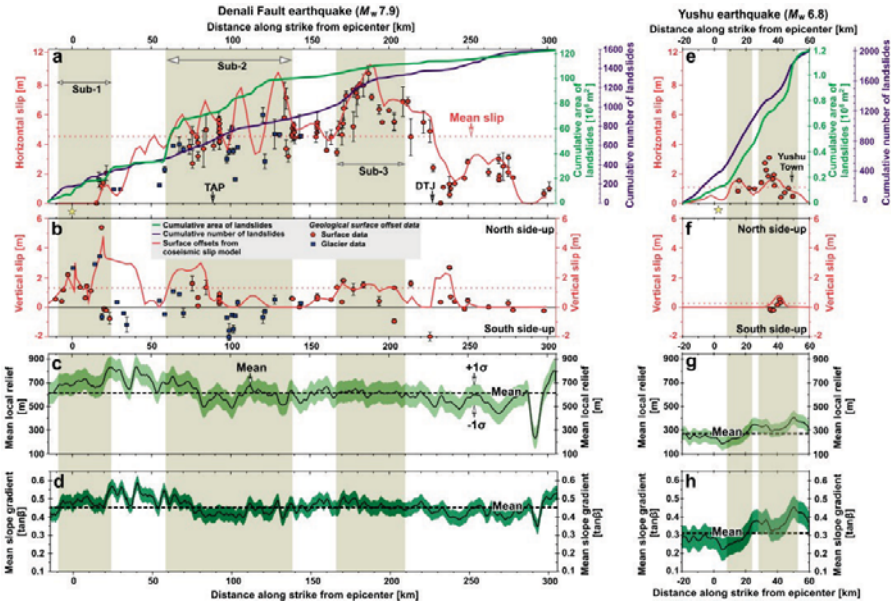

Figure 3.11 Along-strike comparison of cumulative number and area of landslides with modeled coseismic slip and topography in Denali Fault and Yushu strike-slip faulting earthquakes. **(a)** Modeled horizontal (dextral) slip amplitudes (Hreinsdottir et al., 2006) of Denali Fault earthquake and cumulative number (purple lines) and area (green lines) of coseismic landslides per 3-km bins. Geological offset data (red circles and blue squares) are from Haeussler et al. (2004). **(b)** Modeled vertical (reverse) slip amplitudes of Denali Fault earthquake (Crone et al., 2004; Hreinsdottir et al., 2006). **(c)** and **(d)** Swath profiles (40 km × 340 km) of mean local relief and mean slope gradient which are computed from GDEM-2 elevation data within a 3-km radius. Black lines and green shading are means and ± 1 st. dev. per 60-m bins. Dark grey boxes delimit subevents of the Denali Fault earthquake. TAP: Trans-Alaska pipeline. DTJ: Denali-Totschunda fault junction. **(e)** Modeled horizontal (sinistral) slip amplitudes (Li et al., 2011) of Yushu earthquake and cumulative number (purple lines) and area (green lines) of coseismic landslides per 3-km bins. Geological offset data (red circles) are from Lin et al. (2011). **(f)** Modeled vertical (reverse) slip amplitudes of Yushu earthquake (Li et al., 2011). **(g)** and **(h)** Swath profiles (20 km × 80 km) of mean local relief and mean slope gradient which are computed from GDEM-2 elevation data within a 3-km radius. Black lines and green shading are means and ± 1 st. dev. per 60-m bins. Dark grey boxes delimit high slip-patches of the Yushu earthquake.

Numerical modelling results showed that glaciers may reduce topographic amplification of seismic shaking in mountainous terrain (McColl et al., 2012), although topographic amplification of seismic shaking is most pronounced for steeper slopes, and near the crests of mountains or hills (Meunier et al., 2008, Gorum et al., 2013). Terrain oversteepened by glacial scour may amplify seismic shaking more than gentler topography (McColl et al., 2012). In our study area valley and cirque glaciers dominate, thus potentially buffering seismic impacts on toe- or mid-slopes. We find that coseismic landslides originating from narrow, sharp-edged ridges between glacial valleys and upper

slopes of glacierized sections had larger size and runout in the eastern section of the surface rupture particularly. Despite the less occurrence of coseismic landslides in ice-covered terrains (n= <300), the mean area and runout of landslides in this terrains are significantly higher than those of the ice-free terrains (Table 1).This supports the notion that glacial environments can significantly increase the landslide runout of by travelling on low-friction surfaces such as on glaciers, by melting of ice and snow as a result of frictional heating that lead to pore pressure effects at the base of the moving mass or fluidizes the entire flow body (Evans and Clague, 1988; Schneider et al., 2011).

Super-shear velocities revealed in subevent 3 were associated with a decrease in the generation of high-frequency energy at the east end of subevent 3 by Frankel (2003), which is also consistent with the theoretical work of Burridge (1979). The low local relief and hillslope steepness and the accelerations together with less high-frequency energy in subevent 3 and further towards to the east have important effects on the areal fraction of landslides (Figures 3.11c and d). In addition to these factors, limited slope height, and absence of low-friction surfaces such as on glaciers in the areas where subevent 3 recorded may further cause a significant decrease in the size of landslides.

We compared the observations and the results obtained from the analysis about the effects of topography and coseismic slip rate-mode on the landslide distribution pattern and density variations along the surface rupture in the Denali Fault earthquake with the 2010 M_w 6.8 Yushu strike-slip faulting earthquake triggered landslides (Xu et al., 2012; Figures 3.11e-h). This comparison with regard to potential controls of the coseismic slip rate-mode and the topography on coseismic landsliding response shows that there is also a similar signature in the Yushu earthquake. There, the coseismic landsliding pattern similarly mimics variations in coseismic rate and mode together with high topographic relief and hillslope steepness (Figures 3.11e-h). High landslides abundance in below-average local relief and hillslope steepness indicates that the control of slip rate was more prominent in the central section of the fault rupture (Figures 3.11g, h). Despite the similar overall signature of the Denali Fault event, the number of landslides triggered by Yushu earthquake is higher.

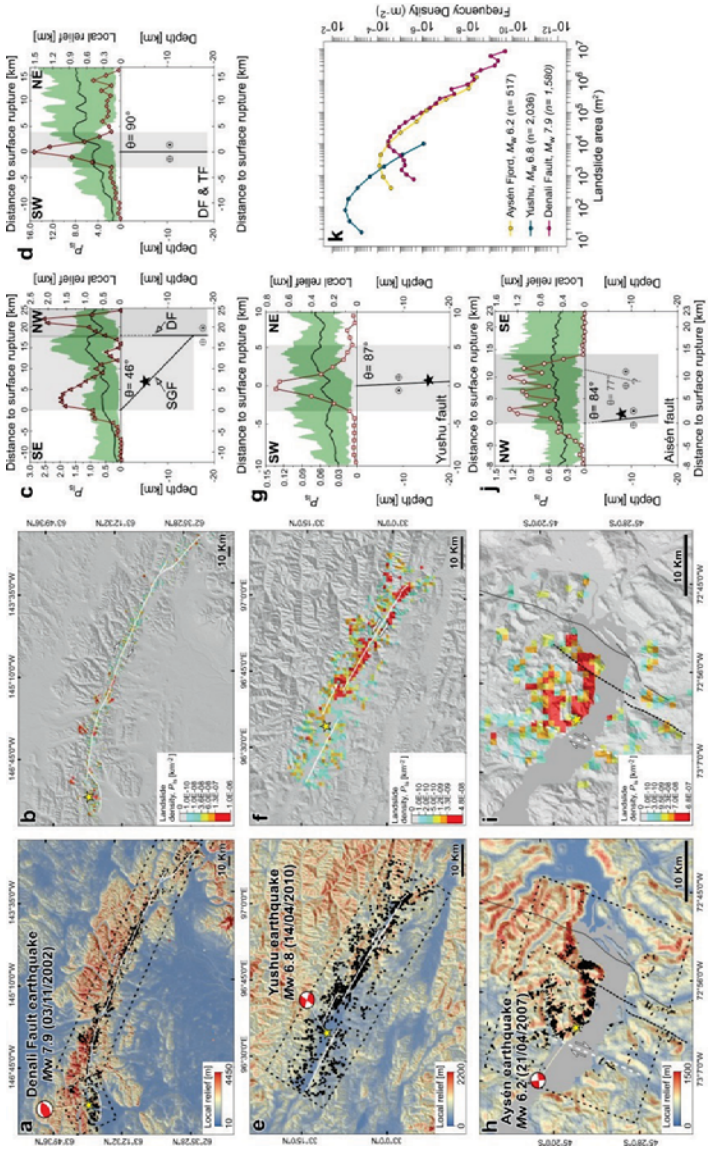

Figure 3.12 Comparison of fault geometry with landslide density (P_{ls}) and local relief along transverse swath profiles for **(a)-(d)** Denali Fault, **(e)-(g)** Yushu and **(h)-(j)** Aysén Fjord strike-slip faulting earthquakes. Dashed rectangles are locations of transverse swath profiles (Figures 3.12c, d, g and j). Thick black line and green shading in the graphs are mean, minimum, and maximum local relief, respectively, computed for 60-m bins. We calculated landslide density P_{ls} (dark red lines: $P_{ls} = A_{ls}/A_t$ where A_{ls} is the area of all landslides within a chosen window size A_t (Meunier et al., 2007). Stars show the location and the position of the earthquake epicenter and hypocenter. **(k)** Size distributions of log-binned landslide deposit areas for three strike-slip faulting earthquakes.

This is mainly caused by the spatial resolution of the remote sensing images used: the images used in the Yushu event-inventory had higher spatial resolution than the ones used in the Denali inventory, i.e. ~1m and ~10m respectively. Yet the total area affected by the landslides triggered by Yushu earthquake is about an order of magnitude below that related to the Denali

earthquake. This is not only related to the total surface rupture length and amount of coseismic slip caused by the Yushu earthquake. Moreover, the areas affected by these two earthquakes are very different in terms of geomorphic environment, which also highly affects the sizes of landslide size as much as the effects of coseismic slip amplitudes. For example, differently from Denali, the Yushu earthquake occurred in a semiarid plateau which had hilly terrains with relatively less steep hillslopes in terms of geomorphic setting. In a regional context, the availability of high slope gradient and larger slope patches may affect the slope stability response to seismic ground shaking. Comparison of polygon-based landslide inventories of strike-slip faulting earthquakes shows that together with the coseismic slip rate, the differences and variations in fault geometry (dip, strike, and slip mode) and local relief has distinctive controls on limiting the size- and spatial distribution of coseismic landslides (Figures 3.12a-j). Except for the thrust segment, SGF, in the Denali Fault, both Denali Fault and Yushu have a narrow density over a non-circular area around the surface ruptures in terms of landslide pattern (Figures 3.12a-g). Unlike the dip-slip faulting earthquakes, in strike-slip faulting earthquakes the strain generally localizes to narrow segments which are wider near the surface than at depth, representing flower structures (Finzi et al., 2009). We obtained similar results in 2007 M_w 6.2 Aysèn Fjord earthquake, in which the control of fault geometry on landslide distribution was more complex (Figures 3.12h-j). The more scattered landslide distribution in Aysèn Fjord as compared to the Denali Fault and Yushu earthquakes can be explained a rupture process involving slip on multiple gently dipping faults (Agurto et al., 2012). Although the Aysèn Fjord earthquake was shallow, it did not rupture the surface, causing a less pronounced coseismic landslide pattern. Despite the limited information about the rupture processes of the Aysèn Fjord earthquake, considering the magnitude of the earthquake, the presence of fewer but larger landslides likely results from the high local relief and hillslope steepness. Additionally, the observation of higher number of landslides in the segments where strike-slip type of faulting formed step-over and bend structures along surface rupture (Figures 3.7, 3.12) favors the idea that local geometric variations over the surface rupture increase the coseismic landsliding.

Overall, our observations on coseismic landslide clustering and size-frequency distributions from comparison of strike-slip faulting earthquakes challenge the validity of empirical relationships between landslide frequency and earthquake magnitude (e.g. Malamud et al., 2004), and area affected by landslides and earthquake magnitude (e.g. Keefer 1984; Rodríguez et al., 1999) which have

unexplained variance of up to about an order of magnitude in our study (Figure 3.12k).

3.6 Conclusions

In summary, we highlight the spatial collocation of abundance, distribution pattern and the size of the coseismic landslides with fault geometry and coseismic slip amplitudes in earthquakes with strike-slip motion. Our study of the 2002 Denali Fault (M_w 7.9) earthquake shows that the differences and variations in fault geometry (dip, strike, and slip mode), together with regional contrasts in geomorphology are important factors controlling the distribution pattern of coseismic landslides, which is a narrow distribution in surface ruptured steep strike-slip faulting earthquakes. The November 3, 2002 Denali Fault earthquake (M_w 7.9) triggered nearly 1,580 landslides with a regional pattern where 80% of slope failures were located in a narrow zone about 15 km wide that straddled the surface rupture over its entire 300 km length. Distinct clusters occurred in areas of high coseismic slip, local relief and slope steepness in where the limits of landslide distribution set by the fault geometry. This pattern corroborates the notion that landslide-density changes mimic variations in coseismic deformation together with high topographic relief along the surface rupture. Furthermore, we show that the differences in rupture velocities between the rupture subevents may further elevate the fraction of the area affected by slope failures. Despite the high coseismic slip rate in the subevent-3, the low coseismic landslide density in this section is mainly due to less high-frequency energy radiation and the limitation of slope failure to areas of varying topographic roughness and hillslope steepness. In addition, we surmise that glaciers, which cover the areas up to 150 km eastward of the epicenter and mainly mantled the mid-slopes, may reduce the topographic amplification though significantly increase the run-out size of the landslides.

Comparing Denali Fault earthquake with other strike-slip faulting events strengthen the view that the distribution pattern, abundance, and area affected by coseismic landslides are linked to first-order with the fault geometry and type, the changes in geomorphic and topographic characteristics, and rate and mode of the coseismic displacements along the surface ruptures. Moreover, frequency-size distributions show that future work may want to consider the seismic properties (i.e. magnitude, faulting mechanism and rupture dynamics) and physiographic characteristics together rather focusing on earthquake magnitude alone.

4 Complex rupture mechanism and topographic controls on landslides-induced by 2010 Haiti earthquake: Implications for coseismic landslide patterns of surface and blind rupture earthquakes[1]

4.1 Introduction

The M_w 7.0 Haiti earthquake struck the southern part of Hispaniola Island at 16:53 local time (21:53 UTC) on 12 January 2010. It was the deadliest earthquake in South Hispaniola's recent history, with more than 316,000 fatalities; 300,000 people injured; 35,000 buildings destroyed; and 1.5 million people left homeless (Cavallo et al., 2010). The earthquake hypocenter was at 18.44° N, 72.57° W, at a depth of 13 km in a poorly seismic instrumented region. The U.S. Geological Survey (USGS) National Earthquake Information Center (NEIC) and the global centroid moment tensor solutions, associated the initial location and mechanism for this event with the rupture of the sinistral Enriquillo-Plantain Garden Fault (EPGF) zone, a major fault system accommodating 7±2 mm yr^{-1} of relative motion between the Caribbean plate and Gonâve microplate (Mann et al., 1984; Manaker et al., 2008; Hayes et al., 2010; Figure 4.1).

The region most affected by the earthquake is located on the junction of the EPGF zone and the Transhaitian Belt (THB), which are the two major crustal structures in eastern Hispaniola (Figure 4.1a and b). From historical records the EPGF was known to have caused M >7 earthquakes in the 18th century (Mann et al., 1995; Calais et al., 2010; Bakun et al., 2012). The 2010 earthquake, however, did not create any detectable surface rupture (Prentice et al., 2010; Mercier de Lépinay et al., 2011), raising the question of which fault was ultimately responsible. Studies that integrated the aftershock moment tensor solutions (Mercier de Lépinay et al., 2011), space geodetic measurements (Hayes et al., 2010; Hashimoto et al., 2011), and field-based uplift data revealed a complex rupture process involving slip on multiple faults (Hayes et al., 2010),

[1] This chapter is based on the following paper: Gorum, T., van Westen, C.J., Korup, O., van der Meijde, M., Fan, X., van der Meer, F.D., 2013. Complex rupture mechanism and topography control symmetry of mass-wasting pattern, 2010 Haiti earthquake. *Geomorphology 184: 127-138*.

with surface deformation driven by rupture on the N264°E north-dipping Léogâne blind thrust fault, and only minor deep sinistral slip along the EPGF.

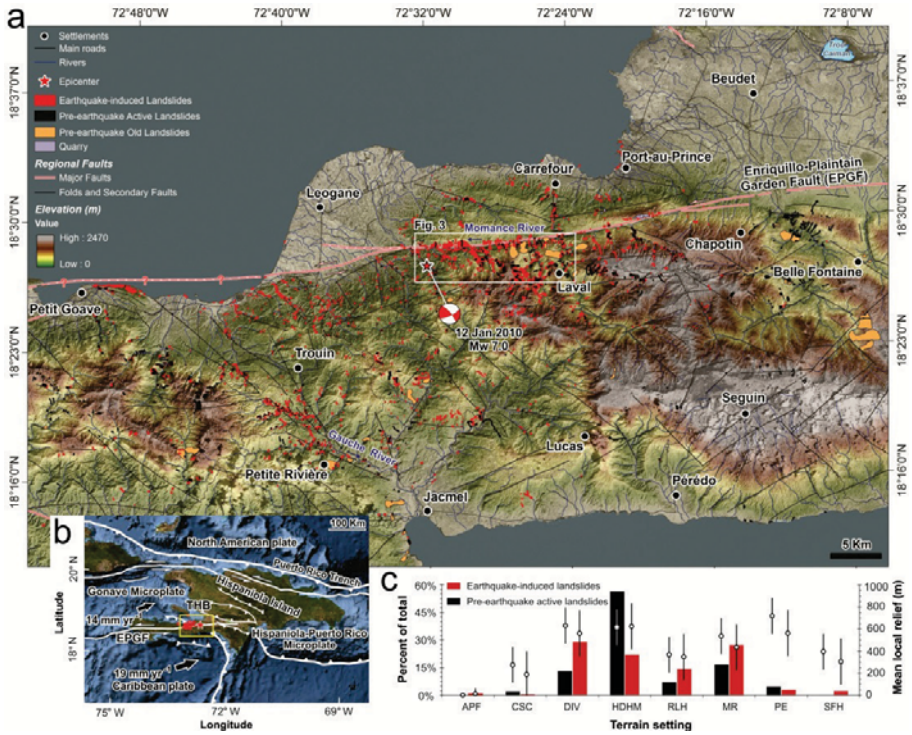

Figure 4.1 Tectonic setting and landslide distribution map of the study area. **(a)** Area surrounding the M_w 7.0 January 2010 Haiti earthquake epicenter; beach ball shows focal mechanism (earthquake.usgs.gov); black and red polygons are pre- and post-earthquake landslides mapped in this study. **(b)** Tectonic setting of the Caribbean plate boundaries. Red star and the points are locations of main shock and major aftershock distributions, respectively. **(c)** Topographic setting (red and black bars) and mean local relief (white circles with ± 1σ whiskers) of pre- and post-earthquake landslides: alluvial plains and fans (APF), coastal cliff (CSC), deeply incised valley (DIV), dissected hilly and mountainous terrain (HDHM), round crested slopes and hills (RLH), moderately steep slopes (MR), plateau escarpments (PE), and steep faulted hills (SFH).

Fault model results show that the main seismogenic Léogâne blind thrust fault was responsible for ~80% of the seismic moment (Hayes et al., 2010). The direction of the rupture propagation mainly focused to S and SE, with increased amplitudes in the direction of rupture propagation, and decreased ground-motion in the backward direction due to source directivity (Hayes et al., 2010; Hough et al., 2010). Integration of the geodetic and seismologic data further shows that some portion of the rupture occurred as deep lateral motion on a steeply (70°) south-dipping fault (Figure 4.1b), i.e. the EPGF, in addition to slip

on thrust faults to the north (Hayes et al., 2010; Mercier de Lépinay et al., 2011).

The 2010 earthquake not only caused severe loss of lives and infrastructure, but also triggered thousands of landslides (Figure 4.1a). Here we explore the possible influence of complex fault slip, spatially variable vertical deformation, topography, and lithology on the regional distribution and abundance of coseismic slope failures. Our objective is to quantify from a detailed inventory of nearly 4,500 post-earthquake landslides the potential contributions of seismic, topographic, and rock-type controls as documented by radar remote sensing, fault-geometry models, digital elevation data, and geological maps.

4.2 Study area

Our study focuses on the main epicentral area of the 2010 earthquake in central Haiti. The regional geology of Hispaniola is characterized by NW–SE oriented sub-parallel belts of igneous, metamorphic and sedimentary rocks (Sen et al., 1988; Escuder-Viruete et al., 2007). The basement in the North of the study area is largely composed of Cretaceous to Paleogene island arc rocks (Sen et al., 1988), covered by Neogene sediments and unconformable Quaternary alluvial deposits that record sustained tectonics since the late Pliocene (Mann et al., 1984; Figure 4.2a). Eocene limestones are mainly exposed in the Momance River and in the SW of the study area: These rocks are pervasively fractured along the EPGF and Gauche River. The Cretaceous Dumisseau Formation features (pillow) basalts and minor picrites interlayered with pelagic limestones that crop out in the southern part of the study area, including the Massif de la Selle (Figure 4.2a). The basalts are deeply weathered and have lateritic profiles. Sustained uplift and erosion delivered lateritic detritus from basaltic terrain into karst structures in the adjacent limestones (Bird et al., 1992).

The left-lateral EPGF is the most prominent strike-slip fault in the region, cutting across the Southern Peninsula of Haiti at N85°E. Two M_w 7.5 earthquakes have occurred in this fault zone on 21 November 1751, and 3 June 1770 (Mann et al., 1995; Bakun et al., 2012).

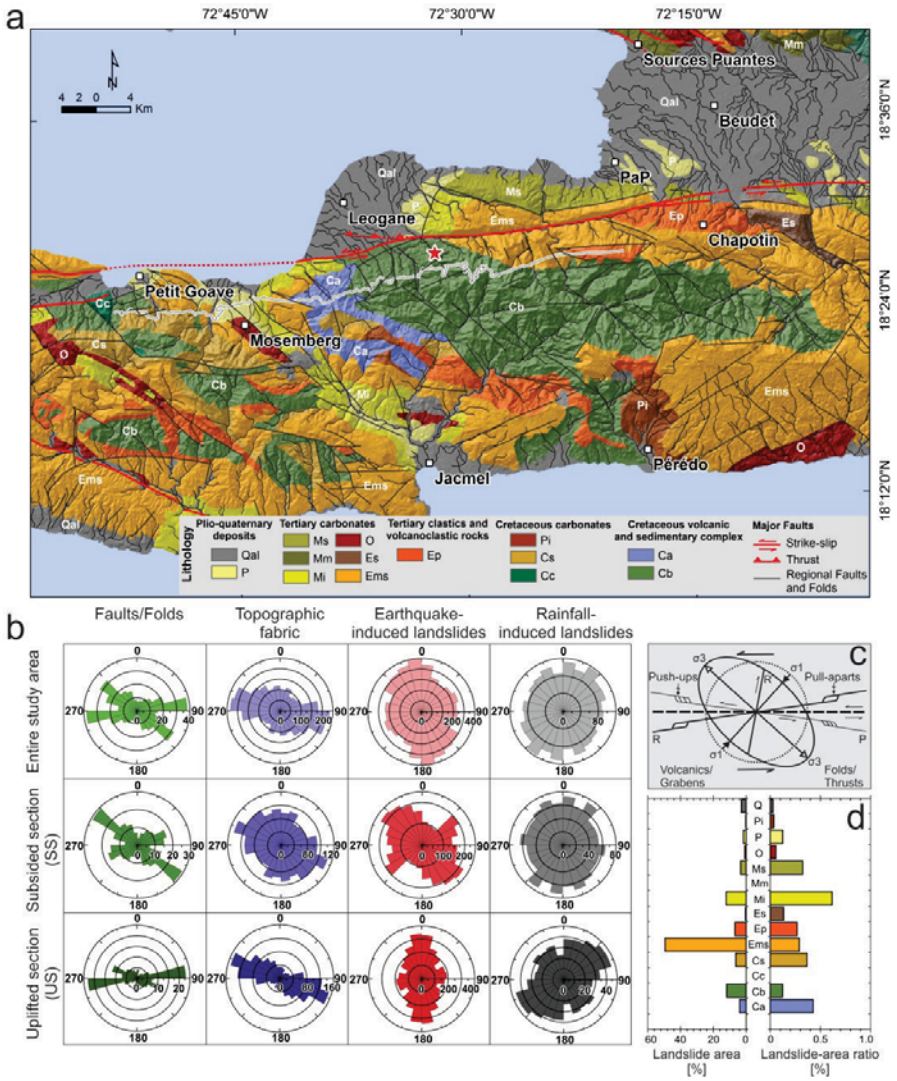

Figure 4.2 Geological setting of the study area. **(a)** Geologic map of the study area (after Lamber et al., 1987)[†]. **(b)** Rose diagrams of faults and folds, topographic fabric, and runout directions of the co- and aseismic landslides in the entire study area, and the subsided and uplifted parts, respectively. **(c)** Strain ellipse of structures predicted in a left-lateral strike-slip plate boundary zone with east-west relative plate motion (after Mann et al., 1984). **(d)** Landslide area and landslide-area ratio for each geological unit.

In the study area, the highly linear segment of the EPGF coincides with the Momance River valley that runs parallel to the fault in an E–W direction, indicating a major tectonic control on topography. The topographic grain of NW–SE and E–W directed valley and ridge systems is consistent with regional

principal stress axes. Mean elevation increases from north to south, rising up to ~2,500 m a.s.l. on the plateau. Topographic relief is high in the southern EPGF, along the central Momance valley, and the north-facing slopes of Massif de la Selle, with distinctly steeper mean hillslope gradients (~0.53) compared to the average of the study area (~0.25).

Haiti's tropical climate features periodic droughts and tropical cyclones (hurricanes), and the precipitation pattern mirrors the N–S gradient in topographic relief. The area experiences two rainy seasons per year, from April to June and from October to November, and a hurricane season from early June until the end of November. The 2010 earthquake occurred in the dry season. Haiti suffered significant losses due to the 2004 tropical storm Jeanne, which caused heavy rainfall, massive flooding, and landslides in southern Hispaniola. Additionally, Hurricanes Fay, Gustav, Hanna, and Ike heavily affected the region in 2008 (NOAA, 2012[2]).

4.3 Materials and methods

We mapped the locations and areas of individual landslides from pre- and post-earthquake high-resolution satellite images and aerial photos covering a total of ~7,000 km^2. The pre-earthquake images were high-resolution Worldview (0.5 m) and Quickbird (0.6 m), and panchromatic OrbView-3 (1 m) data. Post-earthquake images included GeoEye-1 (0.4-m) data and high-resolution Google® and Microsoft™ UltraCamG aerial photos (0.15 to 0.30 m) covering the most heavily affected region (see Figure A1 and Table A2 in appendix). Satellite images and aerial photographs were geometrically corrected using 52 ground control points (GCPs) well distributed within the post-earthquake images that predated the orthorectified GeoEye-1 and Microsoft™ UltraCamG aerial photos. We used a polynomial nearest neighbor re-sampling method and

[2] Qal: Quaternary alluvium, P: Pliocene weakly cemented sandstones, marls, and clastic deposits, Ms: Late Miocene limestone, marls, and sandstone, Mm: Middle Miocene blue-grey marls and neritic limestone, Mi: Early Miocene flysch and limestone, O: Oligocene chalk and marly limestone, Es: Late Miocene pelagic limestone, Ems: Middle to Late Miocene limestone, Ep: Late Paleocene – Early to Middle Eocene conglomerates, sandstone and volcanoclastics (Massif de la Selle), Cs: Senonian pelagic limestone, Pi: Cretaceous marls and, marly limestone Cc: Cretaceous limestone interlayered with reddish marls Ca: Cretaceous volcanic and altered volcanic rocks, intermediate lava and pyroclastic rocks and Cb: Cretaceous tholeiitic and sedimentary complex (fm. Dumisseau) pillowed and massive basalts and minor picrites interlayered with pelagic limestones. White thick line is vertical deformation signal from InSAR (Hayes et al., 2010) delimiting boundary between uplifted northern and subsided southern parts of earthquake-affected region.

the GCPs to establish a transformation model for producing georectified images. The average georectification accuracy has a root mean square error (*RMSE*) of <1 pixel. Overlays of pre- and post-earthquake images did not produce any visible mismatches. We mainly used images with cloud and shadow coverage of <0.4% of the study area.

Visual landslide detection was based on true-color composites and panchromatic images, using monoscopic image interpretation. To identify individual slope failures in the high-resolution images, we used diagnostic features such as differences in shape, size, color, tone, texture, and landform assemblages (van Zuidam 1985; van Westen et al., 2008; Fiorucci et al., 2011; Gorum et al., 2011; Fan et al., 2012a,b). We further used oblique-aerial photos taken from helicopters shortly after the earthquake (US Geological Survey, 2010; http://cires.colorado.edu/~bilham). We mapped 4,492 coseismic landslides in total, though consider this an underestimate given some noise between pre- and post-earthquake imagery, which precluded clear recognition of landslide areas <20 m^2. Assuming that landslides mapped from images predating the 2010 earthquake were triggered mainly by rainstorms, we distinguished aseismic from coseismic, i.e. post-2010, landslide inventories. We computed the spatial density [km^{-2}] and the fraction of area [%] affected by landslides within a moving window of 1-km radius using a Gaussian kernel density estimator. To quantify the net effect of the earthquake on the abundance of landslides, we computed a re-activation rate [%] based on the comparison of the pre-earthquake landslide areas with the extent of coseismic landslide areas.

In order to assess the role of topography and surface-rupture process on the distribution of coseismic landslides, we combined various terrain metrics with available data on lithology and the distribution of vertical coseismic deformation. Regional-scale coseismic deformation rate and rupture process of the earthquake are part of a detailed rupture model based on a joint inversion of interferometric synthetic aperture radar (InSAR), field based off-sets measurements, and teleseismic body-wave data (Hayes et al., 2010). We computed hillslope gradient S_h from an ASTER Global Digital Elevation Model version 2 (GDEM-2) with a pixel resolution of 30 m using a best-fit plane in a 3×3 moving window. Local topographic relief *H* was computed from the same data as the maximum elevation range within a 1-km radius. We also computed a vector ruggedness measure (*VRM*) based on the dispersion of normal vectors of the terrain surface (Sappington et al., 2007) as a proxy of topographic response

during the earthquake, incorporating variability in both slope aspect and gradient .

For exploring the potential effects of rock types on the occurrence of coseismic landslides, we digitized the scanned and orthorectified outlines of major tectonic structures and lithological units compiled by Lamber et al. (1987) at 1:250,000 scale. We derived density estimates of S_h for selected homogenous rock types in uplifted and subsided sections of the study area following the method of Korup (2008). The peaks of these distributions can be used as proxies for rock-mass strength at the regional scale (Korup 2008; Korup and Schlunegger 2009; Korup and Weidinger 2011), and allow assessing the susceptibility of rock type to coseismic landsliding. We excluded areas of low coseismic landslide density (<0.01%) from this analysis. We plotted the coseismic deformation rate, landslide density, local relief and slope gradient along two swath profiles across the earthquake region, centered on the blind fault ruptures and the regions of maximum vertical coseismic deformation. Finally, we compiled inventories of coseismic landslides documented from recent reverse or thrust-faulting earthquakes that serve as a reference for linking fault geometries and rupture dynamics with regional patterns of coseismic landsliding.

4.4 Results

4.4.1 Regional landslide distribution

The 2010 Haiti earthquake triggered at least 4,490 landslides over an area of ~2,250 km^2, and up to a distance of ~46 km from the epicenter. The pre-2010 landslide inventory contains 22 potentially prehistoric and 1,273 recently active landslides. The 2010 earthquake more than tripled the landslide abundance. Prehistoric, recent aseismic, coseismic landslides affected 19.4, 16.5 and 8 km^2, respectively. We find that 572 landslides were re-activated during the 2010 earthquake, affecting a total of 0.7 km^2, or <0.04% of the study area. Thus some 700 pre-existing aseismic landslides were not re-activated by the 2010 Haiti earthquake.

The majority of coseismic landslides clustered in a 5-km wide corridor around the junction of the blind ruptures of the Léogâne fault and EPGF zones (Figure 4.3). Instead of focusing on the hanging wall, most failures largely affected hillslopes of the Momance River valley, mountainous areas in the southern part of the study area, and in the deeply incised valleys of the southern EPGF. Most

coseismic landslides were shallow rock and debris falls, involving the top few meters of strongly fractured and weathered bedrock, regolith, and lateritic soil (Jibson and Harp, 2011). Bedrock failures occurred mainly in the Eocene and the Upper Miocene limestones (Figure 4.2c). In contrast, most of the aseismic landslides were soil and debris landslides that clustered in the thick lateritic horizons of the deeply weathered basalts, especially in the southern parts close to the EPGF (Figure 4.2a). Several lateral spreads occurred in artificial fills and unconsolidated Quaternary deposits in the Port-au-Prince and Léogâne coastal fan delta (Figures 4.1a and 4.2a).

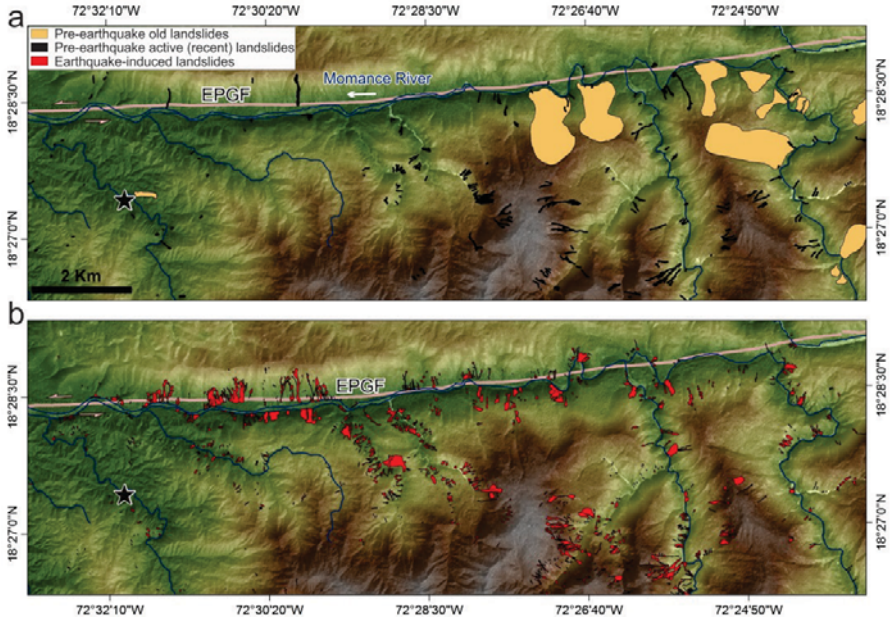

Figure 4.3 Distribution of **(a)** coseismic and **(b)** aseismic landslides along a reach of the Momance River, Haiti; red star is location of 2010 earthquake epicenter; white arrow is flow direction. Old landslides may likely be of prehistoric origin.

Landslides were also abundant in the higher parts of the Gauche River valley that follows a major NW-SE plunging fold axis overlaying strongly fractured Upper-Miocene limestones (Figures 4.1a, 4.2a); one third of the coseismic landslides in this valley were re-activated failures. About 85% of both aseismic and coseismic landslides occurred in the SW facing valley slopes of Gauche River valley. The dominant orientation of the coseismic landslides is consistent with the principal direction of neotectonic compression in the region. The landslide distribution in the uplifted section north of the fault and in the subsided southern section changes with major tectonic structures (Figure 4.2b).

Dominant neotectonic and topographic structures have E–W and NW–SE orientations, with narrow, deeply eroded valleys and steep mountain slopes containing >60% of the coseismic landslides; >80% of the landslides in these areas involved bedrock.

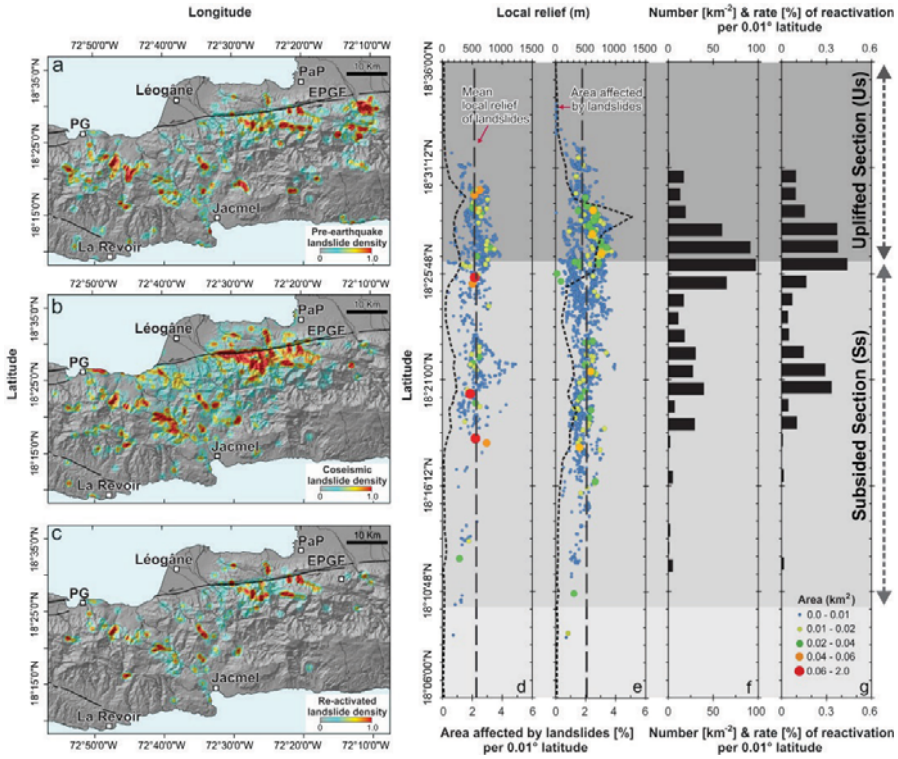

Figure 4.4 Regional distribution of co- and aseismic landslides, and re-activated slope failures. **(a)** Normalized spatial density of pre-earthquake aseismic landslides within 1-km radius (see text). **(b)** Spatial density of coseismic landslides. **(c)** Spatial density of re-activated landslides. **(d and e)** Fraction of area affected by (d) aseismic and **(e)** coseismic landslides per 0.01° latitude; circles are individual landslide locations scaled by area (see legend in panel g). Thin black dashed lines are areas affected by the landslides; thick black dashed lines are mean local relief of coseismically uplifted and subsided areas. **(f** and **g)** Histograms of (f) point density [km^{-2}] and **(g)** rate [%] of re-activated landslides for 0.01° latitude bins; PaP: Port-au-Prince; PG: Petit Goave.

In contrast, the orientation of the aseismic landslides is independent of the region's principal stress axes (Figure 4.2b), with >55% occurring in densely dissected hilly to mountainous terrain (Figure 4.1c).

The spatial abundance of coseismic landslides is high in the Momance River valley and up to ~5 km beyond to the south (Figure 4.4a). Aseismic and

coseismic landslide density varies from north to south, with a minimum in the SW plateau, where seismic re-activation was low (Figure 4.4). Much higher landslide densities occur in the north of the EPGF, but decrease dramatically in the eastern extension of the fault (~72.18° N). In the south, except for the upper section of the Gauche valley, and in the east, the peaks of aseismic landslide abundance are more randomly distributed compared to those of the coseismic slope failures (Figure 4.4a, b). A swath profile across the south-central part of Haiti underlines these gradients in aseismic and coseismic landslide density and re-activation rate (Figure 4.4d-g). In the low-gradient deltas, coseismic landslides affected 0.2% to 5% of the area. Coseismic landsliding rates increase to 5% on steeper slopes of the Momance valley, where maximum aseismic landsliding rates are up to 2% (Figure 4.4d,e). Nearly 40% of the total coseismic landslides occurred in these valley slopes, including the largest slope failures along the Momance River up to the eastern termination of the blind ruptures of the Léogâne and EPGF (Figure 4.4b,e). Further south, the area near the boundary between uplifted and subsided sections has the highest re-activation rates. Re-activated landslide numbers and the rate of re-activation gradually decrease from >95 km^{-2}, and 0.5% to <65 km^{-2}, and 0.2% towards to the south, respectively (Figure 4.4f, g). Despite this decrease, re-activation rates increase again with a distinct peak in the upper catchment the Gauche River (18.18°–18.22° N, Figure 4.4f, g).

4.4.2 Coseismic deformation and fault rupture geometry

The complex rupture of the 2010 earthquake generated two major deformation areas: the first is the uplifted section that covers a corridor 5 km south of the EPGF zone up to the alluvial fan deltas in the north; and the second is along a subsided section covering the mountainous areas to the south (Figure 4.5a). Vertical deformation ranged from −0.6 to +0.6 m (Hayes et al., 2010), with most coseismic landslides clustering in areas with +0.01 to +0.3 m offsets (Figure 4.5). Landslide abundance shows no clear relationship with vertical deformation rate. For example, the number of landslides, mainly lateral spreads and shallow debris falls and slides, in coastal parts of the Léogâne fan delta is limited despite the high coseismic vertical offsets of up to +0.6 m (Figure 4.5a, b). These offsets are three times higher than those in the peak areas of landsliding east of the epicenter. Visual inspection shows that clustering of coseismic landslides spatially coincides with the coseismic fault geometries. Landslide abundance in the high-elevation southern slopes of the EPGF is

bracketed by the up- and down-dip edges of the coseismic rupture (Figure 4.5c, d).

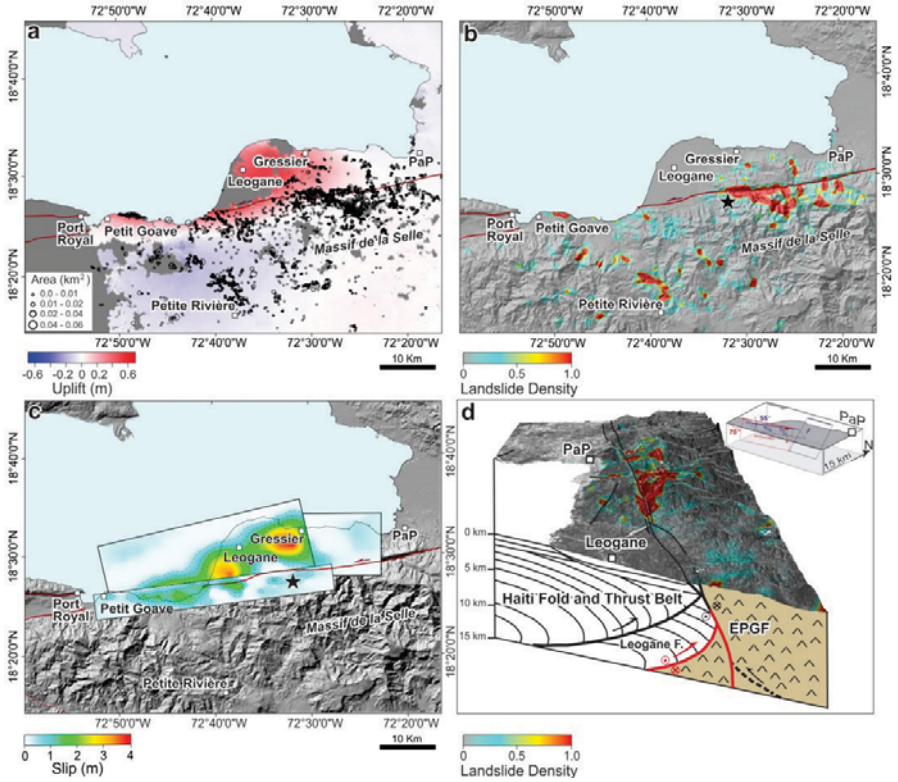

Figure 4.5 Distribution of coseismic deformation, slip, and landslide density. **(a)** Vertical-deformation signal from InSAR (after Hayes et al., 2010); black circles are mapped coseismic landslides; black star is epicenter. **(b)** Normalized landslide density map (cf. Figure 4.4). **(c)** Rupture model and coseismic slip amplitudes from inversion of InSAR data, field based off-set measurements, and broadband teleseismic body-waveform data (after Hayes et al., 2010). **(d)** Block diagram of the Léogâne thrust and Enriquillo-Plantain Garden Fault blind rupture. Normalized landslide density superimposed on data by Mercier de Lépinay et al. (2011). Inset block diagram shows proposed fault geometry by Hayes et al., (2010) for Haiti earthquake ruptures. Thick solid lines are surface projections of each fault; PaP: Port-au-Prince.

Coseismic landslide occurrence in the S and SW of the epicenter is consistent with the direction of rupture propagation (directivity), indicating that the dominant southward direction of coseismic slip could have caused increasing ground-motion amplitudes southward.

4.4.3 Hillslope steepness and rock-type effects

Density estimates of hillslope gradients for four paired sample regions of homogeneous lithologies in which the majority of coseismic landslides occurred shows that different rocks have differing modal hillslope inclinations. These modes are not uniform across the uplifted and subsided sections (Figure 4.6a, b). Hillslope gradients of the rocks in the subsided section (Ss), except for the Miocene limestone (Ems), have higher modes than the homogenous counterparts in the uplifted section (Us; Figure 4.6a, b). Cretaceous volcanic rocks (Ca) and Early Miocene flysch and limestones (Mi) have modes at S_h ~0.35, and ~0.32, which are substantially below those of the Cretaceous tholeiitic-sedimentary complex (Cb), and Miocene limestone (Ems) in both sections of the blind ruptures (Figure 4.6a, b), i.e. S_h ~0.42 and ~0.52, respectively.

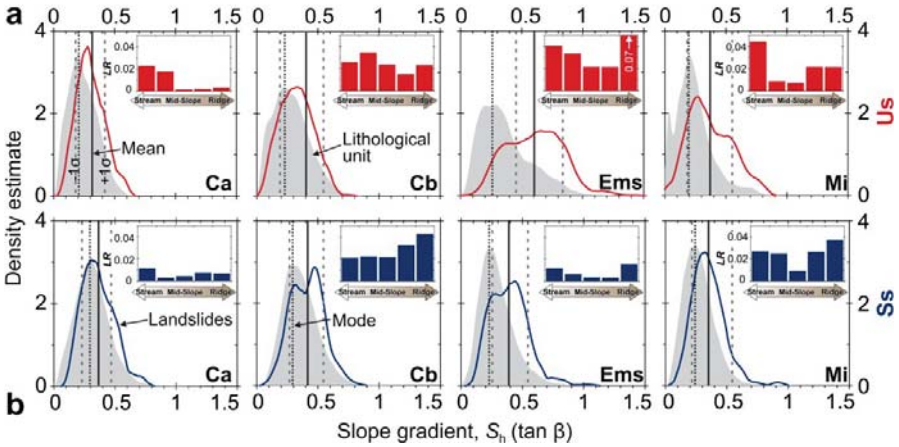

Figure 4.6 Gaussian kernel density estimates of hillslope gradient in selected homogenous rock types in areas affected by coseismic **(a)** uplift (US), and **(b)** subsidence (SS). Samples are from 30-m ASTER DEM within 1 km radius, exclusive of low-gradient valley fills. Grey shades are hillslope gradients; red and blue thick lines are hillslope portions affected by landslides. Inset histograms show topographic position of coseismic landslides per rock type. Histograms bars (from left to right) are streams, lower, mid-, and upper slopes, and ridge crests derived from topographic position index (Jenness, 2006). Landslide ratio (*LR*) is fraction of area affected by landslides per rock type.

Many of the coseismic landslides in *Ca* are clustered in the altered parts of the volcanic rocks, occurring at the base of slopes in the form of shallow soil landslides (Figure 4.6a, b). On the other hand, Early Miocene flysch and limestones (Mi) sustain mainly bedrock landslides and the coseismic landslides in the subsided section occur in distinctly steeper slopes than their nearby (<10

km) counterparts in the uplifted sections in terms of both mean and modal slope gradients.

When comparing rock types in the uplifted and subsided sections, the steepest slope gradients occur in the Ems unit in the uplifted section (north), which also contains 45% of all coseismic landslides. Except for this unit, the slope gradients of coseismic landslides are generally higher in the rocks of the subsided section where coseismic landslides are considerably close to upper slopes and ridges crests.

The vector ruggedness measure (*VRM*) of individual landslides is high in the subsided section and where deformation is between 0.01 and 0.1 m, along the Momance River in the uplifted section. The lowest *VRM* occurs mostly in the northern part of the uplifted section. We also find that the mean *VRM* of individual coseismic landslides in the subsided as well as the southern part of the uplifted sections exceeds the overall mean *VRM* of the earthquake struck region by a factor of ~2.5 (Figure 4.7a, b).

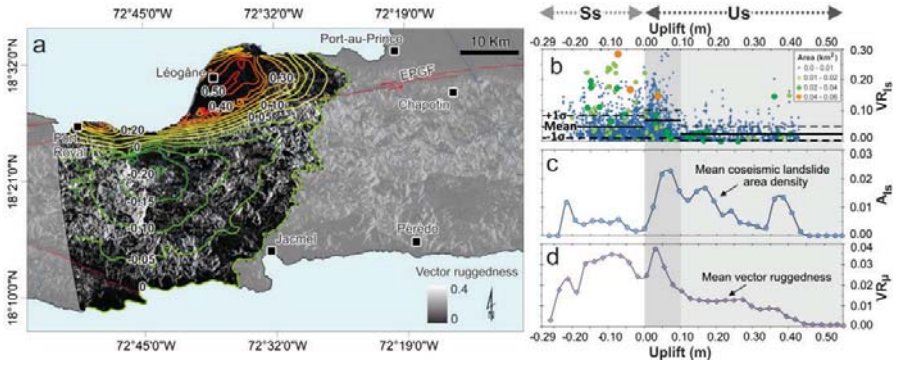

Figure 4.7 Terrain roughness of coseismic landslides in relation to coseismic uplifts in epicentral region. **(a)** Vector ruggedness map displayed in grey tones with positive (uplift) and negative (subsidence) contour lines extracted from vertical-deformation signals of InSAR based on the range of high signal/noise (S/N) ratio (Hayes et al., 2010). **(b)** Vector ruggedness measure (*VRM*) values of individual landslides. **(c)** Mean coseismic landslide area density as a function of coseismic uplift. **(d)** Mean vector ruggedness variations. Black thick and dashed lines are means and ± 1 σ, respectively, circle size and color scaled by landslide area.

4.5 Discussion

4.5.1 Combined effect of complex rupture mechanism and topography

Coseismic landslide abundance varies strongly with topographic relief and coseismic deformation in the study area. The W–E swath profile highlights the

spatial coincidence of peaks in coseismic landslide abundance with the highest relief and steepest hillslopes in the uplifted section (Figure 4.8a, Section 3 (S3)), hosting >80% of the mapped coseismic landslides. Although still observed in this section, coseismic deformation was below average. While the delta and low hilly zone in the west (Figure 4.8a (S2)) were subjected to the highest coseismic deformation, the below-average local relief and hillslope gradients dampened coseismic landslide density, which strikingly mimics the trends of mean local relief and slope gradient over >70 km (Figure 4.8c, d).

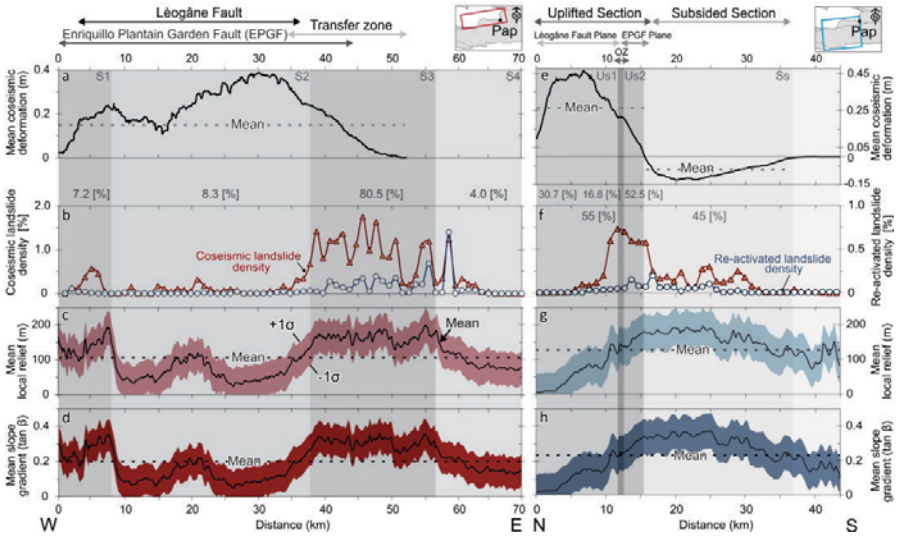

Figure 4.8 Along-strike (W–E) distribution of **(a)** mean coseismic deformation (Hayes et al., 2010), **(b)** coseismic and re-activated normalized landslide density, **(c)** mean local relief, and **(d)** mean hillslope gradient in the uplifted section. N–S distribution of (**e)** mean coseismic deformation (Hayes et al., 2010), **(f)** coseismic and re-activated landslide density, **(g)** mean local relief, and **(h)** mean hillslope gradient in both uplifted and subsided parts. Inset maps show locations of the swaths. Black lines **(c, d, g** and **h)** and red/blue shading are means and ± 1 σ in 60-m bins. Light and dark grey boxes delimit peaks in normalized landslide density **(b),** and sub-sections of differing dominant fault geometries in **(e)**. Dashed grey lines are regional means; scale differs between panels **(b** and **f)** in coseismic and re-activated landslide density.

The abrupt decrease in landslide density coincides with the lowest deformation at the eastern termination of the blind ruptures (Figure 4.8a). From this point eastward, landslide density values increase slightly, with a significant fraction of re-activated slope failures (Figure 4.8b). Although mean local relief in the terrain where aseismic landslides occur is higher than in areas affected by coseismic landslides, the reason for the clustered occurrence of coseismic landslides in the deeply incised valleys may be due to topographic amplification.

The N–S swath profile affords a more explicit picture of the combined effect of fault ruptures and topography on the coseismic landslide pattern, with 55% of the coseismic landslides located in the uplifted section (Figure 4.8e, f). The lowest coseismic landslide density is in the northern part of the uplifted section despite high coseismic uplift rates, due to the low relief. The peak values of the coseismic landslide densities in the uplift section are in the southern part of the blind ruptures (Figure 4.8e, f, Uplifted section1 (Us1)). Most prominent in this section with few landslides are the below-average local relief and slope gradients. Areas with high landslide abundance in the 8-km narrow zone of the uplifted section had higher (or comparable) mean coseismic deformation, local relief and the slope gradient values compared to the overall mean (Figure 4.8e–h). The spatial distribution of the landslide density in the subsided section differs from the uplifted section in terms of having lower density of landslides and more disperse distribution.

Despite the high values of mean local relief and slope steepness we infer that subdued landslide density peaks and the disperse distribution of the landslides are linked to first order with comparatively low rates of the coseismic deformation in the subsided section, which was relatively stationary and acted as a passive block during the earthquake. The earthquake also radiated some energy towards the southern part and the area affected by the landslides is nearly equal (i.e. 3.95 km^2) to that of the uplifted section. This nearly equal proportion is at odds with the area proportions of landslides triggered by thrust earthquakes reported previously.

The topographic response of the rugged terrain during the earthquake also differed in the uplifted and subsided sections (Figure 4.7), likely because of seismic site effects. Coseismic landslides tend to preferentially occur on hillslopes inclined slightly steeper than the modal slope gradient, a finding that has been confirmed in many landslide-prone mountain ranges such as the United States (Wolinsky and Pratson, 2005), New Zealand (Korup, 2008), the Swiss Alps (Korup and Schlunegger, 2009), or Japan (Iwahashi et al., 2001, 2003). Topography can further change peak ground accelerations (*PGA*) values by ±50% in rugged terrains such as deeply incised valleys, ridges, steep slopes and cliffs (Faccioli et al., 2002; Paolucci, 2002; Meunier et al., 2008; Shafique et al., 2011). Judging from their topographic location (Figure 4.6), terrain roughness and structural characteristics (Figures. 4.2b and 4.7), we infer that seismic site effects were prevalent in the subsided and southern part of the uplifted sections.

Yet this cannot be directly shown with the seismic data because Haiti is a poorly seismic instrumented region. The coseismic landsliding rate with respect to topography differs in the deeply incised valleys and hilly terrains. In the Momance and Gauche River basins, coseismic landsliding rate is high and preferably attacking ridges and upper slopes. However, this pattern is not evident in many parts of the uplifted section (Figure 4.6a).

4.5.2 Comparison with other thrust-faulting earthquakes

For a given magnitude, reverse and thrust-faulting earthquakes produce higher ground motion than strike-slip or normal-faulting earthquakes (Campbell, 1981; Oglesby et al., 1998, 2000a). Also, hanging walls of reverse or thrust faults generally have higher peak ground acceleration (*PGA*; Abrahamson and Somerville, 1996; Abrahamson and Silva, 1997). Campbell (2003) attributed this hanging-wall effect to a combination of radiation pattern, source directivity, and trapping of seismic waves within the hanging-wall wedge of the fault. This type of faulting may further enhance erosion rates because of elevated hanging walls through a gain in potential energy (Molnar et al., 2007), and reduced rock-mass strength from repeated seismic hanging-wall shattering (Korup, 2004).

Distinct asymmetric hanging-wall clustering of landslides triggered by thrust earthquakes supports this notion (Figure 4.9). Inventories demonstrate the preponderance of coseismic landslides in the hanging wall for the 1999 Chi-chi,Taiwan (M_w 7.6), the 2008 Wenchuan, China (M_w 7.9), and the 2008 Iwate-Miyagi Nairiku, Japan (M_w 6.9) earthquakes (Liao and Lee, 2000; Yagi et al., 2009; Gorum et al., 2011). However, landslides triggered by the 1994 Northrigde (M_w 6.7), and 2010 Haiti (M_w 7.0) earthquakes were nearly symmetrically distributed about the seismogenic fault (Figure 4.9). The 2010 Haiti earthquake also differs from other thrust earthquakes of comparable magnitude because of its blind rupture.

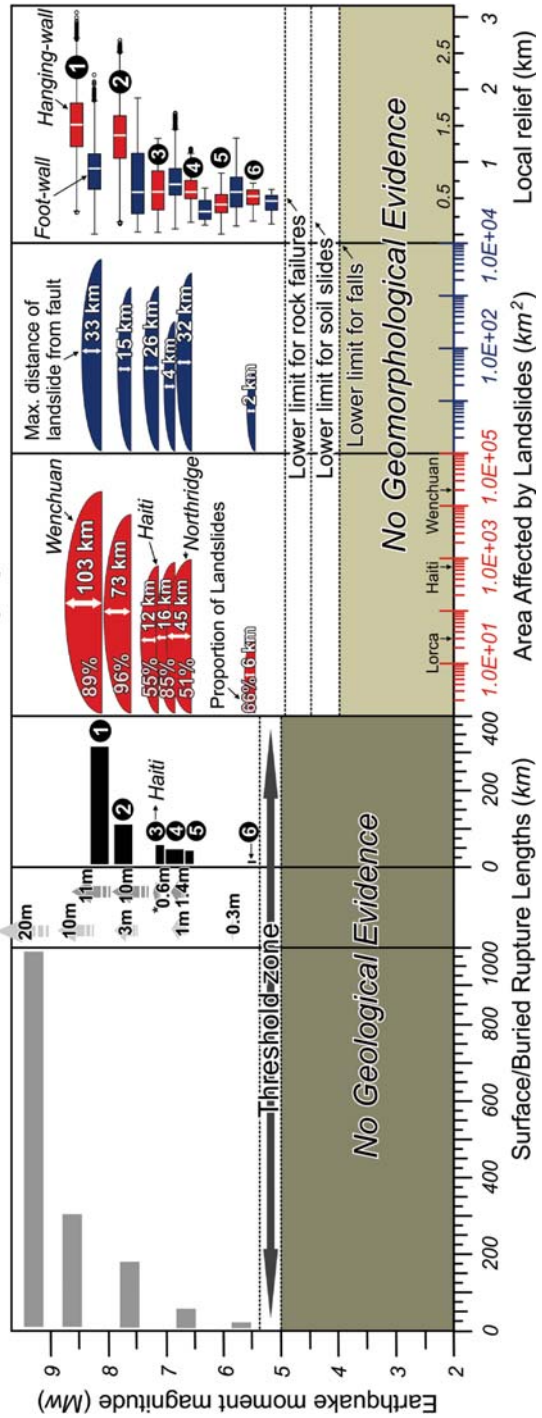

Figure 4.9 Summary of coseismic landslide inventory data from documented reverse or thrust-fault earthquakes. Left panel shows extent of faulting recorded in historical (grey bars) and recent earthquakes (grey bars; modified after McCalpin, 2009). Thick and thin black bars are lengths of surface and blind fault ruptures; estimates of surface rupture lengths (grey bars) and maximum coseismic uplift (light grey arrows) from Wells and Coppersmith (1994); lower limits from Bonilla (1988). Maximum coseismic uplift (*MCU*, dark grey arrows) and surface/blind ruptures: (1) Wenchuan, China, M_w 7.9 (Liu-Zeng et al., 2009); (2) Chi-Chi, Taiwan, M_w 7.6 (Chen et al., 2003); (3) Haiti *Mw* 7.0 (Hayes et al., 2010); (4) Iwate-Miyagi, Japan, M_w 6.9 (Ohta et al., 2008); (5) Northridge, USA, M_w 6.7 (Shen et al., 1996); and (6) Lorca, Spain, M_w 5.2 (Martinez-Diaz et al., 2012). Right panel shows hanging wall (red) and foot-wall (blue) areas affected by coseismic landsliding, and box-and-whisker plots of local relief. Box delimits lower and upper quartiles and median; whiskers are 5th and 95th percentiles; open circles are outliers. Landslide inventory data from Gorum et al. (2011), Liao and Lee (2000), Yagi et al. (2009), Harp and Jibson (1995), and Alfaro et al. (2012); landslide lower limits are from Keefer (1984).

The event is similar to the 1994 Northridge earthquake (M_w 6.7)—which was also a blind rupture, though triggered 11,000 landslides—in terms of the ratio of coseismic hanging-wall to foot-wall landslides. The peculiar abundance of landslides triggered by the 1994 Northridge earthquake, given its magnitude, may be explained by the unusual large ground motions that indicated higher-than-average dynamic stress drops (Shen et al., 1996). Overall, we find that the ratio of coseismic hanging-wall to foot-wall landslides is lower in blind rupture earthquakes than in surface-rupture earthquakes (Figure 4.9).

Distinct asymmetric hanging-wall clustering of landslides triggered by thrust earthquakes supports this notion (Figure 4.9). Inventories demonstrate the preponderance of coseismic landslides in the hanging wall for the 1999 Chi-chi,Taiwan (M_w 7.6), the 2008 Wenchuan, China (M_w 7.9), and the 2008 Iwate-Miyagi Nairiku, Japan (M_w 6.9) earthquakes (Liao and Lee, 2000; Yagi et al., 2009; Gorum et al., 2011). However, landslides triggered by the 1994 Northrigde (M_w 6.7), and 2010 Haiti (M_w 7.0) earthquakes were nearly symmetrically distributed about the seismogenic fault (Figure 4.9). The 2010 Haiti earthquake also differs from other thrust earthquakes of comparable magnitude because of its blind rupture. The event is similar to the 1994 Northridge earthquake (M_w 6.7)—which was also a blind rupture, though triggered 11,000 landslides—in terms of the ratio of coseismic hanging-wall to foot-wall landslides. The peculiar abundance of landslides triggered by the 1994 Northridge earthquake, given its magnitude, may be explained by the unusual large ground motions that indicated higher-than-average dynamic stress drops (Shen et al., 1996). Overall, we find that the ratio of coseismic hanging-wall to foot-wall landslides is lower in blind rupture earthquakes than in surface-rupture earthquakes (Figure 4.9).

This finding awaits further confirmation from future earthquake triggered landslide events. However, the attenuation relation for PGA on rock-site conditions considering the hanging wall scaling, shows a step in the ground motion from the hanging wall to the foot wall for surface-rupture earthquakes (Abrahamson and Silva, 2008). The difference in ground motion between hanging walls and foot walls is more pronounced for surface rupture-earthquakes, with the ground motion focusing on the hanging wall. For the case of blind-rupture earthquakes the transition of the ground motion proportion between the hanging wall and the foot wall is smooth, although the ground motion ratio remains higher on the hanging wall (Abrahamson and Silva, 2008). Short-period ground motions observed during blind-rupture earthquakes

correspond to higher-than-average dynamic stress drops (Campbell, 2003), possibly due to a lack of surface rupture (Somerville, 2000; Sommerville and Pitarka, 2006) or small total fault slip (Anderson, 2003).

During surface-rupture earthquakes the seismic energy focuses more to the surface, and significant increase in the static stress drop in terms of mean displacement may cause more coseismic landslides near the fault. Additionally, shear stress increases near the coseismic fault during surface-rupture earthquakes, depending on the width of the deformation zone and the coseismic slip amplitude (King et al., 1994; Harris, 1998; Stein, 1999). This may not only cause very large coseismic landslides in the hanging wall in a wide corridor (~8 km) along surface-rupturing faults. It also elevates the fraction of the area affected by slope failures up to six times higher compared to other sections (Liao and Lee, 2000; Gorum et al., 2011). Yet the most abundant size of landslides triggered by the 2010 earthquake is below those triggered by other surface-rupture earthquakes (Figure 4.10).

Comparing landslide inventories of reverse or thrust-fault earthquakes with regard to potential controls of magnitude, occurrence of surface ruptures, and local relief, on mass-wasting response shows that seemingly minute differences do matter (Figure 4.9). The number of coseismic landslides appears to be mainly controlled by earthquake magnitude rather than by whether the rupture breaks the surface or not. Yet mass-wasting responses to earthquakes of similar magnitudes differ significantly. For example, the 2008 Iwate-Miyagi Nairiku, Japan (M_w 6.9) earthquake had a lower magnitude and affected areas of lower relief compared to the 2010 Haiti (M_w 7.0) event, though the hanging-wall effect was more pronounced and the landslides were larger in general (Figures 4.9 and 4.10). Additionally, the hanging wall of the blind thrust-earthquakes are morphologically less expressed than those of the surface rupture-earthquakes, which may reflect that they are either recently established faults or simply older faults with rates of fault growth being outpaced by rates of erosion (Figure 4.9).

Overall, different coseismic mass-wasting responses may be driven not only by magnitude, but also blind faulting, and low hanging-wall relief. Studies on earthquake triggered landslides have so far largely neglected potential controls of fault geometry and rupture in this context. We surmise that the abundance, distribution pattern and size of coseismic landslides differ between blind and surface-rupturing earthquakes. Our study of the 2010 Haiti earthquake shows that this, together with the regional differences in geomorphology and tectonic setting, is essential in governing the pattern of coseismic landslides. Likewise,

we find that the hillslope location of coseismic landslides is variable, and divergent from the pattern documented from previous earthquakes (Meunier et al., 2008).

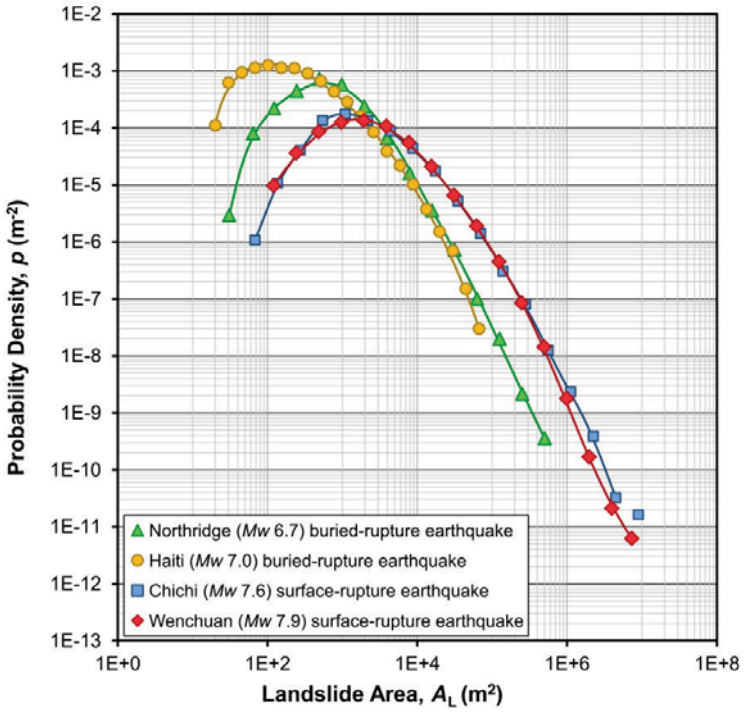

Figure 4.10 Probability density of log-binned landslide deposit areas for blind and surface rupture-earthquakes (M_w 7.9 Wenchuan, China, 2008; M_w 7.6 Chi-Chi, Taiwan, 1999; M_w 7.0 Haiti, 2010; and M_w 6.7 Northridge, USA, 1994).

4.6 Conclusion

We show that the abundance, spatial pattern, and size distribution of coseismic landslides differs between blind and surface-rupturing earthquakes. Our study of the 2010 Haiti (M_w 7.0) earthquake shows that this, together with regional differences in topography and tectonic setting, is essential in governing the pattern of coseismic landslides. The earthquake triggered nearly 4,500 landslides; 55% of these were located within the area uplifted during the earthquake. Distinct clusters of slope failures coincided with areas of extreme local relief and hillslope gradients. This pattern corroborates the notion that landslide-density changes mimic variations in coseismic deformation together with high topographic relief in the uplifted section. In contrast, landslides are more disperse in coseismic subsidence areas where topography is high, although

the total landslide-affected area differs little. This is mainly due to low deformation and the limitation of slope failures to areas of varying topographic roughness and hillslope steepness. Landslide re-activation played an important role in this subsided section, and helps to gauge better the net coseismic landslide production. The absence of coseismic landslides in the high-relief southwestern parts indicates that the distribution of seismic energy is limited, also given that numerous pre-earthquake active landslides in this area were not re-activated.

Comparison of coseismic landslide inventories indicates that blind rupture-earthquakes induced fewer landslides than surface rupture-earthquakes on thrust or reverse faults. The location, abundance, and area affected by coseismic landslides are linked with first order to the type and daylighting of rupture, local topographic relief, and earthquake magnitude. The frequency-size distribution and total area of landslides triggered by the 2010 Haiti earthquake is below those of similar magnitude events, mainly because of the lower static stress drop and mean fault displacement during a blind rupture. The directivity of rupture propagation amplified local topographic differences that superpose the symmetric pattern of the coseismic landslides. Our results provide a testable hypothesis for further quantifying the effects of the surface or blind rupture-earthquakes on coseismic landsliding. Thus, research on coseismic landslides needs a larger number of complete inventories together with more comprehensive study of earthquake triggered landslides in the future.

5 The role of fault-rupture dynamics on the abundance and the spatial pattern of earthquake triggered landslides: Global and regional perspectives[1]

5.1 Introduction

Strong earthquakes are capable of triggering several thousands of landslides, which may incur substantial damage to people and infrastructure, degrade soil and water resources, and often surpass losses caused by seismic shaking alone (Plafker et al., 1971; Keefer, 1984; Harp and Jibson, 1995; Sassa et al., 1995; Rodríguez et al., 1999). Studies on the spatial distribution of coseismic landslides have traditionally focused on earthquake magnitude and environmental setting as the potential governing controls (Keefer, 1984; Harp and Jibson, 1995; Rodríguez et al., 1999). The common notion is that spatial clustering of coseismic landslides is controlled by a combination of factors related to the triggering fault, such as earthquake magnitude, distance from the epicenter or the ruptured fault, as well as topography, lithology, or structural geological setting (Tibaldi et al., 1995; Scheidegger, 1998; Densmore and Hovius, 2000; Meunier et al., 2007). Although landslide density decreases with distance away from earthquake epicenters, a substantial scatter in this decay cannot be explained sufficiently by differences in earthquake magnitude or environmental setting (Figure 5.1).

Despite comparable magnitude, length of surface rupture, average coseismic slip, and topography, historic earthquakes have triggered highly divergent landslide response, which cannot be represented by simple empirical relationships as currently used in susceptibility and hazard assessments (Keefer, 2000; Khazai et al., 2003). For example, the 2002 Denali, Alaska, and 2008 Wenchuan, China, earthquakes had similar magnitudes (M_w 7.9) and lengths of surface rupture, and occurred in steep, tectonically active mountain ranges (Haeussler et al., 2004; Xu et al., 2009). Yet the Wenchuan earthquake (Figure 5.2) produced forty times more landslides than the Denali event (See Chapter 3).

[1] This chapter is based on the following paper: Gorum, T., van Westen, C.J., Korup, O., van der Meijde, van der Meer, F.D., Fan, X., Dai, F.C., (in preparation). Fault-rupture dynamics recorded by earthquake triggered landslide abundance. *Geophysical Research Letters*.

This significant variability may be rooted in differing faulting style and geometry affecting rupture speed, slip distribution, and peak ground motion. Dynamic rupture simulation models demonstrate that, for the same initial stress magnitude, reverse faults produce higher ground motion than normal faults (Duan, 2010; Oglesby et al., 1998; 2000a and 2000b), which in turn generally exceeds the values for strike-slip faults (Oglesby et al., 2000a). Because non-vertical faults cause seismic waves to be reflected off the free surface back onto the fault (Oglesby et al., 2000a and 2000b), ruptures of thrust and reverse faults cause stronger ground motion in their hanging walls (Cocco and Rovelli, 1989; Abrahamson and Somerville, 1996).

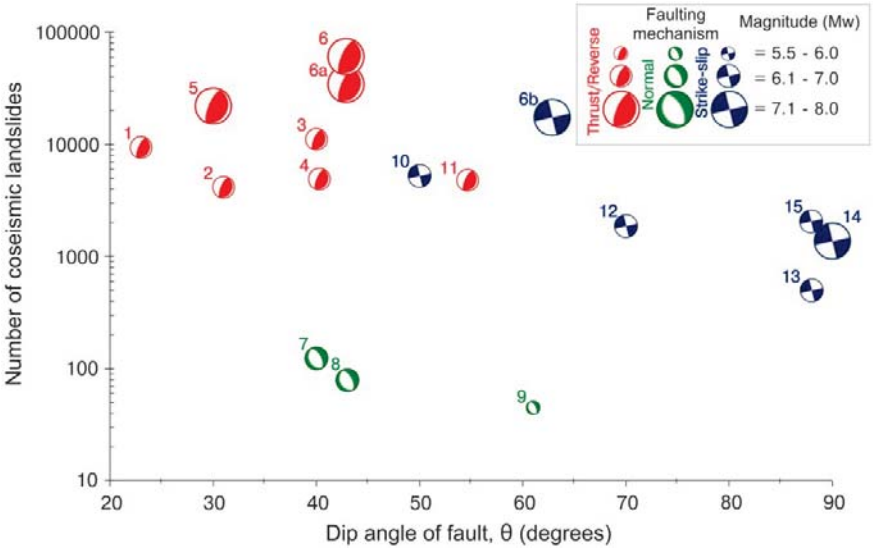

Figure 5.1 Total numbers of earthquake triggered landslides as a function of magnitude of earthquake, dip angle and faulting mechanisms. (1) M_w 6.5 Coalinga, USA (1983); (2), M_w 6.9 Iwate-Miyagi Nairiku, Japan (2008); (3) M_w 6.7 Northridge, USA (1994); (4) M_w 7.0 Haiti (2010); (5) M_w 7.6 Chi-Chi, Taiwan (1999); (6) M_w 7.9 Wenchuan, China (2008): (6a) reverse-slip segment, and (6b) strike-slip segment; (7) M_w 6.0 Umbria Marche, Italy (1997); (8) M_w 6.3 L'Aquila, Italy (2009); (9) M_w 5.6 Rotoehu, New Zealand (2004); (10) M_w 6.2 Mammoth Lakes, USA (1980); (11) M_w 6.7 Mid-Niigata Prefecture, Japan (2004); (12) M_w 6.9 Loma Prieta, USA (1989); (13) M_w 6.2 Aysén, Chile (2007); (14) M_w 7.9 Denali, Alaska, USA (2002); (15) M_w 6.8 Yushu, China (2010). See Supplementary Online Material (SOM) for data sources and quality check of the event inventories.

Likewise, ground motion associated with non-vertical faults is asymmetric with respect to fault-slip direction (Allen et al., 1998), producing distinctly different rupture dynamics than during strike-slip motion (Oglesby et al., 2000b; Ma, 2009). Yet how these varying rupture and slip dynamics due to fault type and

geometry affect the spatial distribution of coseismic slope instability, for example through significant hanging-wall shattering (Abrahamson and Somerville, 1996), remains unknown. More than a dozen substantially complete landslide inventories throughout the world reveal that fault type and geometry strongly influence the number of coseismic slope failures triggered (Figure 5.1, Table A3 in appendix). In particular, surface ruptures of thrust and reverse faults have triggered many more landslides than those of strike-slip faults, and even less on normal faults. Here we test the hypothesis that distinct faulting styles modulate both the abundance and spatial patterns of earthquake-induced landslides.

5.2 Materials and Methods

5.2.1 Fault Geometry and Coseismic Landslides

We compiled data on fault-dip angles and rupture mechanisms together with the total number of coseismic landslides from thirteen substantially complete inventories (Table A3 in appendix). For regional-scale analysis of the 2008 Wenchuan earthquake, we combined two sets of GPS-based measurements of coseismic offsets (Xu et al., 2009; Liu-Zeng et al., 2009), eliminating spatial data overlaps of <25 m. We used moment tensor solutions of the earthquake and the distribution of sub-events, their mechanisms, and their time relative to the initial origin times (Zhao et al., 2009) based on long-period waveform data from 39 worldwide stations; and models of coseismic fault geometry and slip in the hanging wall of the YBF (Figure 5.2) from inverted GPS and InSAR data (Shen et al., 2009).

5.2.2 Landslide Inventory

To investigate the effect of fault rupture on coseismic landslide patterns in the 2008 Wenchuan earthquake, we compiled a georeferenced database of landslides mapped by visual interpretation of 26 pre-earthquake false-color composites of multispectral (15-m ASTER, and 10-m ALOS AVNIR-2), and panchromatic (2.5-m ALOS PRISM, and 2.5-m Cartosat-1) satellite scenes, and compared these to 32 post-earthquake satellite images (2.5-m SPOT-5, and 2.5-m IKONOS). For scale consistency, we digitally mapped at 1:10,000 scale on-screen. We also included sub-samples of landslides from existing inventories (Dai et al., 2011; Gorum et al., 2011) in order to account for the effects of cloud cover or spatial coverage.

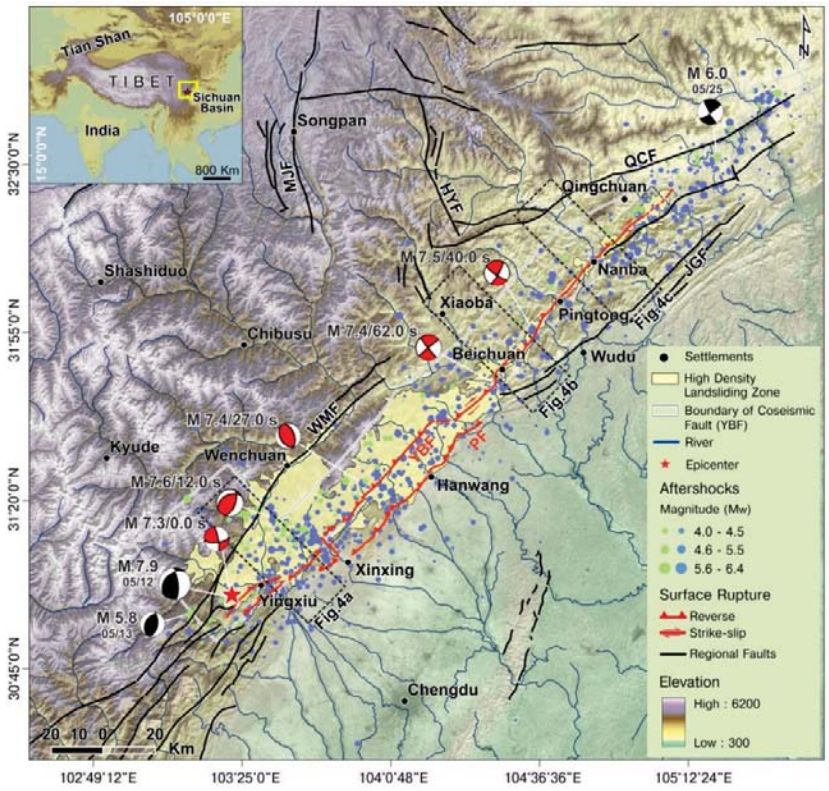

Figure 5.2 Tectonic setting of the Wenchuan earthquake. Red lines indicate surface traces of coseismic rupture (Xu et al., 2009); focal mechanism of the main shock (05/12/2008) and two of the major aftershocks (05/13 and 05/25) are shown in black and white (United States Geological Survey; http://earthquake.usgs.gov), including moment tensor solutions of the earthquake and the distribution of sub-events (Zhao et al., 2010; red and white beach balls), their mechanism and their time relative to the initial origin times. Green and blue dots show the aftershock distribution from United States Geological Survey (USGS) and China Earthquake Administration (CEA), respectively. Region of high landslide area density delimited by 0.08 density contour. Dashed rectangles are locations of transverse swath profiles (Figure 5.6). WMF: Wenchuan-Maowen fault; YBF: Yingxiu-Beichuan fault; PF: Pengguan fault; JGF: Jiangyou-Guanxian fault; QCF: Qingchuan fault; HYF: Huya fault; MJF: Minjian fault.

Contrasts between pre- and post-earthquake images allowed us to single out 3,120 pre-earthquake landslides with no observable earthquake trigger, while attributing 60,574 landslides to the Wenchuan earthquake. We conducted fieldwork in May–June 2009 and April–May 2010 in selected areas near Wenchuan, Yingxiu, Beichuan, Nanba, and Qingchuan for detailed ground trothing (Figure 5.2). We calculated landslide density in a moving window of 1-km radius using a kernel density with a non-parametric density estimator, and normalized density by maximum values. Local relief, defined here as the

maximum elevation range in a 1-km radius moving window, and local slope gradient, defined here as a polynomial plane fitted to the direction of maximum hillslope gradient, were extracted from a 30-m resolution digital elevation model based on the spatial interpolation of contour lines digitized at 20-m equidistance.

5.2.3 Lithologic controls on coseismic landslide occurrence along Yingxiu-Beichuan fault (YBF)

In order to explore lithologic controls that could potentially outweigh the observed relationship between the pattern of coseismic landslides and the dynamic rupture process, we selected two test lithological units that are uniform and comparable, though adjacent to different fault geometries within the hanging wall of YBF (Figure 5.3 and Table 5.1). These lithological units show the highest coseismic landslide density and were considered to be among the most susceptible to slope failure within the region (Chigira et al., 2010; Dai et al., 2011): (i) Cambrian sandstone and mudstone (Cs1-Cs3, Figure 5.3). We selected from these units two patches from segments dominated by strike- and oblique-slip surface rupture, and one patch from the segment where coseismic thrust motion prevailed. These patches are located on the ruptured hanging wall and follow the trace of the surface rupture. (ii) Proterozoic granitic rocks (G1-G3, Figure 5.3). The only granitic body in the region crops out in the strike-slip segment of the surface rupture, >7.2 km away from the surface rupture (Table 5.1). To maintain consistency, we chose two patches of granitic rocks in the thrust-dominated segment of the YBF at a comparable distance, cropping the southeastern boundary of these patches located <7.2 km of the fault. These patches are defined by lithological contacts and major faults such as the hanging wall boundary of the YBF. To normalize landslide occurrence for the outcrop area, we derived the frequency ratio for each lithological unit by calculating the fraction of terrain with and without landslides in these lithological units (Table 5.1).

Table 5.1 Exposure areas, distance to surface rupture, coseismic landslide areas and frequencies for selected lithological units in different surface rupture geometries.

	Lithology	Fault Type	Number of landslides	Landslide area (km2)	(%)	Exposure area (km2)	(%)	Frequency ratio	Distance to Surface Rupture (km)			Terrain slope (°)		Local relief (m)	
									Min.	Max.	Mean	Mean	Std. Dev.	Mean	Std. Dev.
Sandstone (Cambrian)	Cs1	Thrust	1071	12.90	32.49	45.35	21.94	1.48	0.00	15.35	7.68	28.29	10.64	561.83	125.30
	Cs2	Oblique-slip	1418	18.05	45.47	69.76	33.75	1.35	0.00	5.10	2.55	27.50	11.69	510.73	115.69
	Cs3	Strike-slip	591	8.75	22.04	91.61	44.32	0.50	0.00	8.67	4.34	23.65	11.00	401.08	94.44
Granite (M.Proterozoic)	G1	Thrust	1983	51.90	82.58	240.86	73.55	1.12	7.20	15.91	11.56	32.38	10.67	676.16	157.80
	G2	Thrust	463	9.91	15.77	48.40	14.78	1.07	7.20	13.83	10.52	34.88	11.63	737.44	158.06
	G3	Strike-slip	132	1.04	1.65	38.20	11.67	0.14	7.20	13.23	10.22	30.06	10.20	575.84	106.63

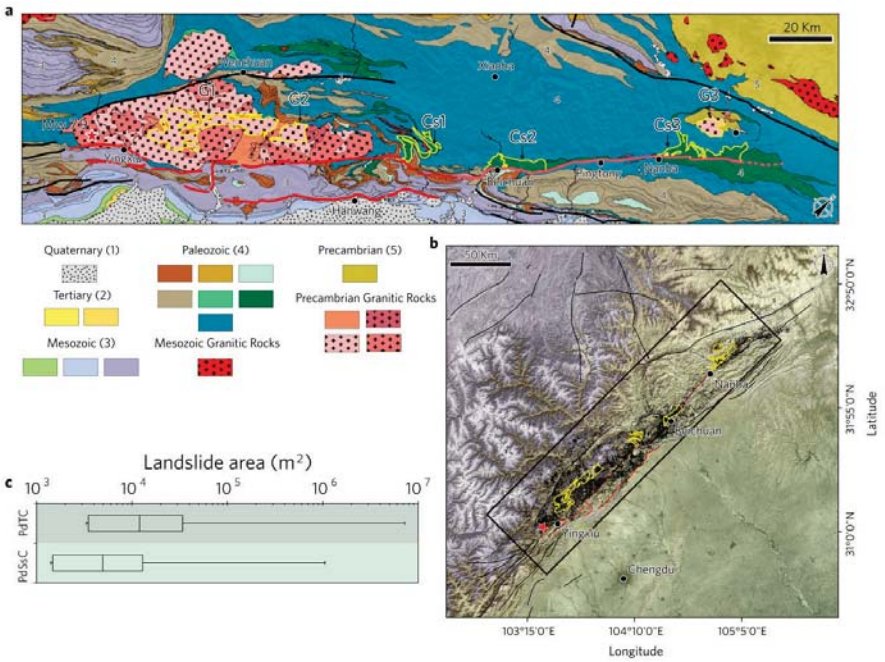

Figure 5.3 Location and size distribution of coseismic landslides in selected uniform lithologies, in the Wenchuan area. **a**, Geological map of the Longmen Shan thrust zone and the locations of selected roughly uniform lithologies; yellow lines delimit selected patches within these units. The star is the epicenter obtained from U.S. Geological Survey (http://earthquakes.usgs.gov). Dark and light red lines indicate surface traces of predominantly thrust and dextral segments of the coseismic rupture, respectively (*14*; see Table S2 for comparison of uniform lithologies). **b,** Distribution of 60,574 landslides triggered by Wenchuan earthquake. Black rectangle inset and yellow polygons show location of inset *a*, and selected uniform lithologies, respectively. **c,** Box-whisker plot of landslide size distribution expressed as planform landslide area [m^2] stratified by predominant fault slip components along the YBF shows that landslide size on average tends to decay away from the epicenter; PdSsC: predominant strike-slope component; PdTC: predominant thrust component.

5.3 Results

We analyzed landslides triggered by the 2008 Wenchuan (M_w 7.9) earthquake along the Yingxiu-Beichuan fault (YBF), where two distinct types of faulting mechanisms (Xu et al., 2009; Liu-Zeng et al., 2009) occurred over a rupture length of 240 km (Figure 5.2).

The dominant style of faulting along the YBF, from its southern to northern parts with reference to Beichuan city, changes from reverse to strike-slip (Xu et al., 2009; Liu-Zeng et al., 2009; Zhao et al., 2010; Wang et al., 2010; Shen et al., 2009; Du et al., 2009). The differing properties of the YBF fault segments

allow us to examine if and to what degree differences in fault type and geometry affect the spatial pattern and extent of landslides. For this purpose we mapped 60,574 landslides, mostly rock falls, rock avalanches, and rock-debris slides, through a systematic comparison of pre-and post-earthquake satellite images.

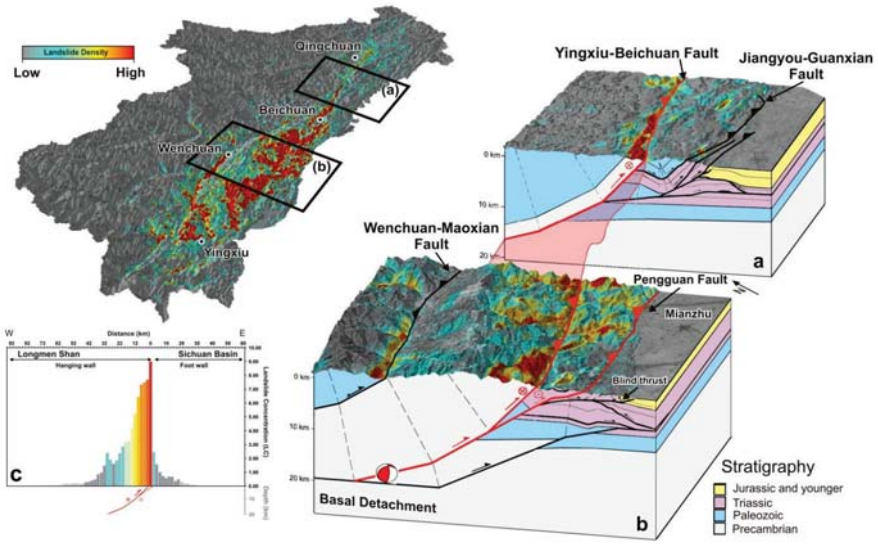

Figure 5.4 Asymmetric distributions of coseismic landslides as regional-scale evidence of hanging-wall shattering in the Longmen Shan fault zone. a, Block diagram of strike-slip segment, and b, reverse-slip segment. Landslide point density [km^{-2}] superimposed on data by Xu et al. (2009). **c,** Histogram of landslide point density across the entire Longmen Shan fault zone. Note significant increases in landslide density in hanging walls of the Yingxiu-Beichuan and the Wenchuan-Maoxian Fault zones.

Our mapping reveals that coseismic landslides occurred mostly in a 17-km wide corridor along the southwestern YBF. This landslide belt narrows to ~10 km in the mid-portions of the fault zone, and ~3.5 km along the northeastern segment. Landslide densities expressed as the number of landslides per unit area [km^{-2}], and the fraction of the terrain affected [%] within a 20-km wide swath profile along the surface rupture vary strongly both with distance along the YBF and with the dominant fault-slip geometries (Figures 5.4 and 5.5).

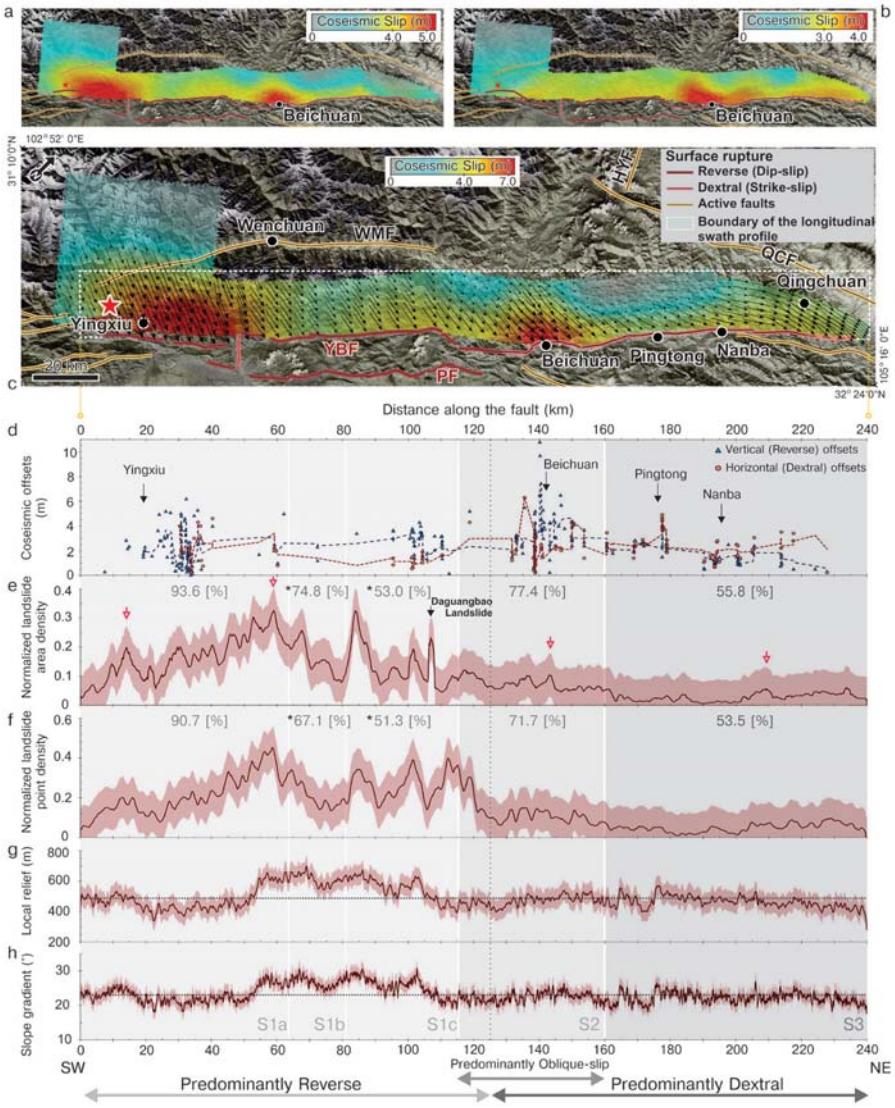

Figure 5.5† Along-strike distributions of coseismic slip, landslide density, and topography in hanging wall of the Yingxiu-Beichuan Fault (YBF) zone. **a**, **b**, Vertical (reverse) and horizontal (dextral) slip amplitudes (Shen et al., 2009). **c**, Coseismic slip distribution (Shen et al., 2009). Black arrows are slip vectors on fault patches (Shen et al., 2009), with amplitudes denoted by coseismic slip rate. Dashed rectangles locate longitudinal swath profiles (e-h). **d,** Combined coseismic offset measurements along the YBF rupture (Xu et al., 2009; Liu-Zeng et al., 2009). Blue and red dashed lines are 5-km running mean of vertical and horizontal offsets, respectively. **e-h,** Swath profiles (20 km × 240 km) of coseismic landslide density, local relief and slope gradient, respectively. Black lines and red shading are means and ± 1 st. dev. per 60-m bins.

Fault segments with prevalent thrusting and vertical coseismic offsets of up to 4 m display the highest overall landslide density (S1a and S1c). Local lows of landslide density are consistent with lower vertical coseismic offsets (S1b). Segments with dominant oblique-slip around Beichuan city (S2) and growing horizontal coseismic offsets show a sharp decrease in landslide density. The dextral strike-slip segment (S3) has the lowest landslide density with only minor peaks towards the northeastern end of the surface rupture.

These along-strike changes in landslide density are only faintly mirrored in metrics of terrain steepness such as mean local relief or slope gradient. Sub-sections S2 and S3 have mean local relief and slope gradients comparable to S1a, although they show a much lower landslide density. Moreover, despite local deviations in S1b and S1c, mean slope gradients remain constant despite distinctive changes in landslide density.

In terms of lithological controls, we noted that the frequency ratio of landslides in Cambrian sandstone is higher in Cs1 in the thrust-dominated segment of the surface rupture than in Cs3 in the strike-slip dominated segment (Table 5.1). Differences in the frequency ratios in Proterozoic granitic rocks are somewhat higher. We observe a significant covariance between the mean slope angles and local relief values in these uniform lithological units, and the landslide frequency ratio is evidently higher in the lithological units within the predominantly thrust segment. Also, the density of coseismic landslides in the predominantly thrust component is nearly twice that of the one in the strike-slip component. Landslide density decreases in comparably uniform granitic lithology throughout various parts of the hanging wall of the YBF in spite of high local relief and high slope gradients. Although landslide density is much lower in mechanically weaker schists and sandstones, it also decreases consistently with coseismic deformation independent of minute changes in topography (Figure 5.3). We infer that landslide density varies more with the amount of coseismic fault offsets than it does with topography or lithology.

The majority of slope failures occur both within <45° of the mean azimuth of the surface rupture (Figure 5.6 (red arrow in rose diagram inset)), and the southwestern fault segments dominated by reverse and oblique slip. Landslide density decreases by more than an order of magnitude beyond these areas, and

† **(Figure 5.5 cont.)** Black arrow shows location of the Daguangbao rock slide (8.4×10^8 m^3), i.e. the largest triggered by the Wenchuan earthquake. Light and dark grey boxes delimit sub-sections of differing dominant fault geometries. Red arrows are local peaks in landslide density coinciding with fault-zone asperities.

quantitatively augments previous estimates (Chigira et al., 2010; Gorum and van Westen, 2010; Ouimet, 2010). Contrary to traditional model predictions, the degree of symmetry with which landslide density decays away from the YBF decisively changes along strike and largely as function of the fault-dip angle and the ratio of vertical to horizontal coseismic offsets along the rupture (Zhao et al., 2010; Wang et al., 2010; Shen et al., 2009; Figure 5.7).

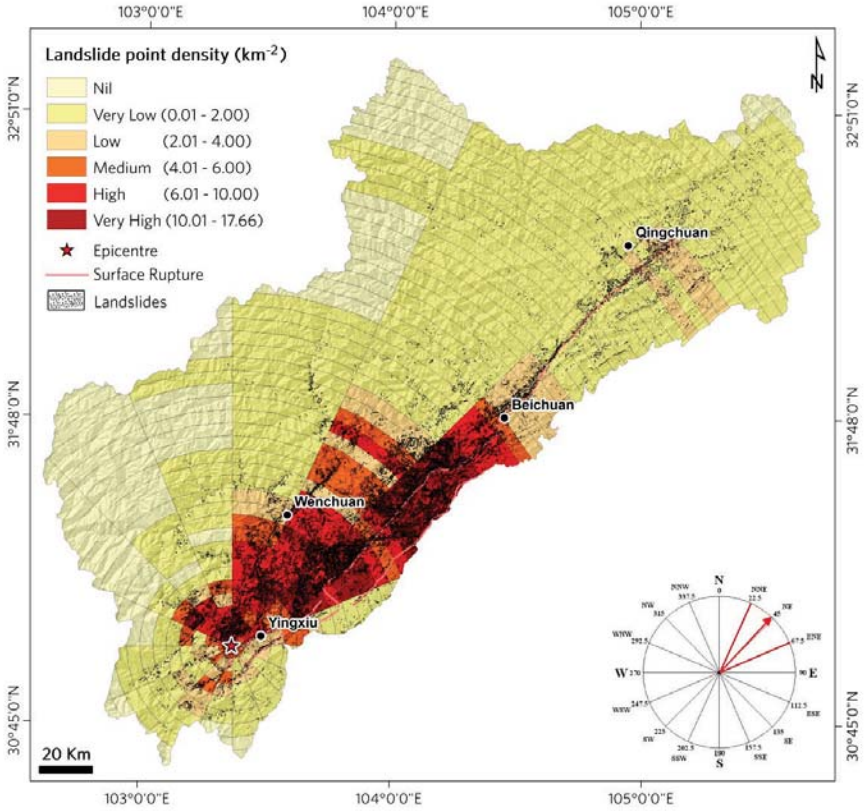

Figure 5.6 Directivity analyses of 60,574 landslides triggered by the 2008 Wenchuan M_w 7.9 earthquake, China. Landslide abundance expressed as point density [km^{-2}] shows a distinct sub-parallel clustering with respect to the ruptured Yingxiu-Beichuan fault (YBF).

The average dip angle of the YBF along three equal-area transverse swath profiles increases along strike in a northeasterly direction. In the southwestern part, coseismic offsets are much larger in the vertical than in the horizontal and the average fault dip angle is 43°.

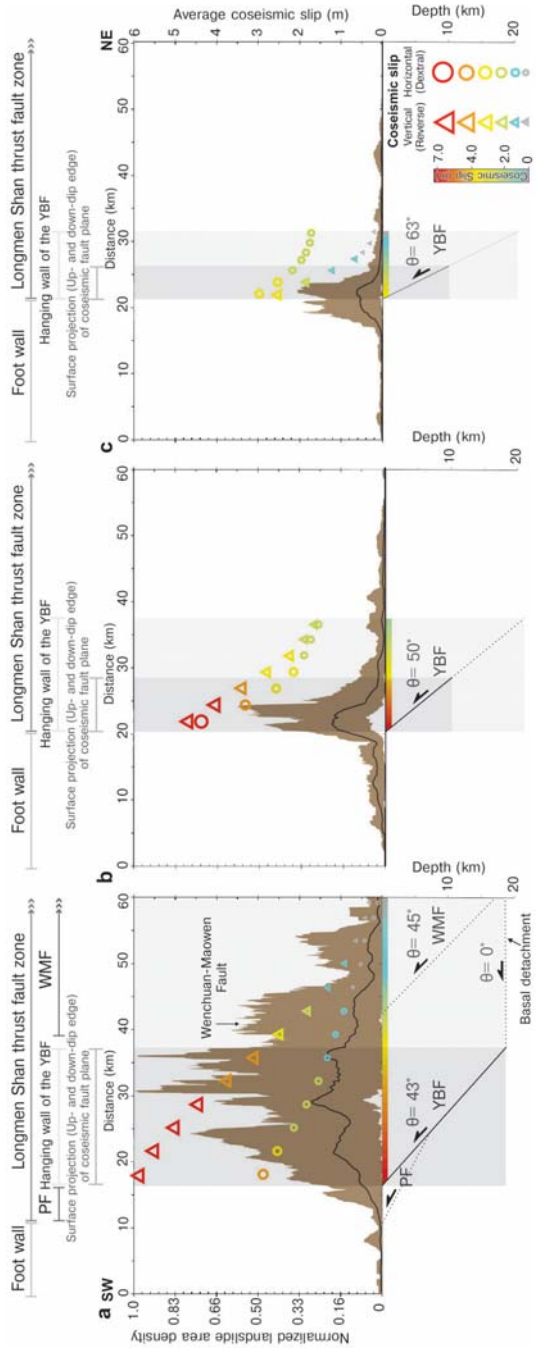

Figure 5.7 Fault geometry and landslide density along transverse swath profiles of three asperities (areas of peak slip) across the Longmen Shan thrust fault zone. **a**, Yingxiu; **b**, Beichuan; and **c**, Nanba (Figure 5.2). Thick black line and brown shading are mean, minimum, and maximum normalized coseismic landslide densities, respectively, computed for 60-m bins. Thin dashed and thick black lines are ruptured fault sections inferred from inversion of GPS-InSAR data (Shen et al., 2009) and kinematic models (Zhao et al., 2010; Wang et al., 2010), respectively; light and dark grey boxes show fault-rupture projections onto ground surface, respectively. Rupture depth is ~10 km in Beichuan and Nanba swaths, and thus shallower than in the Yingxiu (SW) "*geometric barrier*" (Shen et al., 2009). Thin grey dashed lines are Wenchuan-Maowen (WMF) and Pengguan faults (PF). Horizontal color bars show modeled coseismic slip rates (Shen et al., 2009) per swath.

In the central part of the hanging wall of the YBF, vertical offsets are slightly higher than horizontal, and the average dip angle is 50°. In the northeastern part, horizontal offsets dominate, and the average fault-dip angle of 63°. The distinct clustering of landslides on the hanging wall along thrust segments of the YBF provides the first quantitatively robust geomorphic evidence of hanging-wall shattering, introducing spatial asymmetries in landslide response along thrust faults, and compromising classic susceptibility models of coseismic landslide occurrence (Figures 5.4 and 5.7).

In contrast, landslides are nearly symmetrical across strike-slip segments of the YBF, fitting the conventional model of earthquake triggered landslide patterns (Meunier et al., 2007; Keefer, 2000). This along-strike contrast in the spatial pattern of coseismic landslides can be explained by differing fault geometries (i.e., non-vertical dips) along the rupture in the southwestern and central parts of the YBF, which caused highly asymmetric ground motions in the hanging wall and footwall parts of the fault (Figure 5.7). In contrast, the near symmetry of fault geometries (i.e., near-vertical dips) in the northeastern part of the YBF caused more symmetric ground motions on either side of the fault.

5.4 Discussion and Conclusions

The regional variation in landslide density closely coincides with the principal stress field orientations (Duan, 2010) between the thrust, oblique-slip, and strike-slip zones of the hanging wall of the YBF. These variations in fault style and geometry have in turn affected the rupture propagation, causing notable contrasts in fault and ground motion on the hanging wall of the YBF (Zhao et al., 2010). The rupture lasted 105 seconds and featured three stages (Zhao et al., 2010). In the first stage (t = 0-12 s), the rupture initiated near the hypocenter and released 3% of the total seismic moment. In the second stage from (t = 12-45 s), the rupture released 60% of the total seismic moment with very high velocity in the mainly dip-slip sections of the YBF. In the last stage (t = 45-105 s), the rupture released 37% of the total seismic moment in the mainly strike-slip section of the YBF (Zhao et al., 2010). While step-over bends may have caused local changes in faulting styles, variations in the principal stress field orientations prior to the earthquake likely played a dominant role in modulating fault styles (Duan, 2010), judging from evidence from the long northeast-trending Qingchuan fault segment north of the YBF; active fault slickensides (Du et al., 2009); and kinematic models (Zhao et al., 2010; Wang et al., 2010; Shen et al., 2009). Different pre-earthquake faulting styles were also inferred

independently from the pattern of rock-uplift rates (Kirby et al., 2003). A secular block-motion model (Shen et al., 2009) derived from GPS velocity data further suggests the existence of two different blocks in the southwest and the northeast of Longmen Shan fault system, with the Beichuan area forming a transition zone between them. Hence, most of the along-strike differences in mean local relief likely result from higher long-term uplift rates along the southwestern segments of the Longmen Shan fault zone. While the faulting styles and geometries of the surface rupture associated with the Wenchuan earthquake are similar to pre-earthquake characteristics of the Longmen Shan thrust fault zone, the three areas of peak coseismic slip near Yingxiu, Beichuan, and Nanba correspond to major "*geometric barriers*" (Shen et al., 2009) or fault asperities where fatalities, damage, and local landslide density were highest.

In summary, our results lend strong support to the notion that the distribution of landslides triggered by the Wenchuan earthquake is controlled by fault type and coseismic slip rates rather than earthquake magnitude or epicenter distance alone. Topography and lithology play subordinate roles, implying that variations in rock type or relief are insufficient to explain the pattern of coseismic landslides along fault segments with distinctly different rupture styles. Changes in fault geometry and inherent strain release may significantly distort the spatial pattern of coseismic landslide occurrence by imposing significant asymmetry. Furthermore, the distinct asymmetric coseismic landslide pattern underlines the rupture dynamics characterized by unilateral propagation, and helps refine conventional models based on bilateral propagation resulting in a symmetric decay of landslide abundance from the epicenter and fault rupture. Our results further support the observation from global data that thrust/reverse faults induce more coseismic landslides than normal and strike-slip faults, even if occurring on segments along a single main fault (Figure 5.1). Coseismic landslide abundance and spatial asymmetry decrease with increasing dip angle of normal and strike-slip faults, whereas the number of coseismic landslides increases with a decrease in dip angle for thrust and reverse faults for a given magnitude. Detailed mapping of coseismic landslide density closely mimic variations in fault slip rates and geometries. Given that lithology and topography play subordinate roles on earthquake-induced slope failure, landslide maps may serve as a valuable tool for recording fault rupture dynamics, propagation, and the location of major asperities through surface process response. Our results call for modifications to existing models of earthquake triggered landslide susceptibility solely based on empirical relationships, particularly in fault segments vulnerable to strong

hanging-wall shattering. The common expectation that the abundance of coseismic landslides decays systematically away from the ruptured master fault requires careful reappraisal given the possibility of more complex rupture dynamics that may involve stress propagation along different fault segments.

6 Synthesis

6.1 Introduction

The principal goal of most regional landslide susceptibility and hazard studies is to determine the spatial and temporal probability of landslide occurrences. Such maps are important tools for reducing casualties and economic losses as they form the basis for sustainable planning and land-use policies. In order to better predict the distribution of earthquake-induced landslides it is of essential importance to study their distribution caused by historical earthquakes, and correlate these with possible causal factors, which can then be used in generating more reliable earthquake-induced landslide susceptibility maps. Apart from the geo-environmental factors, the characteristics of the triggering earthquake are also important for understanding the spatial probability of landslides. Due to the lack of sufficient earthquake-induced landslide inventories the research on coseismic landslide susceptibility has less progressed in comparison to other natural triggers. This is also caused by less clearly defined understanding of the contribution of earthquake dynamics to coseismic landsliding. In this respect, the objective of this thesis was to contribute to the current state of coseismic landslide knowledge in a global context by exploring the role of earthquake rupture dynamics, faulting styles, topography and rock-types on the location, size, and density pattern of coseismic landslides in different seismo-tectonic and geomorphic environments. In this chapter, the findings of the previous Chapters 2 to 5 are summarized and the results are discussed in relation to the original research objectives which were defined as:

- to evaluate the effect of the type of faulting and fault geometry on the coseismic landslide distribution characteristics (section 6.3).
- to assess whether the spatial pattern of coseismic landslides differs between blind and surface-rupturing earthquakes (section 6.4).
- to determine and to further characterize the potential control of coseismic slip rate and mode together with the differences in rock-type and geomorphic characteristics, on the density of landslides along seismogenic faults (section 6.5).
- to develop a conceptual model on the basis of the results presented in this study, which may bring new perspectives to the field of earthquake triggered landslide studies (section 6.6).

Each of the following sections discusses the achievements obtained for these objectives and summarizes the results of the case studies within a conceptual model. The final section outlines the limitations and further scope of research on earthquake triggered landslides.

6.2 Overview of spatial pattern and size distribution of coseismic landslides

The event-based inventory mapping is the first and principal step for analyzing the spatial pattern of coseismic landslides. In general, an event-based inventory map shows all the slope failures triggered by a single event. These inventories are mostly prepared by interpreting large to medium scale satellite images and/or aerial photographs taken shortly after the triggering event with the corroborative field surveys. The steps and the guidelines followed for mapping the individual landslides in this thesis are described in chapter 2. The main requirements for a relatively well-established event-based inventory are the identification of individual landslides and the coverage of the geographic area affected by the event as complete as possible. Also, the mapping of the individual landslides prevents a possible overestimation that may arise for the size-frequency distribution relation of landslides. The inventories were made using image interpretation of a large set of pre-and post-earthquake satellite images and airphotos. Unfortunately, landslides could only be verified during one fieldwork period which was carried out in the 2008 Wenchuan earthquake struck region. In other study areas, the corroborative information for the area and the landslides were obtained by oblique-aerial photos taken from observation aircrafts shortly after the events. To avoid the inclusion of pre-earthquake landslides, pre- and post-event remote sensing images were compared during the image interpretation. Although there have been efforts to define the essentials of the coseismic landslide mapping (e.g. Harp et al., 2011), there is still not a widely agreed mapping protocol for landslides. Therefore, the quality of many existing inventories remains problematic. Moreover, it is striking to note that about 90% of all the existing coseismic event-inventories have been produced by only using the post-earthquake images. We revealed that a coseismic landslide inventory based solely on post-earthquake images would substantially increase the fraction of area that is considered to be affected by slope failures and leads to anomalies in the landslide distribution (chapter 4). For example, the mapping of coseismic landslides triggered by the 2010 Haiti M_w 7.0 earthquake (chapter 4) clearly showed that there were 700 pre-existing

aseismic landslides which were not re-activated during the earthquake. On the other hand, the comparison of pre- and post-event conditions for coseismic inventory mapping of the Haiti earthquake revealed that 572 out of 1273 aseismic landslides were re-activated during the earthquake. Therefore, we can conclude that such a comparison helps to understand better the net coseismic landslide production. According to the other inventories that were produced within the context of this thesis, there were 5%, 1% and ~6% pre-existing landslides identified for the 2002 Denali Fault, 2007 Aysen and 2008 Wenchuan event-inventories, respectively.

In various parts of the thesis, the spatial distribution of coseismic landslides was assessed for different types of faults to reveal their direct relations with seismic, topographic and lithologic factors, along with an analysis of the landslide patterns density maps. These density maps were used in analyzing the regional coseismic landslide pattern and the relation of this pattern with the seismic and geo-environmental factors. The spatial patterns of coseismic landslides were computed using a Gaussian kernel density estimator both for the number density (number of landslides per square kilometer) and the area density (the fraction of area affected by landslides). An optimal moving window with 1-km radius size was determined for the density estimations of the eight event-inventories used in the study. We found that, especially for the events that had relatively small-sized landslides such as the ones triggered by M_w 6.8 Yushu (2010) and M_w 7.0 Haiti (2010) earthquakes, increasing of the radius size over 1-km caused distortions in the assessment of spatial patterns. Number and area based landslide densities were compared for their appropriateness and robustness in characterizing the landslide spatial pattern. The comparison was conducted using the two extreme example events (Figure 6.1) in terms of coseismic landslides size (i.e. M_w 6.8 Yushu (2010) and M_w 7.9 Denali Fault (2002) earthquakes) considering different sampling radius (R) sizes. The most abundant size of landslides triggered by these two earthquakes differ nearly two-orders of magnitude. According to the comparison it was revealed that the linear correlation between the number and area-based landslide densities was much higher in the case of Yushu earthquake that had smaller-sized coseismic landslides than the Denali Fault earthquake (Figure 6.2).

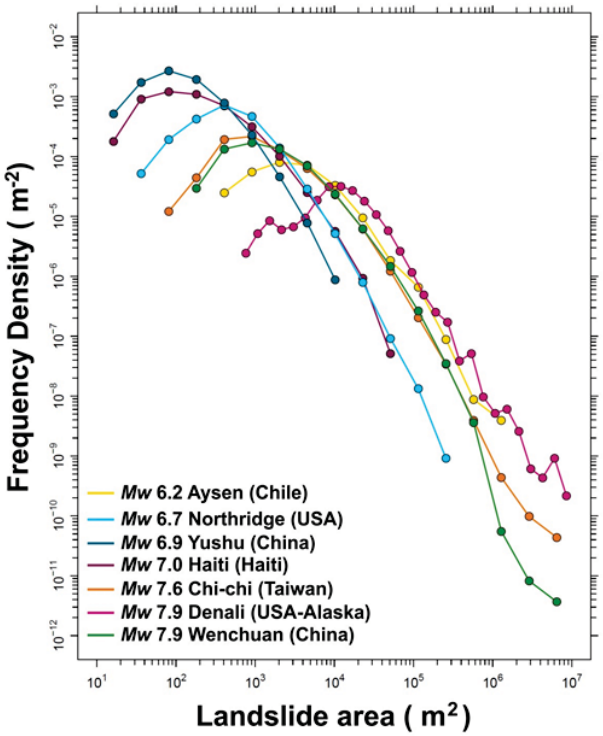

Figure 6.1 Frequency-size distributions of log-binned landslide deposit areas for different faulting earthquakes.

For both of the cases, the correlation coefficient between the number and area based landslide densities increased with increasing R values (Figure 6.2). On the contrary, the increasing sizes of coseismic landslide had a decreasing effect on the correlation between the number and area based landslide densities. Additionally, the distance between the individual landslides and the abundance are other factors that explicitly decrease the correlation. In this respect, although the difference between the landslide number and the areal density maps was small in the earthquake events that had relatively smaller landslide sizes, we can conclude that polygon-based landslide inventories (with areal information) are required for ensuring the robustness of the results. Therefore future earthquake-induced landslide inventories should be made as polygon maps, with classification of the landslide types, and subdivision of the scarp and accumulation areas. This is more work for the interpreters, especially when the interpretation should also be done using stereo-image interpretation and using both pre-and post-earthquake images. In practice there are very few inventories that have been made in this way. In order to speed up the process it would also

be very relevant to further develop algorithms for object-oriented image classification that would allow to extract the landslide polygons in a semi-automated way (Martha, 2011), followed by a phase where interpreters check these polygons using digital stereo image interpretation.

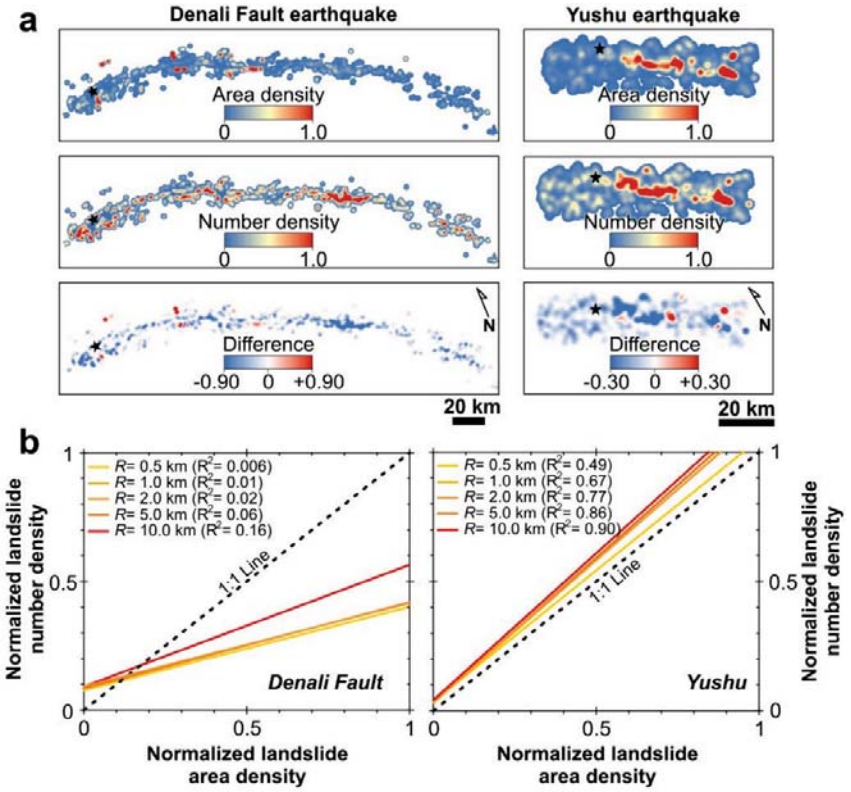

Figure 6.2 Spatial landslide density map comparisons of the M_w 7.9 Denali Fault (2002) and M_w 6.8 Yushu (2010) earthquakes. (a) Number density, area density and difference of landslide density maps within a moving window of 1-km radius using a Gaussian kernel density estimator, and normalized density by maximum values. Black star denotes epicenter. (b) Number and area density relationships of landslides triggered by the M_w 7.9 Denali Fault (2002) and M_w 6.8 Yushu (2010) earthquakes in different sampling radius (R).

6.3 Controls of type of faulting and fault geometry on the coseismic landslide distribution characteristics

Many previous works related to the occurrence and distribution characteristics of earthquake triggered landslides (e.g., Lin and Tung, 2003; Lee and Evangelista, 2006; Chang et al., 2007; Kamp et al., 2008; Lee et al., 2008;

Pareek et al., 2010; Su et al., 2010) have used the distance to (or from) faults as a spatial predictor, regardless of either orientation and/or style-of-faulting (strike-slip, dip-slip or oblique-slip). Implicit in this practice is the notion that every fault has equal influence on the likelihood of landslide occurrence. However, recently, much seismological research has focused on the investigation of different faulting mechanisms on the fault rupture dynamics. In this respect, there are both observational and theoretical arguments that the dynamics of faults with asymmetrical geometry (e.g. dip-slip faults) are both qualitatively and quantitatively different from those of symmetrical faults (e.g. strike-slip faults) (Oglesby et al., 2000a and 2000b; Ma 2009). There is observational evidence that the symmetry of ground motion with respect to fault-slip direction is lost when a fault does not have a vertical dip (Abrahamson and Somerville, 1996). Likewise, ground motion associated with non-vertical faults is asymmetric with respect to fault-slip direction which is also not currently incorporated in any known attenuation relation (Allen et al., 1998), and producing distinctly different rupture dynamics than during strike-slip motion (Oglesby et al., 2000b; Ma, 2009).

In the light of the recent seismological achievements, the controls of faulting types and fault geometries on the coseismic landslide distribution characteristics were evaluated for similar faulting mechanisms in chapter 3 and 4. In addition, in chapter 5, different types of faulting and fault geometries were compared both at global and regional scale. Combining the results of chapters 3-5 we found that the abundance and the spatial distribution of coseismic landslides strongly vary with faulting styles. Moreover, the observation from global data shows that thrust/reverse faults induce more coseismic landslides than normal and strike-slip faults, even if occurring on segments along a single main fault (Figure 5.1). More specifically, for regional scale case events (c.f. chapters 3-5), we revealed that the spatial distributions of landslides were nearly symmetrical across strike-slip segments while the landslides were concentrated asymmetrically on the hanging wall sections in the thrust/reverse segments. In chapter 3 and 5, the control of the fault geometry on the abundance and the density of coseismic landslides were also investigated. It was concluded that fault geometry is a key control on the spatial distribution pattern of the landslides. Furthermore, the clustering of 70-85% of the landslides triggered by intermediate- and large-sized earthquakes (e.g. Wenchuan, Denali Fault, Chi-chi and Yushu earthquakes) over the surface projection (up- and down-dip edge) of the earthquake generating fault supports this observation. In this respect, coseismic landslide abundance and the spatial asymmetry decrease with

increasing dip angle of strike-slip faults, whereas the number and the overall area affected by the coseismic landslides increases with a decrease in dip angle for thrust and reverse faults for a given magnitude. These results further suggest that the future work on the coseismic landslides should consider the faulting styles and fault geometry. Such a consideration will enable a better understanding of the distribution of the coseismic landslides and will increase the prediction capacity for the coseismic susceptibility mapping.

6.4 Blind rupture earthquakes and distribution pattern of coseismic landslides

In general, large earthquakes break the surface, however small earthquakes usually do not (Wells and Coppersmith, 1994). Over one-half of the earthquakes in the magnitude range of 6.0 to 6.5 do not have surface ruptures. This fraction decreases to about one-third for the magnitude range of 6.5 to 7, and about one-fifth of the earthquakes in the magnitude range of 7.0 to 7.5 (Lettis et al, 1997). Latest ground-motion observations suggest that there is a considerable difference in surface-rupturing earthquakes and earthquakes due to buried faults (Abrahamson and Silva, 2008; Hussain and Kumar, 2013). The seismic energy during surface-rupture earthquakes focuses more to the surface, and a significant increase in the static stress drop in terms of mean displacement may cause more coseismic landslides near the fault. Additionally, shear stress increases near the coseismic fault during surface-rupture earthquakes, depending on the width of the deformation zone and the coseismic slip amplitude (King et al., 1994; Harris, 1998; Stein, 1999). Wada and Goto (2012) explained this phenomenon by the difference in the locations of the asperities (areas of peak coseismic slip) of surface- and blind-ruptured earthquakes. Asperities for surface rupture earthquakes are located in regions shallower than 5 km, while they are located deeper than about 5 km in blind rupture earthquakes (Wada and Goto, 2012). Although the locations of asperities are different for surface and buried faults, they are similar in terms of their relative positions from the hypocenter. The location of the hypocenter is close to and beneath the asperities, thus the hypocenter of most earthquakes is located within a region of asperities or very close to one (Mai et al., 2005). Moreover, the attenuation relation for peak ground acceleration (PGA) on rock-site conditions considering the hanging wall scaling, shows a step in the ground motion from the hanging wall to the foot wall for surface-rupture earthquakes (Abrahamson and Silva, 2008). The difference in ground motion between hanging walls and

foot walls is more pronounced for surface rupture-earthquakes, with the ground motion focusing on the hanging wall. However, for the case of blind-rupture earthquakes the transition of the ground motion proportion between the hanging wall and the foot wall is smooth, although the ground motion ratio remains higher on the hanging wall (Abrahamson and Silva, 2008).

The results from chapter 4, where landslides triggered by surface- and blind-ruptured earthquakes were compared, supported the distribution pattern obtained from recent seismological observations. In this respect, the comparison of coseismic landslide inventories indicates that blind rupture-earthquakes induced fewer landslides than surface rupture-earthquakes on thrust or reverse faults (Figure 4.9). The number of coseismic landslides appears to be mainly controlled by earthquake magnitude rather than by whether the rupture breaks the surface or not (Figure 4.9). Yet mass-wasting responses to earthquakes of similar magnitudes hanging-wall effect was more pronounced and the landslides were larger in surface-ruptured earthquakes in contrast to the blind-rupture earthquakes (Figures 4.9 and 4.10). Accordingly, in blind-ruptured earthquakes the distribution of landslides exhibits more symmetric pattern between the fault blocks though the fraction of the area remains higher on the hanging wall side. Furthermore, we showed that the hanging wall of the blind thrust-earthquakes are morphologically less expressed than those of the surface rupture-earthquakes, which may reflect that they are either recently established faults or simply older faults with rates of fault growth being outpaced by rates of erosion (Figure 4.9). Therefore, the relative impact of the topography cannot be neglected. Overall, the findings related with the second objective show that the landslides triggered by the surface- and blind rupture earthquakes, which are different in terms of earthquake seismology (e.g. the depths of asperities and the ground motion proportion between the fault blocks), are significantly different both in terms of distribution pattern and the fraction of area affected by these landslides. As a result, these findings provide new awareness on the earthquake triggered landslide studies and as such contribute to Earth sciences.

6.5 The role of rupture process, topography and lithology on coseismic landslide abundance and pattern

In general the thesis revealed that the fault line is a more trustworthy baseline than point-source measures (i.e. epicenter or hypocenter) to represent the seismogenic source for explaining the coseismic landslides pattern. Generally speaking, point-source distance measures such as epicentral or hypocentral

distance are poor measures for large earthquakes with prolonged ruptures. They are primarily used for characterizing small earthquakes that can be reasonably represented by a point source or for characterizing large earthquakes when the fault-rupture plane cannot be identified for past or future (simulation-based) earthquakes (Campbell, 2003). In this section, we evaluate the potential contributions of rupture process, topography and lithology, and their combined effect on the variations of landslide pattern along and around the fault.

The frictional strength along the fault plane is not uniform, thus overall displacement involves slip on one or more asperities, i.e. high-slip patches, where the friction is maximum (Hall-Wallace, 1998). In general, asperities are controlled by fault plane roughness, geometry and age of the fault zone in space and time. With a rough generalization we can state that there can be more asperities or high-slip patches along the fault rupture for earthquakes with M_w >7.0. Most of the energy released during earthquakes is tied to these asperities (Ruiz et al., 2010) and the depth of the asperities for surface rupture earthquakes are generally shallower than blind rupture earthquakes (Wada and Goto, 2012). In this respect, it cannot be expected that the coseismic landslide distribution stays uniform everywhere with distance from the fault line. In this research, the changes in the coseismic landslides pattern along the fault were analyzed in detail especially in chapters 3-5. The results of these chapters show that a strong variation of coseismic landslide abundance correlates with both rate and mode of the coseismic deformation, but also with the topography. Broadly speaking, step-like changes in the fraction of areas affected by landslides coincide with areas where coseismic deformation attained its maximum (Figures 3.11, 4.8 and 5.5). These areas of higher coseismic slip correspond to earthquake asperities and contain nearly 65 to 85% of the areas affected by the coseismic landslides, which further supports the notion of coseismic slip as an additional controlling parameter for landslide abundance. In addition, we revealed that the majority of the largest landslides triggered by the strong earthquakes studied in this thesis are located above the asperities. In terms of coseismic-slip mode, there was a remarkable increase in the abundance and the area affected by the landslides in the parts where the slip direction (rake) was normal to the surface rupture. This increasing tendency is generally higher near the fault and permanent coseismic vertical deformation areas along the rupture. Moreover, we show that there is a strong signal from landslide distribution patterns associated with the direction of rupture propagation. Coseismic landslide occurrence in the near field is consistent with the direction of rupture propagation (directivity) in many cases (i.e. M_w 7.9 Wenchuan and Denali Fault earthquakes), indicating that the

dominant direction of coseismic slip could have caused increasing ground-motion amplitudes towards to same direction where rupture propagated.

The effect of the rupture processes of the earthquake on coseismic landsliding is spatially modulated by the topographic and lithological characteristics along and around the surface rupture. Therefore, topography and lithology have a combined impact together with the rupture processes on the spatial- and size-distribution of landslides. Although the inter-comparisons of the earthquakes in terms of lithological variables were not so much meaningful at the regional scale, we still determined the lithological units that included the highest number of landslides using the global lithological classes proposed by Hartmann and Moosdorf (2012) for the available earthquake events (Figure 6.3). In this respect, the highest density of individual landslides was observed in carbonate sedimentary rocks (sc) and metamorphics (mt), while the highest areal density of landslides was observed in ice and glaciers (ig) and acid plutonic rocks (pa). However, such a lithological comparison was limited due to the fact that, in addition to the regional lithological differences, the lithological units were also different locally in terms of structural geological and geotechnical characteristics. As a result, any lithology that is determined as susceptible to landslides is valid for the specific case only, and it is difficult to make general conclusions based on such a limited number of inventories. Therefore, for a more reliable and generalized conclusion on such lithological comparisons, there is need for more event-based studies.

Although the earthquake mechanism, fault geometry and earthquake rupture process are the dominant controlling factors on the coseismic landslide pattern the topography is obviously also an important factors. Mass movements are controlled by gravity and therefore slope steepness and internal relief are crucial factors. In addition, terrain ruggedness was used as an additional metric in some parts of the study. Comparison results of the different events showed that local relief and hillslope gradient have a nonlinear relationship with landslide density. In most of the events we found that landslide density increases in a roughly linear fashion with both local relief and hillslope gradient but then increases rapidly near the common modes of the local relief and hillslope gradient (Figures 2.14 and 3.8).

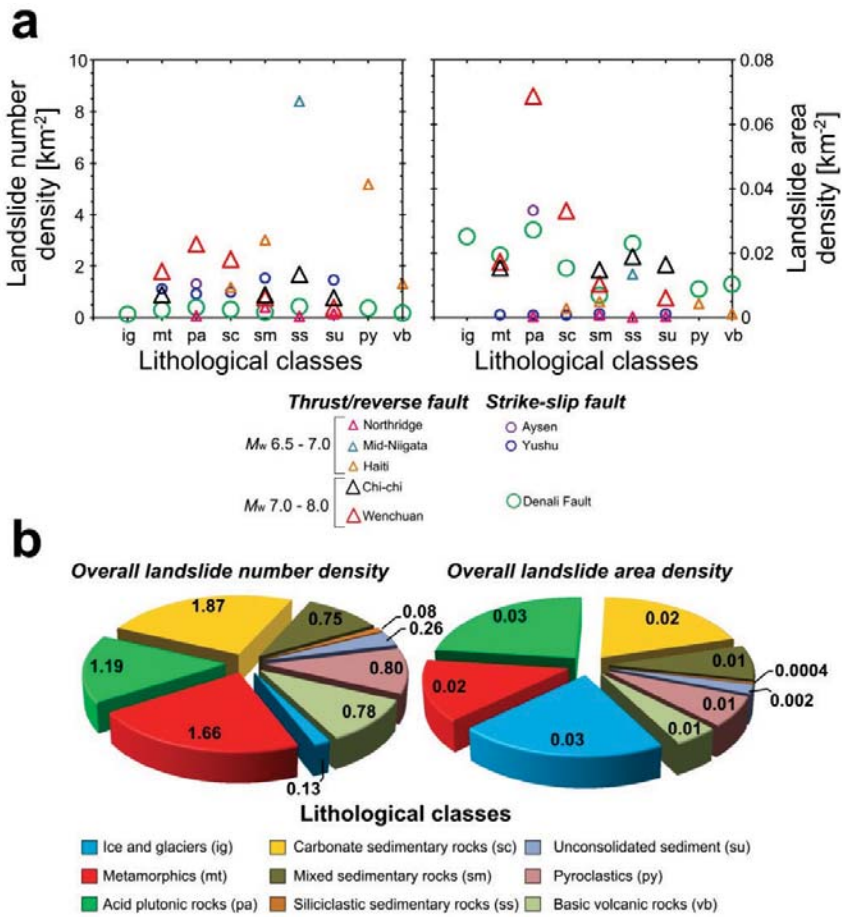

Figure 6.3 Density of coseismic landslides in different geological units. (**a**) Number and area density of landslides triggered by different earthquakes. (**b**) Overall number and area density of landslides triggered by the eight case earthquakes. The classification of lithological units is based on a new global lithological map database (GLiM) (Hartmann and Moosdorf, 2012).

In the comparison of the earthquakes with similar faulting mechanisms (see chapter 3 and 4, Figures 3.12 and 4.9), the direct effect of regional differences in the topographic relief and hillslope steepness on the spatial pattern and size-distribution of coseismic landslides were underlined. Apart from the regional differences in the topography, the local differences in the topographic conditions also have a large effect on the abundance and spatial pattern of coseismic landslides. For example in the M_w 7.0 Haiti earthquake case we showed that while the delta and low hilly zone in the west of the epicenter were

subjected to the highest coseismic deformation, the below-average local relief and hillslope gradients reduced coseismic landslide density, which strikingly mimics the trends of mean local relief and slope gradient over >70 km along the Enriquillo–Plantain Garden Fault. Additionally, judging from topographic location and terrain ruggedness of the coseismic landslides we infer that seismic site effects were prevalent in the rugged terrains such as deeply incised valleys, ridges, steep slopes and cliffs where sudden hillslope changes are common. From a regional geomorphological perspective, coseismic landslide patterns in glaciated landscapes (e.g. in the Denali Fault earthquake struck region) were less abundant, indicating that the glaciers may reduce the topographic amplification though significantly increase the run-out size of the landslides. In this regard, regional morphoclimatic and physiographic differences may affect the distribution characteristics, particularly frequency-size distributions of coseismic landslides. However, in order to be able to study these geomorphologic and climatic effects on coseismic landslide distribution, more inventories are needed covering a variety of terrains.

6.6 A new conceptual model framework of earthquake triggered landslide patterns

Based on the synthesis of the results, as discussed in the previous sections, a conceptual model has been developed to visualize the diversity of causal interactions and the potential contributions of magnitude, faulting type, occurrence of surface or blind ruptures, coseismic displacement and topography with regard to the density and spatial pattern of earthquake-induced landslides. The model is presented in Figure 6.4, and forms the overall conclusion of this research. The empirical equations proposed by Coppersmith (1994) were taken as the basis in establishing scaling consistency for the seismic factors in the model i.e. fault length and average displacement values (Equations 6.1 to 6.4).

$$log(Lss)=1.49+0.64log\,(M) \quad \text{(S.D.=0.27, } n\text{=55)} \quad (6.1)$$

$$log(Lt)=1.36+0.35log\,(M) \quad \text{(S.D.=0.39, } n\text{=21)} \quad (6.2)$$

$$log(AD_{Lss})=-6.32+0.90\,(M) \quad \text{(S.D.=0.28, } n\text{=29)} \quad (6.3)$$

$$log(AD_{Lt})=-0.74+0.08\,(M) \quad \text{(S.D.=0.38, } n\text{=15)} \quad (6.4)$$

where *Lss* and *Lt* are the rupture length of strike-slip and thrust/reverse fault, S.D. is the standard deviation, n is the sample number and AD is the average displacement.

The conceptual model first defines the impacts of different magnitude earthquakes on the density of coseismic landslides for strike-slip and thrust/reverse faults (Figure 6.4a-d). In this regard, the landsliding ratio increases considerably with the increase in earthquake magnitude. However, this increase changes both spatially and in terms of area affected by the landslides depending on the fault type and the distance to the fault (Figure 6.4a and b). Therefore, especially the pattern of landslide distribution induced by surface-ruptured strike-slip faulting earthquakes has a symmetric form and is distributed in a narrow zone. On the other hand, for thrust/reverse faulting earthquakes, the landslides are concentrated asymmetrically, with a much higher density on the hanging wall sections across the fault. As a result, the components of thrust/reverse faults should be evaluated separately in terms of hanging and foot wall blocks and distance to fault. In addition, for a given magnitude the proportion of the area affected by landslides is considerably higher in thrust/reverse faulting earthquakes (Figure 6.4b). As discussed in the previous sections, this is mainly caused by the fact that the planes of thrust or reverse faults are low angle and more importantly their vertical deformation components are high.

In the model, surface- and blind-ruptured earthquakes were also considered in addition to the magnitude, fault type and geometry (Figure 6.4c and d). Landslide density peaks are more subdued and the landslide distribution has a more dispersed form in blind-rupture earthquakes as compared to surface-rupture earthquakes. In the blind-rupture strike-slip faulting earthquakes, the symmetry is conserved in terms of landslide distribution pattern between the fault blocks. Furthermore, the symmetric pattern is even more pronounced due to the decreased landslide ratio between the fault blocks. However, the fraction of the area still remains higher on the hanging wall side (Figure 6.4c and d). In the model, the proposed distribution curve for the blind-ruptured strike-slip faulting earthquakes is questionable because these types of earthquakes were represented with only a single event-inventory in the thesis. In this respect, additional inventories are required to be able to refine the landslide distribution pattern for this type of events.

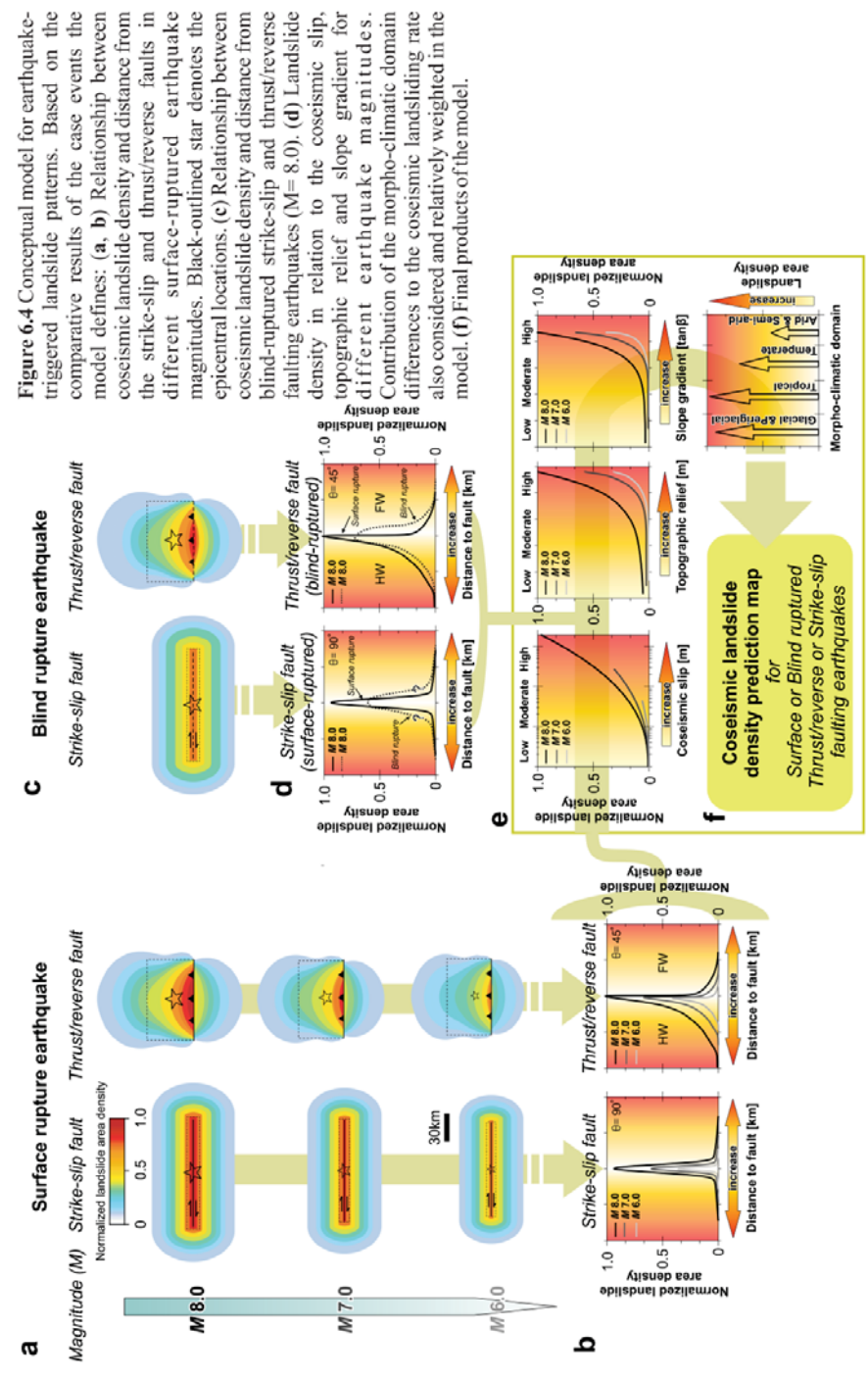

Figure 6.4 Conceptual model for earthquake-triggered landslide patterns. Based on the comparative results of the case events the model defines: (**a**, **b**) Relationship between coseismic landslide density and distance from the strike-slip and thrust/reverse faults in different surface-ruptured earthquake magnitudes. Black-outlined star denotes the epicentral locations. (**c**) Relationship between coseismic landslide density and distance from blind-ruptured strike-slip and thrust/reverse faulting earthquakes (M= 8.0). (**d**) Landslide density in relation to the coseismic slip, topographic relief and slope gradient for different earthquake magnitudes. Contribution of the morpho-climatic domain differences to the coseismic landsliding rate also considered and relatively weighted in the model. (**f**) Final products of the model.

In addition to the factors mentioned in the previous paragraphs, coseismic slip rate and topographic conditions also have an important effect on the landslide density and pattern in the near-field and along the fault. The relations between these factors and the landslide density for different magnitude earthquakes were defined in the model (Figure 6.4e). The relation between coseismic slip or displacement and the landslide density is represented by a power-law function. There is a about two-orders of magnitude difference in the landslide density values between a large earthquake with a high coseismic slip rate, which depends on the magnitude and the rupture length of the earthquake, and a low magnitude earthquake (taken as M= 6.0 in the model). However, this ratio can change under certain conditions. For example, the landslide density can be still low in strike-slip faulting earthquakes with high rupture velocities and super-shear rupture propagations despite experiencing a high coseismic slip rate. In these types of events and the related fault segments, this phenomenon can generally be explained by the conditions of less high-frequency energy radiation. Therefore, the earthquakes that contain super-shear rupture propagations should be examined with more care. The local differences in the topographic conditions also have a large effect on the density and spatial pattern of coseismic landslides, which is illustrated in Figure 6.4e. The available data from the different events showed that local relief and hillslope gradient have a nonlinear relationship with landslide density. The proposed conceptual model also includes first-order morphogenetic or morpho-climatic domains. The significant increases in the run-out size of the landslides at the glaciated areas enabled us to consider the morpho-climatic domains (simplified into four situation) as an additional factor. The following morpho-climatic situations were identified: (Peri)glacial, tropical, temperate and (Semi)arid. We carried out a relative weighting for the coseismic landslide densities considering the depth of weathering degree, the intensity of continuous or periodical wet periods, or low-friction surfaces such as glaciers. These domains can be expanded or modified considering the local conditions. As these conditions can vary greatly within the mountainous terrains, their significance related with the topography should be studied in more detail in future.

To conclude, predictive mapping of the density and the pattern of coseismic landslides can be estimated or improved by the proposed conceptual model (Figure 6.4). Based on the limited number of available earthquake-induced landslide inventories an attempt was made to generate empirical relations that show the landslide density as a function of fault type, magnitude, and distance from the fault.

The findings and issues discussed in the previous chapters are closely linked to the characterization of the density and the pattern of the coseismic landslides. In this respect, the conceptual model for earthquake triggered landslides obviously requires a large amount of available data and further theoretical research that makes it more suitable and applicable for assessing earthquake-induced landslide susceptibility at the present stage. However, our integrative approach can serve as a starting point to build a better picture of the regional distribution and the characteristics of landslides which are closely connected in a causal chain not only with the magnitude of the earthquake but also with the fault geometry and type, the changes in geomorphic and topographic characteristics, and the rate and mode of the coseismic displacements along the surface ruptures. The results show that the variance in rollovers of magnitude-frequency distributions become more pronounced with differences in style of faulting, rupture and the topographic characteristics of the events. Therefore, landslide frequency-size distributions of similar magnitude earthquakes show that future work should consider the seismic properties (i.e. magnitude, faulting mechanism and rupture dynamics) and physiographic characteristics together rather focusing on earthquake magnitude alone. The findings caution against overly relying on across-the-board models of slope stability response to seismic ground shaking.

6.7 Implications and recommendations for future research directions

The results of the presented case studies support that, in the near-field, the differences and variations in fault geometry, rupture processes (coseismic slip rate, rake, rupture directivity and velocities), together with regional contrasts in geomorphology and tectonic setting, are governing the pattern of coseismic landslides. Overall, coseismic landslide density and pattern variations along the ruptures reflect in many ways the differences in the earthquake rupture processes. Therefore, coseismic landslides can be considered as natural seismometers under certain conditions. The distribution pattern of coseismic landslides offers additional perspectives for a better understanding of historical earthquakes in poorly seismic instrumented regions. The fact that the majority of the largest landslides triggered by the strong earthquakes are located above the asperities or high slip-patches in the near-field fault zones can contribute in developing novel paleoseismologic interpretations about the magnitude and location of the historical earthquakes, particularly for those lacking fault

exposures. In this respect, additional inventories are required to be able to refine how earthquake source properties control landslide triggering.

The results have also important implications for sediment flux and landscape evolution modelling studies in tectonically active landscapes. In tectonically active mountain belts, earthquake triggered landslides deliver large amounts of sediment to rivers. With the insights from seismologically and geomorphologically well-instrumented and documented cases, it will be possible to explore the stochastic nature of seismically induced erosion, and seismic and post-seismic sediment production and budgets which will further help to quantitatively resolve the topographic net effect of large earthquakes that culminate in the competition between mountain-belt formation through uplift, and topographic decay through coseismic landsliding in active tectonic areas.

Furthermore, it is a challenge to predict spatially the asperity areas or high slip patches that can form in a probable earthquake. There is a possibility for a general estimation of these areas in the fault zones that have been studied comprehensively in terms of geological and geophysical characteristics (i.e. San Andreas Fault Zone). Accordingly, developing coseismic slip models based on the results from scenario earthquakes will help for a better prediction of the possible landslide pattern. Therefore, for the places with high risk of earthquake-induced hazards, there is need for more advanced structural geologic, paleoseismologic, geodesic and geophysical studies.

The event inventory maps are an essential part of seismic landslide susceptibility and hazard analysis. However, to establish a substantially complete event-inventory is a highly time demanding process, which depends on the size of the area affected by the earthquake and the number of the individual landslides triggered by event. Despite the new efforts in semi-automatic or automatic detection of landslides based on object-oriented methods, the results from these new approaches are still not at the desired level for detecting the individual landslides. Therefore, there is still need for further future work for developing advanced algorithms that can establish substantially complete event-inventory with high accuracy.

Due to the complex nature of earthquake-induced landslides, several methods have been applied for the assessment of landslide susceptibility and hazard at a medium scale. Geographic Information System (GIS) based analysis of earthquake-induced landslide susceptibility includes three components which

are commonly used together: pseudo-static slope stability analysis, models for the attenuation of ground shaking, and (integrated versions of the) Newmark's displacement method (e.g. Jibson et al. 1998) or fuzzy logic system based approaches to estimate the failure probability via membership functions and if-then rules (e.g. Miles and Keefer, 2009). The main drawbacks of these methods are the high degree of oversimplification and the lack of validation due to their application to less than two events. The empirical relations developed in this thesis needs to be further improved with data from more earthquake-induced landslide inventories, and should be integrated with the existing approaches. Considering the complex and nonlinear between the landside density and other factors described in the conceptual model and the availability of a limited number of digital landslide event-inventories, Mamdani fuzzy inference system (Mamdani and Assilian, 1975), which is transparent and allows explicit expression of knowledge of the system via fuzzy “if–then” rules, can be one of the most feasible methods to integrate with the model proposed in the thesis. In this regard, there is need for testing the applicability, prediction capacity and reliability of the model that will integrate the fuzzy rule sets based on the proposed conceptual model. As a further step, the model could eventually be used in a real time mode (shortly after an event), once the information of the hypocentral location, magnitude and mechanism of the event are known in a particular area. For such a case, the results should be made rapidly available via the Web through a variety of map formats, including GIS coverages.

According to the records of the last thirty years of U.S. Geological Survey, there has been 458 earthquakes with M>7.0, 3850 with M>6.0 and 38,000 with M>5.0. However, the number of digital coseismic landslide event-inventories available is only 16. Therefore, to improve the current state of coseismic landslide knowledge the greatest research need we see is for the complete inventorying and comprehensive study of landslides generated by many more earthquakes. Also, sharing of such complete inventories should be promoted through internet based open data platforms in the future.

Appendix

Table A1 Satellite images data index table of Wenchuan earthquake

Pre-Earthquake

Id	Date	Sensor	Resolution (m)	Spectral Information	Source	Production ID
1	02.19.03	ASTER	15	MS(VNIR)	Terra-ASTER	L1A0030219200303572803142003165639
2	02.19.03	ASTER	15	MS(VNIR)	Terra-ASTER	L1A0030219200303574603142003165712
3	02.19.03	ASTER	15	MS(VNIR)	Terra-ASTER	L1A0030219200303573703142003165656
4	08.30.00	ASTER	15	MS(VNIR)	Terra-ASTER	L1A0030830200004053101012003173757
5	03.31.06	ASTER	15	MS(VNIR)	Terra-ASTER	L1A0030331200603554504022006161342
6	09.05.02	ASTER	15	MS(VNIR)	Terra-ASTER	L1A0030905200203514109202002201647
7	06.14.01	ASTER	15	MS(VNIR)	Terra-ASTER	L1A0030614200103590706192001193607
8	06.14.01	ASTER	15	MS(VNIR)	Terra-ASTER	L1A0030614200103585806192001193546
9	06.30.01	ASTER	15	MS(VNIR)	Terra-ASTER	L1A0030630200103581907062001152354
10	04.18.01	ASTER	15	MS(VNIR)	Terra-ASTER	L1A0030418200104065501202004225713
11	08.27.02	ASTER	15	MS(VNIR)	Terra-ASTER	L1A0030827200203581210052002170010
12	02.19.03	ASTER	15	MS(VNIR)	Terra-ASTER	L1A0030219200303571903142003165623
13	08.30.00	ASTER	15	MS(VNIR)	Terra-ASTER	L1A0030830200004052201012003173741
14	08.30.00	ASTER	15	MS(VNIR)	Terra-ASTER	L1A0030830200004051301012003173724
15	03.31.07	ALOS	10	MS (AVNIR-2)	JAXA	ALAV2A062882960
16	03.31.07	ALOS	10	MS (AVNIR-2)	JAXA	ALAV2A062882970
17	04.17.07	ALOS	10	MS (AVNIR-2)	JAXA	ALAV2A065362960
18	01.02.07	ALOS	10	MS (AVNIR-2)	JAXA	ALAV2A054422950
19	11.28.07	ALOS	10	MS (AVNIR-2)	JAXA	ALAV2A098182940
20	11.28.07	ALOS	10	MS (AVNIR-2)	JAXA	ALAV2A098182950
21	05.06.08	ALOS	2.5	PAN (PRISM)	JAXA	ALPSMN121522965
22	05.06.08	ALOS	2.5	PAN (PRISM)	JAXA	ALPSMN121522970
23	08.30.06	ALOS	2.5	PAN (PRISM)	JAXA	ALPSMN031812960
24	04.19.07	CARTOSAT-1	2.5	PAN	ISRO	097027500102
25	04.19.07	CARTOSAT-1	2.5	PAN	ISRO	097027500202
26	04.19.07	CARTOSAT-1	2.5	PAN	ISRO	097027500302

Post-Earthquake

1	07.10.08	ASTER	15	MS(VNIR)	Terra-ASTER	L1A0030710200803570207152008112907
2	05.30.08	ASTER	15	MS(VNIR)	Terra-ASTER	L1A0030530200804024606022008170420
3	07.10.08	ASTER	15	MS(VNIR)	Terra-ASTER	L1A0030710200803565307152008112859
4	05.23.08	ASTER	15	MS(VNIR)	Terra-ASTER	L1A0030523200803570905282008121510
5	05.23.08	ASTER	15	MS(VNIR)	Terra-ASTER	L1A0030523200803565105282008121456
6	05.23.08	ASTER	15	MS(VNIR)	Terra-ASTER	L1A0030523200803570005282008121503
7	05.16.08	ASTER	15	MS(VNIR)	Terra-ASTER	L1A0030516200803504705192008111553
8	06.08.08	ASTER	15	MS(VNIR)	Terra-ASTER	L1A0030608200803571206112008121132
9	12.10.08	ASTER	15	MS(VNIR)	Terra-ASTER	L1A0031210200803504612132008113610
10	07.26.08	ASTER	15	MS(VNIR)	Terra-ASTER	L1A0030726200803564009262008160248
11	12.10.08	ASTER	15	MS(VNIR)	Terra-ASTER	L1A0031210200803505512132008113619
12	05.16.08	ASTER	15	MS(VNIR)	Terra-ASTER	L1A0030516200803502905192008111529
13	05.18.08	ALOS	2.5	PAN (PRISM)	JAXA	ALPSMW123272955
14	05.23.08	ALOS	10	MS (AVNIR-2)	JAXA	ALAV2A124002930
15	06.04.08	ALOS	10	MS (AVNIR-2)	JAXA	ALAV2A125752950
16	06.04.08	ALOS	10	MS (AVNIR-2)	JAXA	ALAV2A125752960
17	06.04.08	ALOS	10	MS (AVNIR-2)	JAXA	ALAV2A125752970
18	10.13.08	SPOT-5	2.5	PAN	Spot Image S.A	5261286/108/10/13
19	07.01.08	IKONOS	2.5+4	PAN+MS	Geo-Eye	325523
20	05.23.08	IKONOS	2.5+4	PAN+MS	Geo-Eye	325578
21	06.28.08	IKONOS	2.5+4	PAN+MS	Geo-Eye	325583
22	05.23.08	IKONOS	2.5+4	PAN+MS	Geo-Eye	325579
23	06.28.08	IKONOS	2.5+4	PAN+MS	Geo-Eye	325584
24	01.24.09	CARTOSAT-1	2.5	PAN	ISRO	097027500402
25	01.24.09	CARTOSAT-1	2.5	PAN	ISRO	097027500502
26	01.24.09	CARTOSAT-1	2.5	PAN	ISRO	097027500602

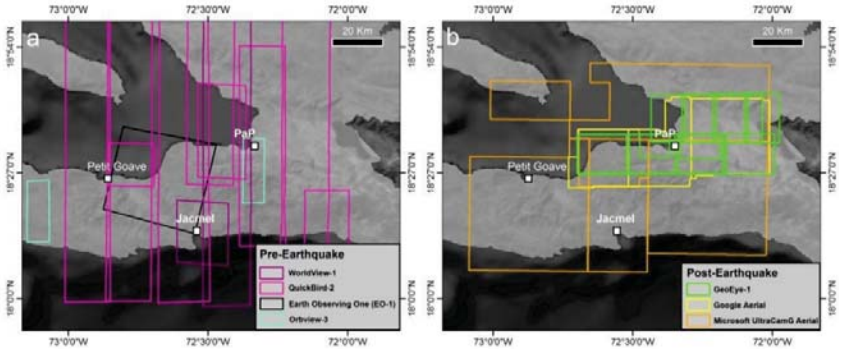

Figure A1 Pre- and post-earthquake aerial photo and satellite image coverage of Haiti earthquake.

Table A2 Aerial photos and satellite images data index table of Haiti earthquake.

Pre-Earthquake

Id	Date	Sensor	Resolution (m)	Data Type	Source	Number of Scenes	Description
1	2/3/2003	EO-1	10	Satellite	USGS	1	Earth Observing One image
2	9/14/2004	OrbView-3	1.00	Satellite	USGS	1	OrbView image
3	5/12/2005	OrbView-3	2.00	Satellite	USGS	1	OrbView image
4	7/3/2002	QuickBird-2	0.60	Satellite	DigitalGlobe©	1	QuickBird image, ortho and mosaic
5	8/31/2002	QuickBird-2	0.60	Satellite	DigitalGlobe©	1	QuickBird image, ortho and mosaic
6	11/21/2004	QuickBird-2	0.60	Satellite	DigitalGlobe©	1	QuickBird image, ortho and mosaic
7	3/17/2005	QuickBird-2	0.60	Satellite	DigitalGlobe©	1	QuickBird image, ortho and mosaic
8	6/2/2005	QuickBird-2	0.60	Satellite	DigitalGlobe©	1	QuickBird image, ortho and mosaic
9	7/26/2005	QuickBird-2	0.60	Satellite	DigitalGlobe©	1	QuickBird image, ortho and mosaic
10	1/22/2006	QuickBird-2	0.60	Satellite	DigitalGlobe©	1	QuickBird image, ortho and mosaic
11	7/8/2008	QuickBird-2	0.60	Satellite	DigitalGlobe©	1	QuickBird image, ortho and mosaic
12	7/24/2009	QuickBird-2	0.60	Satellite	DigitalGlobe©	1	QuickBird image, ortho and mosaic
13	12/23/2008	WorldView-1	0.50	Satellite	DigitalGlobe©	1	WorldView image, ortho and mosaic
14	12/11/2009	WorldView-1	0.50	Satellite	DigitalGlobe©	1	WorldView image, ortho and mosaic

Post-Earthquake

1	1/21/2010	unknown	0.15	Aerial	Google©	6697	Images, mosaics
2	1/28/2010	UltraCamG	0.30	Aerial	Microsoft©	434	Images, mosaics
3	1/13/2010	GeoEye-1	0.41	Satellite	GeoEye©	20	GeoEye images, ortho and mosaics

Table A3 Well documented and substantially complete inventories of landslides triggered by earthquakes in the last 40

Date	Location	M_w	Depth (km)	Number of landslides	Fault type	Dip (degree)	Dip direction	Strike (degree)	Data source
October 26, 1997	Umbria Marche, Italy	6.0	6	124	Normal	40	SW	140	Bozzano, 1998; Esposito et al., 2000
April 6, 2009	L'Aquila, Italy	6.3	5	79	Normal	43	SW	147	Guzzetti et al., 2009; Galli et al., 2010
July 18, 2004	Rotoehu, New Zelland	5.6	6	45	Normal	61	SE	35	Hancox et al., 2004; Hurst et al., 2008
April 21, 2007	Aysen, Chile†	6.2	10	514	Strike-slip	88	E	354	Lange et al., 2008; Mora et al., 2010
October 17, 1989	Loma Prieta, USA	6.9	17.6	2000	Strike-slip	70	SW	130	Keefer and Manson 1998; Marshall et al., 1991
November 3, 2002	Alaska-Denali, USA†	7.9	7.5	1580	Strike-slip	90	-	111	Haeussler et al., 2004
April 14, 2010	Yushu, China	6.8	16	2036	Strike-slip	87	NNE	298	Li et al., 2011; Xu et al., 2012
May 25, 1980	Mammoth Lakes, USA	6.2	10	5253	Strike-slip	50	SE	78	Given et al., 1982; Harp et al., 1984
January 12, 2010	Haiti†	7.0	13	4406	Thrust/reverse	42	N	251	Hayes et al., 2010
January 17, 1994	Northridge, USA	6.7	17.5	11111	Thrust/reverse	40	S	122	Harp and Jibson 1995; Shen et al., 1996
September 20, 1999	Chi-Chi, Taiwan	7.6	7	22000	Thrust/reverse	30	E	5	Chen et al., 2003; Liao and Lee 2000
May 12, 2008	Wenchuan,China†	7.9	19	60574	Thrust/reverse	43	NW	231	Shen et al., 2009; Zhao et al., 2010
May 2, 1983	Coalinga, USA	6.5	10	9389	Thrust/reverse	23	SW	236	Harp, 1990; Rymer et al., 1990
October 23, 2004	Mid-Niigata, Japan	6.8	13	4400	Thrust/reverse	57	W	11	Maruyama et al., 2005; Yamagishi and Iwahashi 2007
June 14, 2008	Iwate-Miyagi Nairiku, Japan	6.9	8	4161	Thrust/reverse	31	NNW	198	Ohta et al., 2008; Yagi et al., 2009

† Landslide event-inventories which were generated within the scope of this thesis.

Bibliography

Abrahamson, N.A., Silva W.J., 1997. Empirical response spectral attenuation relations for shallow crustal earthquakes. Seismological Research Letters 68, 94–127.

Abrahamson, N.A., Silva, W.J, 2008. Summary of the Abrahamson & Silva NGA ground-motion relations. Earthquake Spectra 24, 67-97.

Abrahamson, N.A., Somerville, P.C., 1996. Effects of the Hanging Wall and Footwall on Ground Motions Recorded during the Northridge Earthquake. Bulletin of the Seismological Society of America 86, 93-99.

Alfaro, P., Delgado, J., García-Tortosa, F.J., Lenti, L., López J.A., López-Casado C., Martino, S., 2012. Widespread landslides induced by the M_w 5.1 earthquake of 11 May 2011 in Lorca, SE Spain. Engineering Geology 137-138, 40–52.

Allen, C. R., J. N. Brune, L. S. Cluff, and A. G. Barrows (1998). Evidence for unusually strong near-field ground motion on the hanging wall of the San Fernando fault during the 1971 earthquake. Seism. Res. Lett. 69, 524-531.

Anderson, J.G., 2003. Strong-motion seismology. In: William, H.K.L., Kanamori, H., Jennings, P.C., Kisslinger, C. (Eds.), International Handbook of Earthquake and Engineering Seismology (Part B), Academic Press, Vol. 81, pp. 937-965.

Avouac, J.P., Ayoub, F., Leprince, S., Konca, O., Helmberger, D.V., 2006. The 2005, M-w 7.6 Kashmir earthquake: Sub-pixel correlation of ASTER images and seismic waveforms analysis. Earth and Planetary Science Letters 249, 514-528.

Bakun, W.H., Flores, C.H., ten Brink, US., 2012. Significant Earthquakes on the Enriquillo Fault System, Hispaniola, 1500–2010: Implications for Seismic Hazard. Bulletin of the Seismological Society of America 102, 18-30.

Barka, A., Akyuz, H.S., Altunel, E., Sunal, G., Cakir, Z., Dikbas, A., Yerli, B., Armijo, R., Meyer, B., de Chabalier, J.B., Rockwell, T., Dolan, J.R., Hartleb, R., Dawson, T., Christofferson, S., Tucker, A., Fumal, T., Langridge, R., Stenner, H., Lettis, W., Bachhuber, J., Page, W., 2002. The surface rupture and slip distribution of the 17 August 1999 Izmit earthquake (M 7.4), North Anatolian fault. Bulletin of the Seismological Society of America 92, 43-60.

Ben-Zion, Y., Huang, Y., 2002. Dynamic rupture on an interface between a compliant fault zone layer and a stiffer surrounding solid. Journal Geophysical Research 107, 2042, doi:10.1029/2001JB000254.

Ben-Zion, Y., Sammis, C.G., 2003. Characterization of Fault Zones. Pure and Applied Geophysics 160, 677-715.

Bird, M.I., Longstaffe, F.J., Fyfe, W.S., Bildgen, P., 1992. Oxygen-isotope systematics in a multiphase weathering system in Haiti. Geochimica Et Cosmochimica Acta 56,

2831-2838.

Bonilla, M.G., 1988. Minimum earthquake magnitude associated with coseismic surface faulting. Bulletin of the International Association of Engineering Geology 25, 17–29.

Bozzano, F., Gambino, P., Prestininzi, A., Scarascia Mugnozza, G., Valentini, G., 1998. Ground effects induced by the Umbria-marche earthquakes of September-October 1997, Central Italy. Proc. 8th Cong. IAEG, Vancouver, 2, 825-830.

Bucknam, R.C., Coe, J.A., Mota, A., Godt, J.W., Tarr, A.C., Bradley, L.-A., Rafferty, S., Hancock, D., Dart, R.L., 2001. Landslides triggered by Hurricane Mitch in Guatemala - Inventory and discussion: U.S. Geological Survey Open-File Report 01-443, 40 p., 23 plates.

Burchfiel, B.C., Royden, L.H., van der Hilst, R.D., Hager, B.H., Chen, Z., King, R.W., Li, C., Lu, J., Yao, H., Kirby, E., 2008. A geological and geophysical context for the Wenchuan earthquake of 12 May 2008, Sichuan, People's Republic of China. GSA Today 18 (7), 4-11.

Burridge, R., Conn, G., Freund, L.B., 1979. The stability of a plane strain shear crack with finite cohesive force running at intersonic speeds. J. Geophys. Res 84, 2210-2222.

Cakir, Z., de Chabalier, J.B., Armijo, R., Meyer, B., Barka, A., Peltzer, G., 2003. Coseismic and early post-seismic slip associated with the 1999 Izmit earthquake (Turkey), from SAR interferometry and tectonic field observations. Geophysical Journal International 155, 93-110.

Calais, E., Freed, A., Mattioli, G., Amelung, F., Jónsson, S., Jansma, P., Hong, S.-H., Dixon, T., Prépetit, C., Momplaisir, R., 2010. Transpressional rupture of an unmapped fault during the 2010, Haiti earthquake, Nature Geoscience 3, 794-799.

Campbell, K.W., 1981. Near-source attenuation of peak horizontal acceleration. Bulletin of the Seismological Society of America 71, 2039–2070.

Campbell, K.W., 2003. Strong-motion attenuation relations. In: William, H.K.L., Kanamori, H., Jennings, P.C., Kisslinger, C. (Eds.), International Handbook of Earthquake and Engineering Seismology (Part B), Vol. 81. Academic Press, New York, pp.1003-1012.

Capps, S. R. 1940: Geology of the Alaska railroad region. United States Department of the Interior. Geological Survey Bulletin 907, 1-201.

Cavallo, E.A., Powell, A., Becerra, O., 2010. Estimating the direct economic damage of the earthquake in Haiti. IDB Working Paper Series 163, 16 p.

Chang, T.-Y., Cotton, F., Tsai, Y.-B., Angelier, J., 2004. Quantification of hanging-wall

effects on ground motion: some insights from the 1999 Chi-Chi earthquake. Bulletin of the Seismological Society of America 94, 2186-2197.

Chen, J., Helmberger, D.V., Wald, D.J., Ma, K.F., 2003. Slip history and dynamic implications of the 1999 Chi-Chi, Taiwan, earthquake. Journal of Geophysical Research 108 (B9), 2412. doi:10.1029/2002JB001764.

Chengdu Institute of Geology and Mineral Resources, 2004. Geological Map of the Qingha-Xizang (Tibet) Plateau and Adjacent Areas, Map, Geological, Beijing.

Chigira, M., Wang, W.N., Furuya, T., Kamai, T., 2003. Geological causes and geomorphological precursors of theTsaoling landslide triggered by the 1999 Chi-Chi Earthquake, Taiwan. Engineering Geology 68, 259-273.

Chigira, M., Yagi, H., 2006. Geological and geomorphological characteristics of landslides triggered by the 2004 Mid Niigta prefecture earthquake in Japan. Engineering Geology 82, 202-221.

China Earthquake Administration (CEA)., 2008. Magnitude of the 12 May 2008 Wenchuan Earthquake and aftershocks.

Clague, J. J., Evans, S. G., 1994. Formation and failure of natural dams in the Canadian Cordillera. Geological Survey of Canada Bulletin 464, 35pp.

Cocco, M., and A. Rovelli (1989). Evidence for the variation of stress drop between normal and thrust faulting earthquakes in Italy. J. Geophys. Res. 94, 9399–9416.

Crone, A.J., Personius, S.F., Craw, P.A., Haeussler, P.J., Staft, L.A., 2004. The Susitna Glacier Thrust Fault: Characteristics of Surface Ruptures on the Fault that Initiated the 2002 Denali Fault Earthquake. Bull. Seismol. Soc. Am. 94(6B), 5-22.

Crozier, M.J., Deimel, M.S., Simon, J.S., 1995. Investigation of Earthquake Triggering for Deep-seated Landslides, Taranaki, New Zealand. Quaternary International 25, 65-73.

Csejtey, B., 1976. Tectonic implications of a late Paleozoic volcanic arc in the Talkeetna Mountains, south-central Alaska, Geology 4 (1), 49-52.

Cui, P., Zhu, Y.Y., Han, Y.S., Chen, X.Q., Zhuang, J.Q., 2009. The 12 May Wenchuan earthquake-induced landslide lakes: distribution and preliminary risk evaluation. Landslides 6, 209-223.

Dai, F.C., Xu, C., Yao, X., Xu, L., Tu, X.B., Gong, Q.M., 2011. Spatial distribution of landslides triggered by the 2008 Ms 8.0 Wenchuan earthquake, China. Journal of Asian Earth Sciences 40, 883-895.

Densmore, A.L., Ellis, M.A., Li, Y., Zhou, R., Hancock, G.S., Richardson, N., 2007. Active tectonics of the Beichuan and Pengguan fault at the eastern margin of the Tibetan Plateau. Tectonics 26(4), TC4005.

Densmore, A.L., Hovius, N. 2000. Topographic fingerprint of bedrock landslides. Geology 28, 371-374.

Dirks, P., Wilson, C.J.L., Chen, S., Luo, Z., Lin, S., 1994. Tectonic evolution of the NE margin of the Tibetan Plateau: evidence from the central Longmen Mountains, Sichuan Province, China. Journal of Southeast Asian Earth Sciences 9, 181-192.

Dor, O., Ben-Zion, Y., Rockwell, T.K., Brune, J.N., 2006. Pulverized rocks in the Mojave section of the San Andreas fault zone, Earth and Planetary Science Letters 245, 642-654.

Dortch, J.M., Owen, L.A., Caffe, M.W., Brease, P., 2010, Late Quaternary glaciation and equilibrium line altitude variations of the McKinley River region, central Alaska Range. Boreas 39, 233-246.

Du, Y., Xie, F., Zhang, X., Jing, Z., 2009. The mechanics of fault slip of the Ms 8.0 Wenchuan earthquake (in Chinese), Chin. J. Geophys., 52, 464-473.

Duan, B. 2010. Role of initial stress rotations in rupture dynamics and ground motion: A case study with implications for the Wenchuan earthquake. Journal of Geophysical Research 115, B05301 doi:10.1029/2009JB006750.

Dunham, E.M., Archuleta, R.J., 2004. Evidence for a Super-shear Transient during the 2002 Denali Fault Earthquake. Bull. Seismol. Soc. Am. 94(6B), 256-268.

Dunham, E.M., Bhat, H.S., 2008. Attenuation of radiated ground motion and stresses from three-dimensional super-shear ruptures Journal of Geophysical Research 113, B08319, doi:10.1029/2007JB005182.

Dunning, S.A., Mitchell, W.A., Petley, D.N., Rosser, N.J., Cox, N.J., 2007. Landslides predating and triggered by the 2005 Kashmir earthquake: rockfall to rock avalanches. Geophys. Res. Abstr. 9, 06376.

Eberhart-Phillips, D., Sieh, K., Rubin, C., 2003. The 2002 Denali Fault earthquake, Alaska. Science 300, 1113–1118.

Escuder-Viruete, J., Perez-Estaun, A., Contreras, F., Joubert, M., Weis, D., Ullrich, T.D., Spadea, P., 2007. Plume mantle source heterogeneity through time: Insights from the Duarte Complex, Hispaniola, northeastern Caribbean. Journal of Geophysical Research 112 (B4), B04203. doi:10.1029/2006JB004323.

Esposito, E., Porfido, S., Simonelli, A. L., Mastrolorenzo, G., Iaccarino, G., 2000. Landslides and other surface effects induced by the 1997 Umbria–Marche seismic sequence. Engineering Geology 58(3), 353-376.

Faccioli, E., Vanini, M., Frassine, L., 2002. Complex site effects in earthquake ground motion, including topography. In: 12th European Conference on Earthquake Engineering 9-13 September 2002, Barbican Centre, London, UK. Paper Reference

844, 22p.

Fan, X., van Westen, C.J., Korup, O., Gorum, T., Xu, Q., Dai, F.C., Huang, R.Q., Wang, G., 2012a. Transient water and sediment storage of the decaying landslide dams induced by the 2008 Wenchuan earthquake, China. Geomorphology 171-172, 58-68.

Fan, X., van Westen, C.J., Xu, Q., Gorum, T., Dai, F.C., 2012b. Analysis of landslide dams induced by the 2008 Wenchuan earthquake. Journal of Asian Earth Sciences 57, 25-37.

Fiorucci, F., Cardinali, M., Carlà, R., Rossi, M., Mondini, A.C., Santurri, L., Ardizzone, F., Guzzetti, F., 2011. Seasonal landslide mapping and estimation of landslide mobilization rates using aerial and satellite images. Geomorphology 129, 59-70.

Frankel, A., 2004. Rupture process of the M7.9 Denali Fault, Alaska, earthquake: Sub-events, directivity, and scaling of high-frequency ground motions, Bull. Seismol. Soc. Am., 94(6B), 234-255.

Fukuyama, E., 2009. Fault-Zone Properties and Earthquake Rupture Dynamics. In: Fukuyama, E. (Ed.), Fault-Zone Properties and Earthquake Rupture Dynamics. Elsevier, San Diego, California, pp. 1-13.

Galli, M., Ardizzone, F., Cardinali, M., Guzzetti, F., Reichenbach, P., 2008. Comparing landslide inventory maps. Geomorphology 94, 268-289.

Galli, P., Giaccio, B., Messina, P., 2010. The 2009 central Italy earthquake seen through 0.5 Myr-long tectonic history of the L'Aquila faults system. Quaternary Science Reviews 29(27), 3768-3789.

Given, J.W., Wallace, T.C., Kanamori, H., 1982. Teleseismic analysis of the 1980 Mammoth Lakes earthquake sequence. Bulletin of the Seismological Society of America 72(4), 1093-1109.

Gorum, T., Fan, X., van Westen, C.J., Huang, R., Xu, Q., Tang, C., Wang, G., 2011. Distribution Pattern of Earthquake-induced Landslides Triggered by the 12 May 2008 Wenchuan Earthquake. Geomorphology 133, 152–167.

Gorum, T., van Westen, C.J., Korup, O., van der Meijde, M., Fan, X., van der Meer, F.D., 2013. Complex rupture mechanism and topography control symmetry of mass-wasting pattern, 2010 Haiti earthquake. Geomorphology 184, 127-138.

Guzzetti F., Esposito E., Balducci V., Porfido S., Cardinali M., Violante C., Fiorucci F., Sacchi M., Ardizzone F., Mondini A., Reichenbach P., Rossi M., 2009. Central Italy seismic sequences-induced landsliding: 1997-1998 Umbria-Marche and 2008-2009 L'Aquila cases. Proceedings of the conference "The Next Generation of Research on Earthquake-induced Landslides: International Conference in Commemoration of 10th Anniversary of the Chi-Chi Earthquake, Taiwan", ISBN

978-986-01-9854-6, 52-61.

Guzzetti, F., 2005, Landslide Hazard and Risk Assessment. Unpublished PhD Thesis, University of Bonn, November 2005, 389 pp.

Guzzetti, F., Cardinali, M., Reichenbach, P., Carrara, A., 2000. Comparing landslide maps: a case study in the upper Tiber River Basin, Central Italy. Environmental Management 25, 247-363.

Haeussler, P., Schwartz, D., Dawson, T., Stenner, H., Lienkaemper, J., Sherrod, B., Cinti, F., Montone, P., Craw, P., Crone, A., Personius, S., 2004. Surface rupture and slip distribution of the Denali and Totschunda Faults in the 3 November 2002 M 7.9 Earthquake, Alaska. Bull. Seismol. Soc. Am. 94, 23-52.

Hall-Wallace, M.K., 1998. Can earthquake be predicted? Journal of Geoscience Education 46, 439-449.

Hao, K.X., Si, H., Fujiwara, H., Ozawa, T., 2009. Coseismic surface-ruptures and crustal deformations of the 2008 Wenchuan earthquake M_w 7.9, China. Geophysical Research Letters 36, L11303, doi:101029/2009GL037971.

Harp E.L., Keefer D.K., Sato H.P., Yagi, H., 2011. Landslide inventories: the essential part of seismic landslide hazard analyses. Engineering Geology 122(1-2), 9-21.

Harp, E.L., Jibson, R.W. 1995. Inventory of Landslides Triggered by the 1994 Northridge, California Earthquake, U.S. Geological Survey Open-File Report 95-213.

Harp, E.L., Crone, A.J., 2006. Landslides Triggered by the October 8, 2005, Pakistan Earthquake and Associated Landslide-Dammed Reservoirs. U.S. Geological Survey Open-file report, pp.1052-1065.

Harp, E.L., Jibson, R.W., 1995. Inventory of landslides triggered by the 1994 Northridge, California earthquake. In: US Geol. Surv. Open-File Rep. 95-213, 17 pp.

Harp, E.L., Jibson, R.W., Kayen, R.E., Keefer, D.K., Sherrod, B.L., Carver, G.A., Collins, B.D., Moss, R.E.S., Sitar, N., 2003. Landslides and liquefaction triggered by the M 7.9 Denali Fault earthquake of 3 November 2002. GSA Today 13 (8), 4-10.

Harp, E.L., Sarmiento, J., Cranswick, E., 1984. Seismic-induced pore-water pressure records from the Mammoth Lakes, California, earthquake sequence of 25 to 27 May 1980. Bulletin of the Seismological Society of America, 74(4), 1381-1393.

Harris, R.A., 1998. Introduction to special section: Stress triggers, stress shadows, and implications for seismic hazard. Journal of Geophysical Research 103, 24347-24358.

Hartmann, J., Moosdorf, N., 2012. The new global lithological map database GLiM: A representation of rock properties at the Earth surface. Geochemistry, Geophysics, Geosystems (G^3) 13, 1525-2027.

Hayes, G. P., Briggs, R.W., Sladen A., Fielding E.J., Prentice, C., Hudnut, K., Mann, P., Taylor, F.W., Crone, A. J., Gold, R., Ito, T., Simons, M., 2010. Complex rupture during the 12 January 2010 Haiti earthquake. Nature Geoscience 3, 800–805.

Hengl, T., Reuter, H.I., (Eds.), 2008. Geomorphometry: concepts, software, applications. Developments in Soil Science 33, Elsevier, Amsterdam, 765 pp.

Hreinsdottir, S., Freymueller, J.T., Burgmann, R., Mitchell, J., 2006. Coseismic deformation of the 2002 Denali Fault earthquake: insights from GPS measurements. J. Geophys. Res.-Solid Earth 111, B03308, 1-18 doi:10.1029/2005JB003676.

Hsu, Y.J., Bechor, N., Segall, P., Yu, S.B., Kuo, L.C., Ma, K.F., 2002. Rapid afterslip following the 1999 Chi-Chi, Taiwan Earthquake. Geophysical Research Letters 29, DOI:10.1029/2002GL014967.

Huang, R.Q., Li, W.L., 2009. Analysis of the geo-hazards triggered by the 12 May 2008 Wenchuan Earthquake, China. Bulletin of Engineering Geology and the Environment 68, 363-371.

Hussain, M.A., Kumar, R.P., 2013. Modelling of buried faults using applied element method. International Journal of Earthquake Engineering and Science 3 (1), 1-16.

Iwahashi, J., Watanabe, S., Furuya, T., 2001. Landform analysis of slope movements using DEM in Higashikubiki area, Japan. Computers & Geosciences 27, 851-865.

Iwahashi, J., Watanabe, S., Furuya, T., 2003. Mean slope-angle frequency distribution and size frequency distribution of landslide masses in Higashikubiki area, Japan. Geomorphology 50, 349-364.

Jenness, J., 2006. Topographic Position Index (tpi_jen.avx) extension for ArcView 3.x, v. 1.2. Jenness Enterprises. Available at: http://www.jennessent.com/arcview/tpi.htm.

Jibson, R.W., Harp, E.L., 2011. Field reconnaissance report of landslides triggered by the January 12, 2010, Haiti earthquake. U.S. Geological Survey Open-File Report 2011–1023, 19 p.

Jibson, R.W., Harp, E.L., Michael, J.A., 2000. A method for producing digital probabilistic seismic landslide hazard maps. Engineering Geology 58, 271-289.

Jibson, R.W., Harp, E.L., Schulz, W., Keefer, D.K., 2004. Landslides triggered by the 2002 M-7.9 Denali Fault, Alaska, earthquake and the inferred nature of the strong shaking. Earthquake Spectra 20, 669-691.

Jibson, R.W., Harp, E.L., Schulz, W., Keefer, D.K., 2006. Large rock avalanches

triggered by the M 7.9 Denali Fault, Alaska, earthquake of 3 November 2002. Engineering Geology 83, 144-160.

Jibson, R.W., Keefer, D.K., 1989. Statistical analysis of factors affecting landslide distribution in the New Madrid seismic zone, Tennessee and Kentucky. Engineering Geology 27, 509-542.

Jin, W., Tang, L., Yang, K., Wan, G., Lü, Z., and Yu, Y., 2009. Tectonic evolution of the middle frontal area of the Longmen Mountain thrust belt, western Sichuan basin, China. Acta Geologica Sinica 83, 92-102.

Kamp, U., Growley, B.J., Khattak, G.A., Owen, L.A., 2008. GIS-based landslide susceptibility mapping for the 2005 Kashmir earthquake region. Geomorphology 101, 631-642.

Keefer, D.K., 1984. Landslides caused by earthquakes. Geological Society of America Bulletin 95, 406-421.

Keefer, D.K., 2000. Statistical Analysis of an Earthquake-induced Landslide Distribution-the 1989 Loma Prieta, California Event. Engineering Geology 58, 213-249.

Keefer, D.K., Manson, M.W., 1998. Regional distribution and character of landslides generated by the earthquake. In: Keefer, D.K. (Ed.), The Loma Prieta, California earthquake of October 17, 1989-landslides. U.S. Geol Survey Prof Paper, 1551-C, p. 7–32.

Kenneth D. Ridgway, K.D., Trop, J.M., Nokleberg, W.J., Davidson, C.M., Eastham, K.R., 2002.Mesozoic and Cenozoic tectonics of the eastern and central Alaska Range: Progressive basin development and deformation in a suture zone Geological Society of America Bulletin, 114, 1480-1504.

Khazai, B., Sitar, N. 2003. Evaluation of factors controlling earthquake-induced landslides caused by Chi–Chi earthquake and comparison with the Northridge and Loma Prieta events. Engineering Geology 71, 79–95.

King, G.C.P., Stein, R.S., Lin, J., 1994. Static stress changes and the triggering of earthquakes. Bulletin of the Seismological Society of America 84, 935-953.

Kirby, E., Whipple, K.X., Burchfiel, B.C., Tang, W., Berger, G., Sun, Z., Chen, Z., 2000. Neotectonics of the Min Shan, China: implications for mechanisms driving Quaternary deformation along the eastern margin of the Tibetan Plateau. Geological Society of America Bulletin 112, 375-393.

Kirby, E., Whipple, K.X., Tang, W., Chen, Z., 2003. Distribution of active rock uplift along the eastern margin of the Tibetan Plateau: inferences from bedrock channel longitudinal profiles. Journal of Geophysical Research 108 (B4), 2217.

Korup, O., 2004. Geomorphic implications of fault zone weakening: slope instability along the Alpine Fault, South Westland to Fiordland. New Zealand Journal of Geology and Geophysics 47, 257–267.

Korup, O., 2008. Rock type leaves topographic signature in landslide-dominated mountain ranges. Geophys. Res. Lett. 35, L11402. doi:10.1029/2008GL034157.

Korup, O., Schlunegger, F., 2009. Rock-type control on erosion-induced uplift, eastern Swiss Alps. Earth and Planetary Science Letters 278, 278–285.

Korup, O., Weidinger, J.T., 2011. Rock type, precipitation, and the steepness of Himalayan threshold hillslopes. In: Gloaguen, R., Ratschbacher, L. (Eds.), Growth and collapse of the Tibetan Plateau. Geological Society of London Special Publications 353, 235-249.

Kothe, R., Lehmeier, F., 1993. SAGA – Ein Programmsystem zur Automatischen Relief-Analyse. Zeitschrift für Angewandte Geographie 4, 11-21.

Lambert, M.L, Gaudin, J. and Cohen, R., 1987. Carte Geologique D'Haiti, Feuille Sud-Est: Port-au-Prince, 1:250,000, IMAGEO-CNRS.

Lange, D., Cembrano, J., Rietbrock, A., Haberland, C., Dahm, T., Bataille, K., 2008. First seismic record for intra-arc strike-slip tectonics along the Liquiñe-Ofqui fault zone at the obliquely convergent plate margin of the southern Andes. Tectonophysics 455, 14-24.

Lee, C.T., Huang, C.C., Lee, J.F., Pan, K.L., Lin, M.L, Dong, J.J., 2008. Statistical approach to earthquake-induced landslide susceptibility. Engineering Geology 100, 43-58.

Lee, S., Evangelista, D.G., 2006. Earthquake-induced landslide-susceptibility mapping using an artificial neural network. Natural Hazards and Earth System Sciences 6, 687-695.

Lettis, W. R., Wells, D.L., Baldwin, J.N., 1997. Empirical observations regarding reverse earthquakes, blind thrust faults, and quaternary deformation: are blind thrust faults truly blind? Bulletin of the Seismological Society of America 87, 1171-1198.

Li, Q., Gao, R., Wang, H., Zhang, J., Lu, Z., Li., P., Guan, Y., Guan,Y., , He, R., 2009. Deep background of Wenchuan earthquake and the upper crust structure beneath the Longmen Shan and adjacent areas. Acta Geologica Sinica 83, 733-739.

Li, Y., Allen, P.A, Densmore, A.L., Xu., Q, 2003. Evolution of the Longmen Shan Foreland Basin (western Sichuan, China) during the Late Triassic Indosinian Orogeny, Basin Research 15, 117-138.

Li, Y., Zhou, R., Densmore, A.L., Ellis, M.A., Yan, L., Dong, S., Richardson, N., Zhang, Y., He, Y., Chen, H., Qiao, B., Ma, B., 2008. Geological background of

Longmen Shan seismic belt and surface rupture in Wenchuan earthquake, Zhongguo Lixue Wenzhai 22, 1-12 (in Chinese).

Liao, H.W., Lee, C.T., 2000 Landsides triggered by the Chi-Chi Earthquake, Proceedings of the 21st Asian Conference on Remote Sensing, Taipei, Volume 1-2, 383-388.

Lin, A., 2009. Geometry and Slip Distribution of Co-seismic Surface Ruptures Produced by the 2001 Kunlun, Northern Tibet, Earthquake. In: Fukuyama, E. (Ed.), Fault-Zone Properties and Earthquake Rupture Dynamics. Elsevier, San Diego, California, p. 15-36.

Lin, A., Ren, Z., Jia, D., Wu, X., 2009. Co-seismic thrusting rupture and slip distribution produced by the 2008 M_w 7.9 Wenchuan earthquake, China. Tectonophysics 47, 203-215.

Lin, M.-L., Tung, C.-C., 2003. A GIS-based potential analysis of the landslides induced by the Chi-Chi earthquake. Engineering Geology 71, 53-77.

Liu, N., Zhang, J.X., Lin, W., Cheng, W.Y., Chen, Z.Y., 2009. Draining Tangjiashan Barrier Lake after Wenchuan Earthquake and the flood propagation after the dam break. Sci China Ser E-Tech Sci 52, 801-809.

Liu-Zeng, J., Zhang, Z., Wen, L., Tapponnier, P., Sun, J., Xing, X., Hu, G., Xu, Q., Zeng, L., Ding, L., Ji, C., Hudnut, K.W., Van der Woerd, J., 2009. Co-seismic ruptures of the 12 May 2008, Ms 8.0 Wenchuan earthquake, Sichuan: East-west crustal shortening on oblique, parallel thrusts along the eastern edge of Tibet. Earth and Planetary Science Letters 286, 355-370.

Ma, S. Distinct asymmetry in rupture-induced inelastic strain across dipping faults: An off-fault yielding model. Geophys. Res. Lett., 36, L20317, doi: 10.1029/2009GL040666 (2009).

Mahdavifar, M.R., Solaymani, S., Jafari, M.K., 2006. Landslides triggered by the Avaj, Iran earthquake of June 22, 2002. Engineering Geology 86, 166-182.

Mai, P., Spudich, P., Boatwright, J., 2005. Hypocenter Locations in Finite-Source Rupture Models. Bulletin of the Seismological Society of America 95, 965–980.

Malamud, B.D. Turcotte, D.L. Guzzetti, F., Reichenbach, P., 2004. Landslides, earthquakes, and erosion. Earth and Planetary Science Letters 229, 45-59.

Mamdani, E.H., Assilian, S., 1975. An experiment in linguistic synthesis with a fuzzy logic controller International Journal of Man–Machine Studies 7 (1), 1-13.

Manaker, D.M., Calais, E., Freed, A.M., Ali, S.T., Przybylski, P., Mattioli, G., Jansma, P., Prépetit, C., de Chabalier, J.B., 2008. Interseismic plate coupling and strain partitioning in the northeastern Caribbean, Geophysical Journal International 174,

889–903.

Mann, P., Matumoto, T., Burke, K., 1984. Neotectonics of Hispaniola-plate motion, sedimentation, and seismicity at a restraining bend. Earth Planetary Science Letters 70, 311-324.

Mann, P., Taylor, F.W., Edwards, R.L., Ku, T.L., 1995. Actively evolving microplate formation by oblique collision and sideways motion along strike-slip faults: An example from the northwestern Caribbean plate margin. Tectonophysics 246, 1-69.

Mantovani, F., Soeters, R., van Westen, C.J., 1996. Remote sensing techniques for landslide studies and hazard zonation in Europe. Geomorphology 15, 213-225.

Marhsall, G.A., Stein, R.S., Thatcher, W., 1991. Faulting geometry and slip from co-seismic elevation changes: the 18 October 1989, Loma Prieta, California, earthquake, Bull. Seism. Soc. Am. 81, 1660-1693.

Martha, T.R., 2011. Detection of Landslides by Object-Oriented Image Analysis: e-book. PhD Thesis University of Twente. ITC Dissertation 189, ISBN: 978-90-6164-309-8.

Martha, T.R., Kerle, N., Jetten, V., van Westen, C.J., Kumar, K.V., 2009. Characterising spectral, spatial and morphometric properties of landslides for semi-automatic detection using object-oriented methods, Geomorphology 116, 24-36.

Martinez-Diaz, J.J., Bejar-Pizarro, M., Alvarez-Gomez, J.A., Mancilla, F.D., Stich, D., Herrera, G., Morales, J., 2012. Tectonic and seismic implications of an intersegment rupture the damaging May 11th 2011 M_w 5.2 Lorca, Spain, earthquake. Tectonophysics 546, 28-37.

Maruyama, T., Fusejima, Y., Yoshioka, T., Awata, Y., Matsu'ura, T., 2005. Characteristics of the surface rupture associated with the 2004 Mid Niigata Prefecture earthquake, central Japan and their seismotectonic implications. Earth Planets and Space, 57(6), 521-526.

Matmon, A., Schwartz, D.P., Haeussler, P.J., Finkel, R., Lienkaemper, J.J., Stenner, H.D., Dawson, T.E., 2006. Denali fault slip rates and Holocene-late Pleistocene kinematics of central Alaska. Geology 34, 645-648.

McCalpin, J.P., 2009. Paleoseismology (2nd Edition), Academic Press, New York, 629p.

McColl, S.T., Davies, T.R.H., McSaveney, MJ., 2012. The effect of glaciation on the intensity of seismic ground motion. Earth Surface Processes and Landforms 37(12), 1290-1301.

Mercier de Lépinay, B., Deschamps, A., Klingelhoefer, F., Mazabraud, Y., Delouis, B., Clouard, V., Hello, Y., Crozon, J., Marcaillou, B., Graindorge, D., Vallée, M.,

Perrot, J., Bouin, M.P., Saurel, J.M., Charvis, P., St-Louis, M., 2011. The 2010 Haiti earthquake: A complex fault pattern constrained by seismologic and tectonic observations, Geophysical Research Letters 38, L22305, doi:10.1029/2011GL049799

Metternicht, G., Hurni, L. and Gogu, R., 2005. Remote sensing of landslides: An analysis of the potential contribution to geo-spatial systems for hazard assessment in mountainous environments. Remote Sensing of Environment 98, 284-303.

Meunier, P., Hovius, N., Haines, A.J., 2008. Topographic site effects and the location of earthquake-induced landslides. Earth and Planetary Science Letters 275, 221–232.

Meunier, P., Hovius, N., Haines, J.A., 2007. Regional patterns of earthquake-triggered landslides and their relation to ground motion. Geophysical Research Letters 34, 5 pp., doi:10.1029/2007GL031337.

Miles, S.B., Keefer, D.K., 2009. Evaluation of CAMEL - comprehensive areal model of earthquake-induced landslides. Engineering Geology 104, 1-15.

Molnar, P., Anderson, R.S., Anderson, S.P., 2007. Tectonics, fracturing of rock, and erosion. Journal of Geophysical Research 112, F03014. doi:10.1029/2005JF000433.

Mora, C., Comte, D., Russo, R., Gallego, A., Mocanu, V., 2010. Aysén seismic swarm (January 2007) in southern Chile: Analysis using joint hypocenter determination. Journal of seismology 14, 683-691.

NOAA (National Oceanic and Atmorspheric Administration), 2012. National Oceanographic Data Library, Haiti Climatological Data. http://docs.lib.noaa.gov/rescue/data_rescue_haiti.html.

Oglesby, D.D., Archuleta, R.J., Nielsen, S.B., 1998. Earthquakes on dipping faults: the effects of broken symmetry. Science 280, 1055-1059.

Oglesby, D.D., Archuleta, R.J., Nielsen, S.B., 2000a. Dynamics of dip-slip faulting: explorations in two dimensions. Journal of Geophysical Research 105, 13643-13653.

Oglesby, D.D., R.J. Archuleta, Nielsen, S.B., 2000b. The three dimensional dynamics of dipping faults. Bulletin of the Seismological Society of America 90, 616-628.

Ohta, Y., Ohzono, M., Miura, S., Iinuma, T., Tachibana, K., Takatsuka, K., Miyao, K., Sato, T., Umino, N., 2008. Coseismic fault model of the 2008 Iwate-Miyagi Nairiku earthquake deduced by a dense GPS network. Earth Planets Space 60, 1197–1201.

Owen, L.A., Kamp, U., Khattak, G.A., Harp, E., Keefer, D.K., Bauer, M., 2008. Landslides triggered by the October 8, 2005, Kashmir earthquake. Geomorphology 94, 1-9.

Ozacar, A. A., Beck S.L, 2004. The 2002 Denali Fault and 2001 Kunlun Fault

earthquakes: Complex rupture processes of two large strike-slip events, Bull. Seismol. Soc. Am., 94(6B), 278-292.

Paolucci, R., 2002. Amplification of earthquake ground motion by steep topographic irregularities. Earthquake Engineering and Structural Dynamics 31, 1831-1853.

Papadopoulos, G.A., Plessa, A., 2000. Magnitude–distance relations for earthquake-induced landslides in Greece. Engineering Geology 58, 377-386.

Pareek, N., Sharma, M.L., Arora, M.K., 2010. Impact of seismic factors on landslide susceptibility zonation: a case study in part of Indian Himalayas. Landslides 7, 191-201.

Plafker, G., Ericksen, G.E., Fernández Concha, J., 1971. Geological Aspects of the May 31, 1970, Perú Earthquake, Bulletin of the Seismological Society of America 61, 543-578.

Prentice, C.S., Mann, P., Crone, A.J., Gold, R.D., Hudnut, K.W., Briggs, R.W., Koehler, R.D., Jean, P., 2010. Seismic hazard of the Enriquillo-Plantain Garden fault in Haiti inferred from palaeoseismology, Nature Geoscience 3, 789-793.

Rengers, N., Soeters, R., van Westen, C.J., 1992. Remote Sensing and GIS applied to mountain hazard mapping. Episodes 15, 36-46.

Richter D.H., Jones, D.L., 1970. Structure and Stratigraphy of Eastern Alaska Range, Alaska. American Association of Petroleum Geologists Bulletin 54 (12), 2502-2512.

Rodriguez, C.E., Bommer, J.J., Chandler, R.J., 1999. Earthquake-induced landslides: 1980-1997. Soil Dynamics and Earthquake Engineering 18, 325-346.

Ruiz, S., Kausel, E., Campos, J., Saragoni, G.R., Madariaga, R., 2011. Identification of high frequency pulses from earthquake asperities along Chilean subduction zone using strong motion. Pure and Applied Geophysics 168, 125-139.

Rymer, M.J., Kendrick, K.J., Leinkaemper, J.J., Clark, M.M., 1990. The Nunez fault and its surface rupture during Coalinga earthquake sequence, in the Coalinga, California Earthquake of May 2, 1983, ed. by M. Rymer and W. Ellsworth, U.S. Geological Survey Prof. Pap. 1487, 299-318.

Sappington, J.M., Longshore, K.M., Thompson, D.B., 2007. Quantifying landscape ruggedness for animal habitat analysis: A case study using bighorn sheep in the Mojave Desert. The Journal of Wildlife Management 71, 1419-1426.

Sassa, K., Fukuoka, H., Scarascia-Mugnozza, G., Irikura, K. and Okimura, T., 1995. Landslides Triggered by the Hyogoken-Nanbu Earthquake, Landslide News 9, 2-5.

Sato, H.P., Harp, E.L., 2009. Interpretation of earthquake-induced landslides triggered by the 12 May 2008, M7.9 Wenchuan earthquake in the Beichuan area, Sichuan

Province, China using satellite imagery and Google Earth. Landslides 6, 153-159.

Sato, H.P., Hsegawa, H., Fujiwara, S., Tobita, M., Koarai, M., Une, H., Iwahashi, J., 2007. Interpretation of landslide distribution triggered by the 2005 Northern Pakistan earthquake using SPOT5 imagery. Landslides 4, 113-122.

Scheidegger, A.E., 1998. Tectonic predesign of mass movements, with examples from the Chinese Himalaya. Geomorphology 26, 37-46.

Schneider, D., Huggel, C., Haeberli, W., Kaitna, R., 2011. Unraveling driving factors for large rock-ice avalanche mobility. Earth Surface Processes and Landforms, 36(14), 1948-1966.

Sen, G., Hickeyvargas, R., Waggoner, D.G., Maurrasse, F., 1988. Geochemistry of basalts from the Dumisseau formation, southern Haiti - implications for the origin of the Caribbean Sea crust. Earth and Planetary Science Letters 87, 423-437.

Shafique, M., van der Meijde, M., Kerle, N., van der Meer, F.D., 2011. Impact of DEM source and resolution on topographic seismic amplification. International Journal of Applied Earth Observation And Geoinformation 13, 420-427.

Shen, Z., Sun, J., Zhang, P., Wan, Y., Wang, M., Bürgmann, R., Zeng, Y., Gan, W., Liao, H., Wang, Q., 2009. Slip maxima at fault junctions and rupturing of barriers during the 2008 Wenchuan earthquake, Nature Geoscience 2, 718-724.

Shen, Z.K., Ge, B.X., Jackson, D.D., Potter, D., Cline, M., Sung, L.Y., 1996. Northridge earthquake rupture models based on the global positioning system measurements. Bulletin of the Seismological Society of America 86, 37-48.

Somerville, P.G., 2000. New developments in seismic hazard estimation. In: Proc., 6th International Conference on Seismic Zonation, Nov. 12–15, 2000, Palm Springs, CA, Proc. CD-ROM, 25 pp. Earthquake Engineering Research Institute, Oakland, CA.

Somerville, P.G., Pitarka, A., 2006. Differences in earthquake source and ground motion characteristics between surface and buried earthquakes. Processing of 8th National Conference on Earthquake Engineering, Paper No. 977.

Stein, R.S., 1999. The role of stress transfer in earthquake occurrence. Nature 402, 605-609.

Stout, J.H., Brady, J.B., Weber, F., Page, R.A., 1973. Evidence for Quaternary movement on Mckinley-Strand of Denali-Fault in Delta-River Area, Alaska. Geological Society of America Bulletin 84, 939-947.

Stout, J.H., Chase, C.G., 1980. Plate kinematics of the Denali fault system. Canadian Journal of Earth Sciences 17 (11), 1527-1537.

Su, F., Cui, P., Zhang, J., Xiang, L., 2010. Susceptibility assessment of landslides

caused by the Wenchuan earthquake using a logistic regression model. Journal of Mountain Science 7, 234-245.

Tang, L., Yang, K., Jin, W., Wan, G., Lü, Z., Yu, Y., 2009. Differential tectonic deformation of the Longmen Mountain thrust belt, western Sichuan Basin, China. Acta Geologica Sinica 83,158-169.

Tibaldi, A., Ferrari, L. and Pasquarè, G., 1995. Landsides triggered by earthquakes and their relations with faults and slope geometry: an example from Ecuador. Geomorphology 11, 215-226.

U.S. Geological Survey, 2002. The 2002 Denali Fault earthquake Magnitude 7.9 near Denali National Park, AK. http://earthquake.usgs.gov/earthquakes/eqinthenews/2002/uslbbl/

U.S. Geological Survey, 2008. Magnitude 7.9 - Eastern Sichuan, China, 2008 May 12 06:28:01 UTC. http://earthquake.usgs.gov/earthquakes/eqinthenews/2008/us2008ryan/

U.S. Geological Survey, 2010. Landslide Photo Collections, Haiti Earthquake-Induced Landslides, January 12, 2010.http://landslides.usgs.gov/learning/photos/international/haiti_earthquake induced_landslides__january_12__2010

van Westen, C.J., Castellanos Abella, E.A., Sekhar, L.K., 2008. Spatial data for landslide susceptibility, hazards and vulnerability assessment: an overview. Engineering Geology 102, 112–131.

van Westen, C.J., Seijmonsbergen, A.C., Mantovani, F., 1999. Comparing landslide hazard maps. Natural Hazards 20, 137-158.

van Zuidam, R.A., 1985. Aerial Photo-Interpretation in Terrain Analysis and Geomorphologic Mapping. ITC. Smits Publishers, The Hague, Netherlands.

Wada, K., Goto, H., 2012. Generation mechanism of surface and buried faults: Effect of plasticity in a shallow crust structure. Bulletin of the Seismological Society of America 102, 1712-1728.

Wang, E., Meng, Q, 2009. Mesozoic and Cenozoic tectonic evolution of the Longmenshan fault belt. Science in China Series D: Earth Science 52, 579-592.

Wang, F.W., Cheng, Q.G., Highland, L., Miyajima, M., Wang, H.B., Yan, C.G., 2009. Preliminary investigation of some large landslides triggered by the 2008 Wenchuan earthquake, Sichuan Province, China. Landslides 6, 47-54.

Wang, G.Q., Liu, F., Fu X.D., Li T.J., 2008. Simulation of dam breach development for emergency treatment of the Tangjiashan Quake Lake in China. Science in China Series E: Technological Sciences 51, 82-94.

Wang, H.B., Sassa, K., Xu, W.Y., 2007. Analysis of a spatial distribution of landslides triggered by the 2004 Chuetsu earthquakes of Niigata Prefecture, Japan. Natural Hazards 41, 43-60.

Wang, W., Sun, W., Jiang, Z. 2010. Comparison of fault models of the 2008 Wenchuan earthquake (Ms8.0) and spatial distributions of co-seismic deformations. Tectonophysics 491, 85-95.

Wang, W.N., Wu, H.L., Nakamura, H., Wu, S.C., Ouyang, S., Yu, M.F., 2003. Mass movements caused by recent tectonic activity: the 1999 Chi-Chi earthquake in central Taiwan. Island Arc 12, 325-334.

Weirich, F., Blesius, L., 2007. Comparison of satellite and air photo based landslide susceptibility maps. Geomorphology 87, 352-364.

Wells, D.I., Coppersmith, K.J., 1994. New empirical relationships among magnitude, rupture length, rupture width, rupture area, and surface displacement. Bulletin of the Seismological Society of America 84, 974-1002.

Wilson, F.H., Dover, J.H., Bradley, D.C., Weber, F.R., Bundtzen, T.K., Haeussler, P.J., 2008. Geologic Map of Central (Interior) Alaska. U.S. Geological Survey Open-File Report OF 98-133-A.

Wilson, J.P., Gallant, J.C., 2000. Terrain analysis principles and applications. Wiley, Toronto, 479 pp.

Wolinsky, M.A., Pratson, L.F., 2005. Constraints on landscape evolution from slope histograms. Geology 33, 477-480.

Xu, C., Xu, X., Yu, G., 2012. Landslides triggered by slipping-fault-generated earthquake on a plateau: an example of the 14 April 2010, Ms 7.1, Yushu, China earthquake. Landslides DOI 10.1007/s10346-012-0340-x.

Xu, G., Kamp, P.J.J., 2000. Tectonics and denudation adjacent to the Xianshuihe fault, eastern Tibetan Plateau: Constraints from fissiontrack thermochronology, Journal of Geophysical Research 105, 19231-19251

Xu, Q., Fan, X.M., Huang, R.Q., Westen, C.V., 2009. Landslide dams triggered by the Wenchuan earthquake, Sichuan Province, south west China. Bulletin of Engineering Geology and the Environment 68, 373-386.

Xu, X., Wen, X., Yu, G., Chen, G., Klinger, Y., Hubbard, J., Shaw, J., 2009. Coseismic reverse- and oblique-slip surface faulting generated by the 2008 M_w 7.9 Wenchuan earthquake, China. Geology 37, 515-518.

Yagi, H., Sato, G., Higaki, D., Yamamoto, M., Yamasaki, T., 2009. Distribution and characteristics of landslides induced by the Iwate-Miyagi Nairiku Earthquake in 2008 in Tohoku District, Northeast Japan. Landslides 6, 335-344.

Yamagishi, H., Iwahashi, J., 2007. Comparison between the two triggered landslides in Mid-Niigata, Japan by July 13 heavy rainfall and October 23 intensive earthquakes in 2004. Landslides, 4(4), 389-397.

Yin, Y., Wang, F., Sun, P., 2009. Landslide hazards triggered by the 2008 Wenchuan earthquake, Sichuan, China. Landslides 6 (2), 139-152.

Zhang, Y., Dong, S., Yang, N., 2009. Active faulting pattern, present-day tectonic stress field and block kinematics in the East Tibetan Plateau. Acta Geologica Sinica 83, 694-712

Zhao, C.P., Chen, Z.L., Zhou, L.Q., Li, Z.X., Kang, Y. 2010. Rupture process of the Wenchuan M8.0 earthquake of Sichuan, China: the segmentation feature. Chinese Science Bulletin 55, 284-292.

Zhou, D., Graham, S. A., 1996. Songpan-Ganzi Triassic flysch complex of the West Qinling Shan as a remnant ocean basin. In: A. Yin and M. Harrison (Eds.), The Tectonic Evolution of Asia, Cambridge Univ. Press, New York, pp. 281-299.

Summary

Earthquakes are among the most devastating geophysical processes on Earth, which have caused an estimated minimum of 13 million fatalities in the past 4000 years. Large, shallow earthquakes (>*M* 6.0) may trigger thousands of landslides in mountainous terrain due to the strong ground motion and the associated weakening of the hillslope materials. Generally, the destructive impact and casualties of earthquake triggered landslides are considered as a component of the earthquake damage itself, and thus their long-term economic and societal detrimental impact is generally overlooked. Yet casualties from recent earthquake-induced landslides indicate that the coseismic landslides as a secondary hazard can be very significant in major earthquakes that occur in mountainous regions.

The rate of coseismic landsliding and their distribution pattern can be highly variable in both its spatial and temporal aspects because of the variability of factors such as topography, geology, geomorphology, and the epicentral location and faulting mechanism of the seismic events. The location, type and abundance of earthquake-induced landslides in an area depend on the characteristics of the seismic parameters and on the predisposing conditions. The latter include the local and regional morphological and lithological setting, and more specifically the morphodynamics and the mechanical properties of the rocks and soils. It is generally understood that the abundance of coseismic landslides decreases markedly with distance from the epicenter and fault rupture. However, it is still not fully clear whether and how different fault types and geometries affect this decay of slope-failure density with decreasing seismic intensity in different seismo-tectonic and geomorphic environments, hampering reliable assessments of earthquake-induced landslide susceptibility.

This thesis presents results of a regional analysis at high spatial resolution of coseismic landslides in seismologically and geomorphologically contrasting events and landscapes. To improve the current state of coseismic landslide knowledge in a global context, the role that earthquake rupture dynamics, faulting styles, topography and rock-type may have on the size, abundance and the distribution pattern of the coseismic landslides were explored using a total of eight polygon based landslide event-inventories triggered by strike-slip and dip-slip earthquakes. The coseismic event-inventories of the 2002 Denali Fault, Alaska (M_w 7.9), 2007 Aisén Fjord, Chile (M_w 6.2), 2008 Wenchuan, China (M_w 7.9) and 2010 Haiti (M_w 7.0) earthquakes were generated within the scope of this thesis. The locations of 66,700 individual landslides in these four core study

sites were mapped by visual interpretation using pre- and post-earthquake high-resolution satellite images and aerial photos. The results associated with the controls of faulting type and fault geometry on the coseismic landslide distribution characteristics reveal that the thrust/reverse faulting earthquakes induce many more landslides than normal and strike-slip faulting earthquakes. In addition, the clustering of 70-85% of the landslides triggered by intermediate- and large-sized earthquakes (e.g. Wenchuan, Denali Fault, Chi-chi and Yushu earthquakes) over the surface projection (up- and down-dip edge) of earthquake fault revealed that the fault geometry is a key restrictive factor on the spatial landslide distribution pattern. In this respect, coseismic landslide abundance and the spatial asymmetry decrease with increasing dip angle of strike-slip faults, whereas the number and the overall area affected by the coseismic landslides increases with a decrease in dip angle for thrust and reverse faults for a given magnitude. Furthermore, in this study, it is demonstrated that the landslides triggered by the surface- and blind ruptured earthquakes are significantly different both in terms of distribution pattern and the fraction of area affected by the coseismic landslides. The comparison results of the event-inventories of six reverse or thrust-faulting earthquakes show that the mass-wasting responses to earthquakes with similar magnitudes in the hanging-wall are more pronounced and the landslides are larger in surface-ruptured earthquakes in contrast to the blind-ruptured earthquakes. Thus, in blind-ruptured earthquakes the distribution of landslides exhibits more symmetric pattern between the fault blocks though the fraction of the area remains higher on the hanging wall side. The results from different events show that the differences and variations in rupture dynamics (depth, mode and rate of the coseismic slip), in combination with the topography and the lithology have distinctive controls on limiting the size- and spatial distribution of coseismic landslides along the surface ruptures. From a regional geomorphological perspective, the coseismic landslide patterns in glaciated landscapes (e.g. the Denali Fault earthquake region) are considered to have a lower density, probably due to the fact that glaciers may reduce the topographic amplification although they may also significantly increase the run-out size of the landslides. In this regard, regional morphoclimatic and/or morphodynamic differences may affect the distribution characteristics, particularly the frequency-size distributions, of coseismic landslides. The variance in rollovers of magnitude-frequency distributions become more pronounced with differences in style of faulting, rupture and the topographic characteristics of the events. Therefore, landslide frequency-size distributions of different events show that future work

should consider the seismic properties (i.e. magnitude, faulting mechanism and rupture dynamics) and physiographic characteristics together rather focusing on earthquake magnitude alone. Our results call for modifications of existing models of earthquake triggered landslide susceptibility solely based on empirical relationships.

Overall, the comparison of different faulting events in diverse geomorphic environments strengthens our hypothesis that the distribution pattern, abundance, and area affected by coseismic landslides are linked closely with the fault geometry and type, the changes in geomorphic and topographic characteristics, and the rate and mode of the coseismic displacements along the surface ruptures. Based on our assessment about the combined impacts of the seismic parameters and the predisposing conditions this study suggests a new conceptual model for earthquake triggered landslide patterns, which may contribute to the current state of our understanding of coseismic landsliding in a regional context. In this manner, the proposed conceptual model may further help to the landslide research community to improve the knowledge-guided empirical susceptibility assessment for earthquake triggered landslides.

Samenvatting

Aardbevingen zijn een van de meest verwoestende geofysische processen op aarde, welke naar schatting minimaal 13 miljoen doden in de afgelopen 4000 jaar veroorzaakt hebben. Grote, ondiepe aardbevingen (> 6,0 M) kunnen duizenden aardverschuivingen veroorzaken in bergachtig terrein als gevolg van sterke grondbewegingen en de bijbehorende verzwakking van de hellingmaterialen. Over het algemeen worden de verwoestende gevolgen en slachtoffers van door aardbevingen veroorzaakte massabewegingen in de schadestatistieken beschouwd als een onderdeel van de aardbevingsschade zelf, en daardoor worden de schadelijke economische en maatschappelijke effecten van deze aardverschuivingen op lange termijn vaak onderschat. Het grote aantal slachtoffers van door recente aardbevingen veroorzaakte aardverschuivingen geeft echter aan dat deze als secundair gevaar zeer aanzienlijk kunnen zijn, en het is van belang deze afzonderlijk van de directe aardbevingsschade te evalueren.

De hoeveelheid massabewegingen die veroorzaakt worden door aardbevingen en hun verspreidingspatroon kan zeer variabel zijn in zowel ruimtelijke en temporele zin, vanwege de variabiliteit van factoren zoals topografie, geologie, geomorfologie, de locatie van het epicentrum en het breukmechanisme van de aardbevingen. De locatie, het type en de grootte van de door aardbevingen veroorzaakte massabewegingen in een gebied hangt af van de kenmerken van de seismische parameters en de terreincondities. Deze laatste omvatten de lokale en regionale morfologische en lithologische omgeving, en meer specifiek de morfodynamiek en de mechanische eigenschappen van de gesteenten en bodems. Over het algemeen wordt ervan uitgegaan dat de hoeveelheid aardverschuivingen sterk afneemt met de afstand van het epicentrum en de breukzone. Het is echter nog steeds niet volledig duidelijk of en hoe de verschillende breuktypes en geometrieën van invloed zijn op deze trend van verminderende aardverschuivingsdichtheid met afnemende seismische intensiteit in verschillende seismisch-tektonische en geomorfologische milieus. Dit belemmert een betrouwbare ruimtelijke evaluatie van de door aardbevingen veroorzaakte aardverschuivingsgevoeligheid en gevaar.

Dit proefschrift presenteert de resultaten van een regionale analyse, met hoge ruimtelijke resolutie, naar de verspreidingspatronen van door aardbevingen veroorzaakte massabewegingen (coseismic landslides) voor verschillende seismologische gebeurtenissen en onder diverse geomorfologische condities.

Dit onderzoek draagt bij aan een beter inzicht in de invloed van breukdynamiek, breuktypes, topografie en gesteentetypes op aardbeving gerelateerde aardverschuivingen. Het verspreidingspatroon van dergelijke aardverschuivingen werd onderzocht door middel van een groep van acht, op polygonen gebaseerde, aardverschuivingskaarten voor aardbevingen veroorzaakt door zijschuivingen (strike-slip) en opschuivingen/overschuivingen (dip-slip). Voor de volgende aardbevingen werden binnen dit onderzoek aardverschuivingskaarten gegenereerd met behulp van satellietbeeldinterpretatie: Denali Fault (Alaska, 2002, Mw 7.9), Aisen Fjord (Chili, 2007, Mw 6.2), Wenchuan (China, 2008, Mw 7.9) en Haïti (2010, Mw 7.0). De locaties van 66.700 individuele aardverschuivingen in deze vier studiegebieden werden in kaart gebracht door middel van visuele interpretatie van hoge resolutie satellietbeelden en luchtfoto's van voor en na de aardbeving. De resultaten met betrekking tot de invloed van het breuktype en geometrie op de kenmerken van aardbeving gerelateerde aardverschuivingsdistributies onthullen dat aardbevingen met overschuiving (thrust faults) en opschuiving (reverse faults) veel meer aardverschuivingen veroorzaken dan die met afschuiving (normal faults) en horizontaal verschuiving (strike-slip faults). De studie toonde aan dat 70-85 % van de aardverschuivingen die veroorzaakt worden door intermediaire - en grote aardbevingen (bv. Wenchuan , Denali Fault , Chi-chi en Yushu aardbevingen) plaatsvinden op het projectievlak van breuken. Dit is een duidelijke aanwijzing dat de breuk geometrie een belangrijke invloed heeft op de ruimtelijke verdeling van aardverschuivingen. De hoeveelheid coseismische aardverschuivingen en de ruimtelijke asymmetrie neemt af met toenemende hellingshoek van zijschuivingen (strike-slip faults), terwijl het aantal en de totale oppervlakte van deze toeneemt met een daling van de hellingshoek voor opschuivingen (reverse faults) en overschuivingen (thrust faults). Verder is in deze studie aangetoond dat er een groot verschil bestaat in de ruimtelijke patronen en dichtheden van massabewegingen veroorzaakt door aardbevingen met aan het oppervlakte dagzomende breuklijnen (surface ruptures) en breuken die niet aan de oppervlakte treden (blind rupture faults). De vergelijking van de resultaten van de aardverschuivingskaarten van zes aardbevingen met opschuiving of overschuiving (reverse or thrust faults) toont aan dat aardbevingen met vergelijkbare magnitudes veel meer massabewegingen veroorzaken in het overschuivende deel van de breuk (hanging wall). De aardverschuivingen zijn in deze situatie veel groter in het geval van aan het oppervlakte dagzomende breuken (surface rupture) dan voor breuken die niet aan de oppervlakte treden (blind rupture). In deze laatste

situatie is het aardverschuivingspatroon meer symmetrisch hoewel het overschuivende deel nog steeds een grotere dichtheid heeft. De resultaten van de verschillende case studies tonen aan dat de verschillen en variaties in breukdynamiek (hypocentrale diepte, breuktype en hoeveelheid van coseismic slip) in combinatie met de topografie en de lithologie samen verantwoordelijk zijn voor de ruimtelijke verdeling van coseismische aardverschuivingen langs de breuklijnen. Vanuit een regionaal geomorfologische perspectief gezien, is het opvallend dat de aardverschuivingspatronen in glaciale landschappen (bv. de Denali Fault in Alaska) een lagere dichtheid hebben. Dit is waarschijnlijk te wijten aan de vermindering van topografische amplificatie in gebieden die bedekt zijn door gletsjers. Daar staat tegenover dat de massabewegingen in die gebieden een significant grotere oppervlakte, en een langere uitlooplengte (run-out) hebben. In dit verband kan opgemerkt worden dat de regionale morfoklimatologische en/of morfodynamische verschillen sterk het aardverschuivingspatroon beïnvloeden, en dan met name de frequentieverdeling van de oppervlakte van de aardverschuivingen (size-frequency distribution). De variatie in de effecten met betrekking tot de lagere oppervlaktes (rollovers) van deze frequentieverdelingen worden meer uitgesproken met verschillen in de stijl van breuken, de manier van verplaatsing langs de breuk (rupture) en de topografische kenmerken. De variatie in frequentieverdelingen van aardverschuivingsgrootte voor de onderzochte aardbevingen geven aan dat in toekomstig onderzoek het van belang is om de seismische eigenschappen (d.w.z. aardbevingsmagnitude, breukmechanisme en verplaatsingsdynamiek) gezamenlijk te bestuderen tezamen met de fysiografische kenmerken, en minder te focussen op de magnitude alleen als indicatie voor de te verwachten aardverschuivingspatronen. De resultaten van dit onderzoek pleiten voor aanpassingen van bestaande modellen voor het analyseren van de gevoeligheid voor aardbeving gerelateerde massabewegingen, welke enkel zijn gebaseerd op empirische relaties.

Uiteindelijk versterkt de vergelijking van aardbevingen met verschillende breukmechanismes in verschillende geomorfologische milieus onze hypothese dat het verspreidingspatroon, de hoeveelheid, en het gebied dat getroffen wordt door coseismische aardverschuivingen nauw zijn verbonden met de breukgeometrie en het breuktype, de veranderingen in de geomorfologische en topografische kenmerken, en de hoeveelheid en modus van de coseismische breukverplaatsingen langs het oppervlak. Op basis van de uitgebreide analyse van de gecombineerde effecten van de seismische parameters en de terreincondities wordt er in dit proefschrift een nieuw conceptueel model

gepresenteerd, dat een bijdrage hoopt te leveren aan een betere voorspelling van de mogelijke regionale aardverschuivingspatronen, die veroorzaakt kunnen worden door aardbevingen in berggebieden. Dit voorgestelde conceptuele model hoopt een bijdrage te leveren aan het onderzoek om meer betrouwbare gevoeligheidskaarten voor coseismische aardverschuivingen te genereren op basis van kennis-geleide empirisch methodes.

Biography

Tolga Görüm was born in Muş, Turkey on January 01, 1980. He worked on his MSc degree in Geomorphology from 2003 to 2006 at the Physical Geography Department of Istanbul University, Turkey. His MSc research focused on hillslope processes and the landslide susceptibility assessment of Melen Gorge, in the northern part of the 1999 Duzce earthquake struck region, Turkey. In 2005 he joined the Natural Sciences Research Center of Yildiz Technical University as a research assistant. Since then his work has mainly focused on natural hazards and earth surface processes in active mountain belts, tectonic geomorphology and earthquake triggered landslides in specifically. Tolga worked on several research projects which were supported by the Scientific and Technological Research Council of Turkey and he has published results from those projects in a range of articles in international journals, and presented at various conferences. In 2008 he was awarded a HUYGENS scholarship by the Netherlands Organization for International Cooperation in Higher Education (NUFFIC) to carry out his PhD research in the Faculty of Geo-Information Science and Earth Observation of the University of Twente (ITC). In October 2008, he started his PhD working on the analysis of size, distribution pattern and characteristics of coseismic landslides in different tectonic and geomorphic environments. During his PhD, he published 5 peer reviewed paper and presented his research in several international conferences and workshops.

Tolga Görüm currently lives in İstanbul, Turkey with his wife Hale and their son Aral.

Author's publications

1. **Tolga Gorum**, Cees J van Westen, Oliver Korup, Mark van der Meijde, Xuanmei Fan, Freek van der Meer (2013), Complex rupture mechanism and topography control symmetry of mass-wasting pattern, 2010 Haiti earthquake. *Geomorphology 184, 127-138.*

2. Xuanmei Fan, Cees J van Westen, Oliver Korup, **Tolga Gorum**, Qiang Xu, Fuchu Dai, Runqiu Huang, Gonghui Wang (2012), Transient water and sediment storage of the decaying landslide dams induced by the 2008 Wenchuan earthquake, China, *Geomorphology 171, 58-68.*

3. Xuanmei Fan, Cees J van Westen, Qiang Xu, **Tolga Gorum**, Dai Fuchu, (2012), Analysis of landslide dams induced by the 2008 Wenchuan earthquake, *Journal of Asian Earth Sciences 57, 25-37*.

4. **Tolga Gorum**, Xuanmei Fan, Cees J. van Westen, Run Qiu Huang, Qiang Xu, Chuan Tang, Gonghui Wang (2011), Distribution pattern of earthquake-induced landslides triggered by the 12 May 2008 Wenchuan earthquake. *Geomorphology 133 (3), 152-167*.

5. Oliver Korup, **Tolga Görüm**, Yuichi Hayakawa (2012), Without power? Landslide inventories in the face of climate change. *Earth Surface Processes and Landforms 37, 92-99.*

6. Erkan Gökaşan, **Tolga Görüm**, Hüseyin Tur, Fatmagül Batuk (2012), Morpho-tectonic evolution of the Çanakkale Basin (NW Anatolia): evidence for a recent tectonic inversion from transpression to transtension. *Geo-Marine Letters 32*, 227-239. DOI: 10.1007/s00367-011-0262-y.

7. K. Zorlu, M. Celal Tunusluoglu, T. Gorum, H.A. Nefeslioglu, A. Yalcin, D. Turer, C. Gokceoglu, (2011), Landform effect on rockfall and hazard mapping in Cappadocia (Turkey). Environmental Earth Sciences 62 (8), *1685-1693*.

8. Hakan A Nefeslioglu, Candan Gokceoglu, Harun Sonmez, **Tolga Gorum** (2011), Medium-scale hazard mapping for shallow landslide initiation: the Buyukkoy catchment area (Cayeli, Rize, Turkey). *Landslides 8 (4), 459-483*.

9. Erkan Gokasan, Huseyin Tur, Mustafa Ergin, **Tolga Gorum**, Fatma Gul Batuk, Nurcan Sagci, Timur Ustaomer, Ozan Emem and Hakan Alp (2010). Late Quaternary evolution of the Çanakkale Strait region (Dardanelles, NW Turkey): implications of a major erosional event for the postglacial Mediterranean-Marmara Sea connection. *Geo-Marine Letters 30 (2), 113-131*.

10. C. Gokceoglu, M.C. Tunusluoglu, **T. Gorum**, H., Tur, E. Gokasan, A.B. Tekkeli, F. Batuk, H. Alp, (2009) Description of dynamics of the Tuzla Landslide and its implications for further landslides in the northern slope and shelf of the Cinarcik Basin (Marmara Sea, Turkey). *Engineering Geology 106, 133-153*.

11. T. Gorum, B. Gonencgil, C. Gokceoglu & H. A. Nefeslioglu. 2008, Implementation of Reconstructed Geomorphologic Units in Landslide Susceptibility Mapping: the Melen Gorge (NW Turkey). *Natural Hazards 46 (3), 323-351*.

12. T. Ustaomer, E. Gokasan, H. Tur, **T. Gorum**, F. Batuk, D. Kalafat, H.Alp, B. Ecevitoglu, H. Birkan. 2008, Faulting, mass-wasting and deposition in an active dextral shear zone, the Gulf of Saros and the NE Aegean Sea, NW Turkey. *Geo-Marine Letters 28 (3), 171-193*.

13. E. Gokasan, M. Ergin, M. Ozyalvac, H.I. Sur, H. Tur, **T. Gorum**, T. Ustaomer, F.G. Batuk, H. Alp, H. Birkan, A. Turker, E. Gezgin & M. Ozturan. 2008, Factors controlling the morphological evolution of the Canakkale Strait (Dardanelles, Turkey). *Geo-Marine Letters 28 (2), 107-129*.

14. E. Dolu, E. Gokasan, E. Meric, M. Ergin, **T. Gorum**, H. Tur, B. Ecevitoglu, N. Avsar, M. Gormus, F.G. Batuk, B. Tok & O. Cetin. 2007, Quaternary evolution of the Gulf of İzmit (NW Turkey): a sedimentary basin under control of the North Anatolian Fault Zone. *Geo-Marine Letters 27 (6), 355-381*.

15. E. Gokasan, H. Tur, B. Ecevitoglu, **T. Gorum**, A. Turker, B. Tok, F. Caglak, H. Birkan & M. Simsek. 2005, Evidence and implications of massive erosion along the Strait of Istanbul (Bosphorus), *Geo-Marine Letters 25, 324-342*.

ITC Dissertation List

http://www.itc.nl/Pub/research/Graduate-programme/Graduate-programme-PhD_Graduates.html